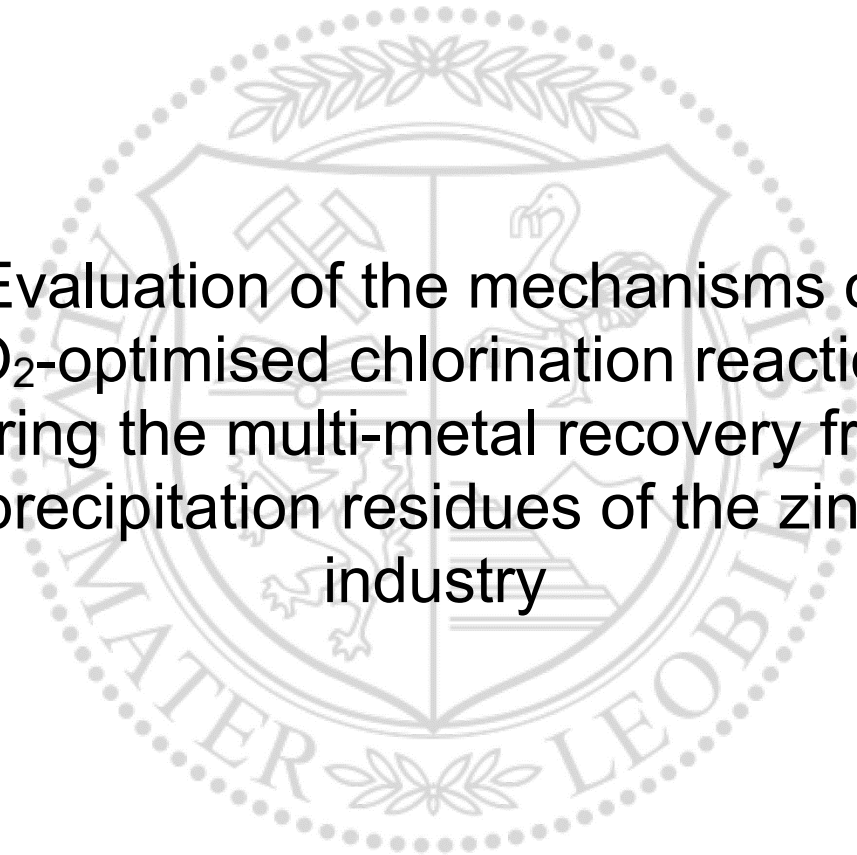




Chair of Nonferrous Metallurgy

Master's thesis



Evaluation of the mechanisms of
CO₂-optimised chlorination reactions
during the multi-metal recovery from
precipitation residues of the zinc
industry

Roberto Lerche, BSc

May 2021

Danksagung

An dieser Stelle möchte ich allen Personen, die mich beim Erstellen dieser Masterarbeit in unterschiedlichster Art und Weise vorangetrieben, motiviert und unterstützt haben, meinen größten Dank aussprechen.

Zuerst gebührt dieser Dipl.-Ing. Lukas Höber, der mir als Betreuer stets mit seiner fachlichen Expertise und seinem unermüdlichen Ideenreichtum zur Seite stand und so einen grundlegenden Beitrag zur Realisierung dieser Arbeit leistete. Er wusste stets auf subtile Weise die richtigen Impulse zu setzen, um den mir anvertrauten kreativen Freiraum mit der notwendigen Motivation zu füllen und mich in Richtung neuer Horizonte blicken zu lassen.

Ebenfalls möchte ich mich bei Priv.-Doz. Dipl.-Ing. Dr.mont. Stefan Steinlechner für seine hilfreichen Anregungen und konstruktive Kritik bedanken, womit er von Anfang bis Ende zur Hilfe stand. Ich bedanke mich außerdem bei dem Leiter des Lehrstuhls für Nichteisenmetallurgie, Univ.-Prof. Dipl.-Ing. Dr.mont. Helmut Antrekowitsch, für die Möglichkeit, an diesem hochspannenden Forschungsvorhaben teilgenommen haben zu dürfen.

Selbstverständlich sei auch meinen Eltern herzlichst gedankt, die mich von klein auf in all meinen Bestrebungen unterstützten und mich auch in den durchaus fordernden Phasen dieser Arbeit, in denen die Literaturberge nicht endend erschienen oder es tagelang Syntaxfehler regnete, auf allen Ebenen bestärkten. Nur Dank ihrer Unterstützung stehe ich heute dort, wo ich bin.

Alla fine, la lista non sarebbe mai completa senza ringraziare il mio sole Nathália. Grazie per avermi sempre dato lo spazio di calma e di pace che mi permetteva di superare le sfide di questa tesi nonostante la distanza che ci separava.

Abstract

Millions of tons of iron precipitation residues, predominantly jarosite, are accumulating in the primary zinc industry every year. Regardless of environmental concerns and its potential use as a secondary resource, the material is still commonly disposed of since none of the numerous already developed recycling techniques could prevail. In recent years, a new approach for a CO₂-optimized multi-metal recovery from the residues jarosite and goethite by means of a selective chlorination extraction has been proposed. In this thesis, the theoretical and practical potentials of this process have been thoroughly evaluated. A comprehensive simulation algorithm was developed in the Python programming language which gave profound insights into the thermochemical aspects of chlorination reactions by support of the FactSage Equilib computational software. The algorithm allows the simultaneous iteration of relevant reaction parameters such as temperature, pressure or stoichiometry and offers a high degree of freedom in the choice of reactants. Furthermore, statements about the influences of different chlorination agents, atmospheres and secondary components are possible. Based on the results of tens of thousands of different simulated scenarios, it was found that the carbon-free extraction of the valuable metals indium, silver, zinc and lead from a calcined jarosite material in the form of volatile chlorides is already possible at moderate temperatures and low chlorine additions, while the undesired iron phase remains in the solid residue. Since real processes are influenced by further factors that cannot be easily simulated on the basis of thermodynamics, a kinetic study of four small-scale chlorination campaigns was carried out to identify reaction mechanisms in more detail. An automated interpretation of a set of DSC measurements at different heating rates was realised by developing another Python algorithm. This facilitated the determination of the sequence of chemical steps in the chlorination of Ag₂O, In₂O₃ and ZnO with AlCl₃·6H₂O, MgCl₂·6H₂O and FeCl₃·6H₂O, respectively, and determined the activation energy of relevant reactions according to the Kissinger method. Due to its general applicability to any other suitable reactions, the algorithm poses the potential to facilitate future kinetic studies in multiple fields of science.

Kurzfassung

In der Zinkindustrie fallen jährlich Millionen von Tonnen an Eisenfällungsrückständen, vorwiegend Jarosit, an. Ungeachtet damit einhergehender ökologischer Aspekte und der potenziell möglichen Nutzung als Sekundärrohstoff, wird das Material fortwährend deponiert. Im Rahmen mehrerer Forschungsprojekte wird an der Montanuniversität Leoben ein innovativer Ansatz für eine wirtschaftlich realisierbare und CO₂-optimierte Multi-Metall-Rückgewinnung aus den Fällungsrückständen Jarosit und Goethit mittels selektiver Chlorierungsextraktionen verfolgt. In der vorliegenden Arbeit wurden die zugrundeliegenden Reaktionsmechanismen des Verfahrenskonzeptes eingehend evaluiert. Dies erfolgte durch die Entwicklung eines umfassenden Simulationsalgorithmus in der Programmiersprache Python. Gestützt durch die Berechnungssoftware FactSage Equilib, ermöglicht dieser ein tiefgehendes Verständnis der thermochemischen Aspekte von Chlorierungsreaktionen. Der Algorithmus bietet nicht nur die simultane Iteration relevanter Reaktionsparameter wie Temperatur, Druck oder Stöchiometrie, sondern bewerkstelligt auch eine limitationsfreie Wahl der in FactSage verfügbaren Reaktanten. Weiters sind Aussagen über die Einflüsse von verschiedenen Chlorierungsagenten, Atmosphären und Nebenbestandteilen möglich. Basierend auf den Ergebnissen von zehntausenden verschiedenen simulierten Szenarien wurde festgestellt, dass die kohlenstofffreie Extraktion der Wertmetalle Indium, Silber, Zink und Blei aus einem kalzinierten Jarositmaterial über die Gasphase bereits bei moderaten Temperaturen und geringer Chlorzugabe möglich ist, während Eisen im festen Rückstand verbleibt. Da reale Prozesse von weiteren Faktoren beeinflusst werden, die sich nicht ohne weiteres auf Basis der Thermodynamik simulieren lassen, wurde eine kinetische Studie von vier kleinmaßstäblichen Chlorierungskampagnen durchgeführt, um Reaktionsmechanismen näher zu identifizieren. Die Realisierung einer automatisierten Auswertung eines Satzes von DSC-Messungen bei unterschiedlichen Heizraten erfolgte durch die Entwicklung eines weiteren Python-Algorithmus. Dieser ermöglichte die Bestimmung der Abfolge von chemischen Schritten der Chlorierung von Ag₂O, In₂O₃ und ZnO mit AlCl₃·6H₂O, MgCl₂·6H₂O bzw. FeCl₃·6H₂O und die Berechnung der Aktivierungsenergien relevanter Reaktionen gemäß der Kissinger-Methode. Die Flexibilität der entwickelten algorithmischen Auswertemethode birgt das Potential für die automatisierte Untersuchung der Reaktionskinetik in weiteren relevanten Forschungsfeldern.

Eidesstattliche Erklärung

Ich erkläre an Eides statt, dass ich die vorliegende Arbeit selbstständig verfasst, andere als die angegebenen Quellen und Hilfsmittel nicht benutzt, und mich auch sonst keiner unerlaubten Hilfsmittel bedient habe.

Ich erkläre, dass ich die Richtlinien des Senats der Montanuniversität Leoben zu „Gute wissenschaftliche Praxis“ gelesen, verstanden und befolgt habe.

Weiters erkläre ich, dass die elektronische und gedruckte Version der eingereichten wissenschaftlichen Abschlussarbeit formal und inhaltlich identisch sind.

Affidavit

I declare on oath that I wrote this thesis independently, did not use other than the specified sources and aids, and did not use any unauthorized aids.

I declare that I have read, understood, and complied with the guidelines of the senate of the Montanuniversität Leoben for “Good Scientific Practice”.

Furthermore, I declare that the electronic and printed version of the submitted thesis are identical, both, formally and with regard to content.

.....
Roberto Lerche

Leoben, Juni 2021

List of contents

1	INTRODUCTION	1
1.1	Zinc production and accumulating residues	1
1.1.1	Methods for iron removal from pregnant leach solution	2
1.1.2	Comparison of iron precipitation residues	4
1.1.3	Significance of metals contained in precipitation residues	6
1.2	Recycling concepts and innovative new approach	7
1.3	Impact of an alternative indium-source on the global transition to clean energy	8
2	THEORETICAL EVALUATION OF SELECTIVE CHLORINATION EXTRACTION PROCESSES	10
2.1	Behaviour of solid chlorination agents in the course of extraction processes	11
2.1.1	Evaporation of the solid chlorination agent	11
2.1.2	Direct oxidation of the solid chlorination agent	13
2.1.3	Formation of an intermediate compound	14
2.2	Behaviour of to be extracted metal compounds	15
2.2.1	Evaporation of the metal compound	15
2.2.2	Direct chlorination of the metal compound	15
2.2.3	Formation of a volatile or stable compound	19
2.3	Direct reaction between the metal compound and SCA	19
2.4	Summary of potential influences on chlorination processes	20
3	THERMOCHEMICAL MODELLING OF ADVANCED CHLORINATION PROCESSES	21
3.1	Approach and methodology	21
3.1.1	Limitations of FactSage Equilib's input interface	21
3.1.2	Algorithmic automatization of reaction parameter input	22
3.2	Results	24
3.2.1	Assessment of individual metals	24
3.2.2	Assessment of metal mixtures	34
4	KINETIC STUDY OF CHLORINATION REACTIONS	45
4.1	The Kissinger-Method for kinetic parameter assessment	45
4.2	Approach and methodology	47
4.3	Results	48
4.3.1	Campaign 1: Ag_2O with $\text{AlCl}_3 \cdot 6\text{H}_2\text{O}$	48
4.3.2	Campaign 2: In_2O_3 with $\text{MgCl}_2 \cdot 6\text{H}_2\text{O}$	51
4.3.3	Campaign 3: Fe_2O_3 with $\text{AlCl}_3 \cdot 6\text{H}_2\text{O}$	53
4.3.4	Campaign 3: Fe_2O_3 with $\text{AlCl}_3 \cdot 6\text{H}_2\text{O}$	55
5	DISCUSSION	57
5.1	Comprehensive algorithmic simulation of chlorination reactions	57
5.2	Kinetic study of selected chlorination scenarios	60
6	SUMMARY AND OUTLOOK	61
7	LITERATURE	63

8	LIST OF FIGURES	71
9	LIST OF TABLES	76
10	APPENDIX	77
	Chapter 2	77
	Chapter 3	79
	Chapter 4	88

1 Introduction

Zinc is an essential metal for industrial economies that experienced tremendous growth since it first surpassed a global annual production of 1 Mio. tonnes in 1913. More than a hundred years later, in 2020, 13.6 Mio. tonnes of slab zinc were supplied globally, ranking it as the third largest non-ferrous metal [1]. China dominates the zinc industry by contributing with 33.1 % and 42.7 % to globally mined and produced zinc respectively. Remaining shares are distributed quite evenly among other countries of all continents. Regardless of the slight decrease in primary production observed in recent years, it is believed to recommence growing until reaching peak of around 17 Mio. tonnes in 2030 [2, 3].

Zinc is considered to bear one of the highest economic importances amongst other metals while facing only a relatively low supply risk [4]. This significance derives, among other factors, from its predominant industrial application in galvanizing steel. In the US, this usage share has increased from 50 % in 1990 to over 80 % in 2014, diminishing end uses in zinc and brass alloys or semi-manufactures [2, 5]. Compared to other metals, zinc also stands out in terms of its dissipative nature. This results not only from its corrosion in the sacrificial steel coatings. When applied as a vulcanizing agent in tires, ZnO is released into the environment through wear. Zinc is also lost to any recovery when ending up in chemicals as an essential nutrient to human health [6–8]. The share of recycled content in zinc production is reported to be relatively low, accounting for only between 10 wt.% [8] – 27 wt.% [7, 9]. Although the recycling rate is expected to increase through technological innovation and a rapid growth of secondary steel production from galvanized scrap, primary zinc will undoubtedly be the dominant supply to satisfy global demand in the near future [9, 10].

1.1 Zinc production and accumulating residues

Generally, both pyro- and hydrometallurgical routes exist for primary zinc production. In the EU, however, only one pyrometallurgical smelting furnace still operates in Poland [11]. Also globally, the hydrometallurgical route is almost exclusively set to practice, accounting for about 89 % of total world zinc output [12]. In the common hydrometallurgical route, also called roast-leach-electrowin (RLS) route, primarily utilized zinc sulphide (ZnS) concentrates enter the initial roasting step, where zinc is converted into an impure oxide (ZnO), also referred to as zinc calcine, which is to be dissolved in sulphuric acid subsequently. Sulphur released during the roasting process is converted into sulphuric acid and sold as a by-product. Due to the presence of up to 12 wt.% iron in commercial zinc ore concentrates, a variable but significant amount of hardly soluble zinc ferrite $\text{ZnO}\cdot\text{Fe}_2\text{O}_3$ is formed and contained in the calcine. As a

result, zinc leaching is conducted in two separate but interdependent circuits. At first, ZnO is dissolved in the primary neutral leach circuit, using low acid concentrations (from pH 5.5 – 15 g/l H₂SO₄, 60 °C) to obtain an iron-free solution, which is sent to purification followed by electrowinning. The largely unattacked residue, containing still around 20 wt.% zinc in form of ferrite or silicate, enters the secondary leach circuit where it is dissolved by hot and concentrated acid (from 30–120 g/l H₂SO₄, >90 °C). Residues of the secondary leaching step are generally composed of lead and silver, which form a marketable product. To avoid complications in the sensitive zinc electrolysis, in the pregnant leach solution dissolved iron must be removed beforehand. Several methods have been developed to achieve this. A schematic flow sheet of the roasting-leaching process is shown in Figure 1. [12–14]

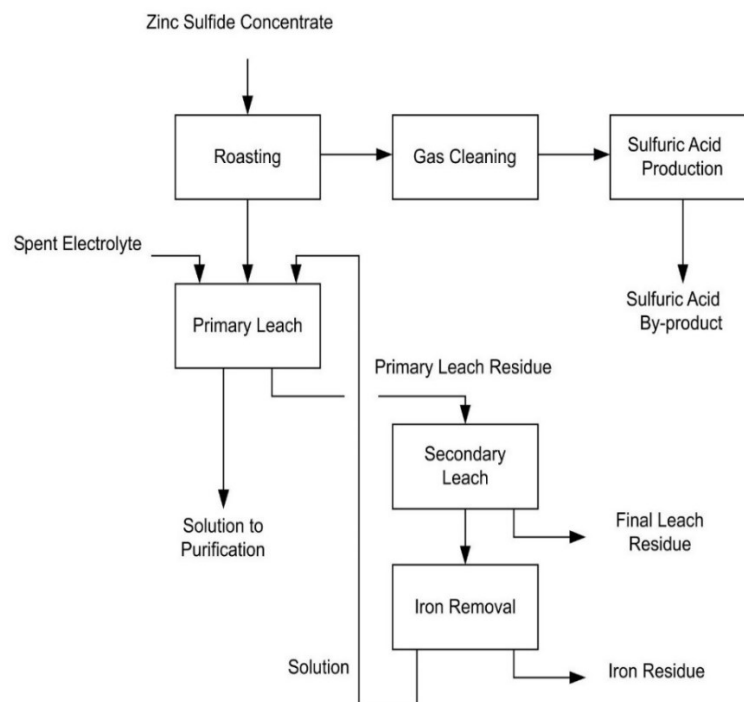


Figure 1: Roasting-leaching flow-sheet [12]

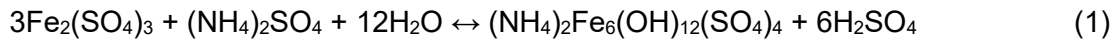
1.1.1 Methods for iron removal from pregnant leach solution

The development of techniques that allow the removal of iron from the pregnant leach solution in the late 1960s is considered as the most significant advance in the hydrometallurgical zinc production. Its implementation improved efficiencies of zinc extraction from around 85–90 % to reaching 98 %. The original and still predominantly applied method thereof is the jarosite process. [12]

- The Jarosite process

In the jarosite process, iron is precipitated as a complex basic iron sulfate in the form of $R_{(2)}Fe_3(SO_4)_2(OH)_6$ where the R position can be either occupied by two monovalent cations

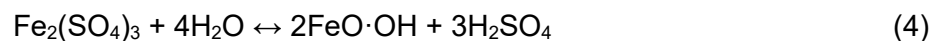
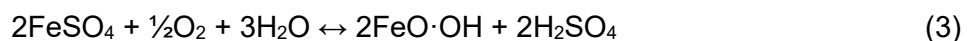
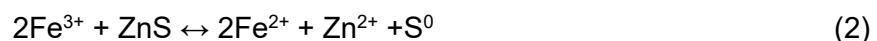
such as K^+ , NH_4^+ , Na^+ , Ag^+ , H_3O^+ or one bivalent cation like Pb^{2+} . To explain the chemical mechanism of jarosite precipitation, the reaction for ammonium jarosite is given in Equation 1 as a schematic example. [12]



The equilibrium concentration of dissolved iron highly depends on the solution's temperature. Typically, temperatures above 90 °C are preferred, resulting in practical operation values of around 0.01 for the ratio of $Fe^{3+}:H_2SO_4^2$ in g/l. As seen in Equation 1, one mole sulfuric acid is produced for every mole of precipitated iron which is neutralized by addition of calcine to proceed the reaction. Through the process, incoming iron loads of about 30 g/L can be reduced to less than 5 g/L. Jarosite precipitation is generally integrated as a loop circuit into the RLE, receiving the solution from secondary leach and delivering a zinc containing, iron-reduced solution which is returned to primary leach. Due to the higher pH in the neutral leach circuit the remaining iron is precipitated as ferric hydroxide, thus further reducing iron levels in the pregnant leach solution, which is introduced into the zinc-electrolysis subsequently. The precipitated iron exits the system in the final filtered and washed jarosite residue. Although a variety of slightly different processes have developed, a general exemplary process scheme shown in Figure 2 will be sufficient for this work. [12]

- The Goethite process

At lower ferric iron concentrations of below 2 g/L in the solution, the stable solid phase to be precipitated changes to goethite $FeO \cdot OH$. This property is applied in the goethite process, where iron is removed in either two steps according to Equations 2 and 3 or directly as shown in Equation 4. [12]



The two reaction paths are based on different approaches employed to reach the necessary low ferric iron levels. In the Vieille Montagne (VM) goethite process, zinc sulfide concentrate is added to the solution, which reduces the ferric iron to the ferrous state (Equation 2). Subsequently, goethite is precipitated in the precipitation tanks by re-oxidation with air, as shown in Equation 3. In the second technique, the paragoethite process, iron levels are decreased and maintained at a suitably low degree by control of the solution flow into a generally very large precipitation tank. Ideally, precipitation follows Equation 4, however, due to a poor concentration uniformity the obtained solid is typically impure. [12]

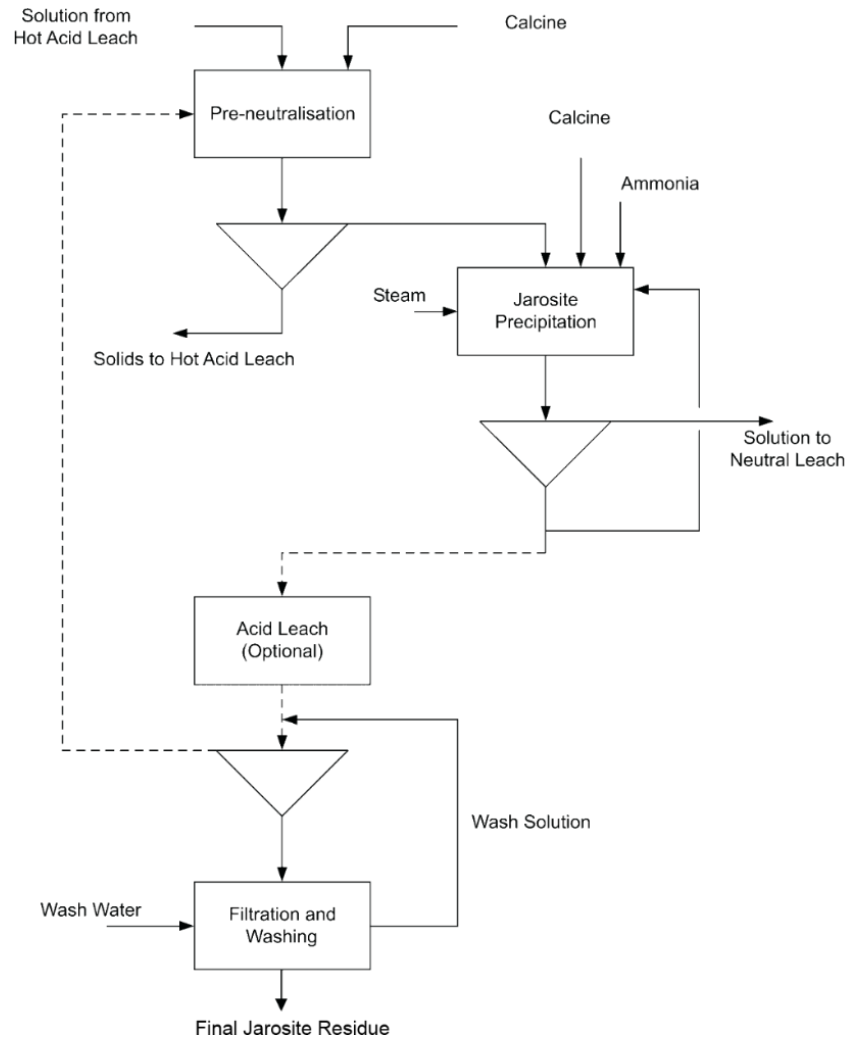
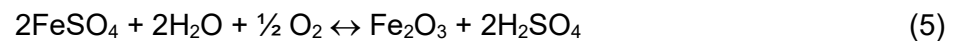


Figure 2: Schematic flow sheet of the jarosite process [12]

- The Hematite process

The third possibility for iron removal is the hematite process, where iron precipitates in the form of Fe_2O_3 according to Equation 5. This is achieved by the addition of oxygen at high process temperatures between 180 – 200 °C, at which the most stable solid phases in the $\text{Fe-SO}_4\text{-H}_2\text{O}$ system are less hydrated. [12]



Today, the hematite process is known to be applied in only one operating plant, which is why it will not be discussed in more detail. [15]

1.1.2 Comparison of iron precipitation residues

Depending on the applied precipitation method, residues with variable properties are obtained, which are shown in Table 1.

Table 1: Typical characteristics of common iron precipitation residues

Process	Jarosite	Goethite	Hematite
Fe content [wt%]	29 [12]	34–43 [12]	57–60 [12, 16]
Zn content [wt%]	2–6 [12, 16]	9–13 [12]	0–1 [12]
Moisture [wt%]	44–50 [16, 17]	43–50 [16, 17]	10 [16]
Dry quantity [kg/t Zn] [16]	520	370	245
Quantity moist [kg/t Zn] [16]	907	637	272

In comparison to jarosite, both theoretical and practical iron contents of goethite are significantly larger, reaching 63 % and 43 % subsequently, resulting in an about 25 % lower overall residue quantity. The major downside of goethite is its higher incorporation of zinc, which accounts for higher zinc losses than jarosite. Despite presenting the highest iron content, lowest zinc content and consequently lowest overall quantity, the hematite process is unfavoured due to its comparatively higher costs. Thus, the jarosite process still is the most commonly applied method for iron removal. [12, 16]

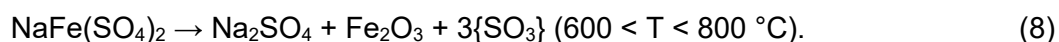
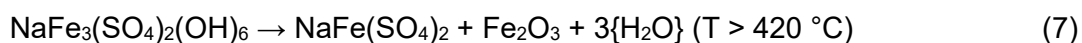
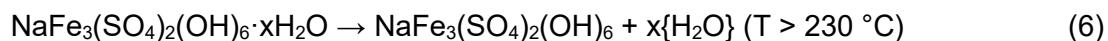
In addition to the above mentioned variability of the primary cation R in the basic jarosite formula $R_2Fe_3(SO_4)_2(OH)_6$, other ions can be substitutes for both the iron and sulfate group cation. At preferably high pH and low ferric ion concentrations, divalent base metals like Cu^{2+} , Zn^{2+} , Co^{2+} , Ni^{2+} or Mn^{2+} or trivalent metals like In^{3+} or Ga^{3+} are incorporated in the jarosite structure, replacing iron [14]. These impurities stem from dissolved compounds of the zinc calcine utilized for neutralization purposes during the precipitation process. Furthermore, some plants lack a sufficient separation utility for Pb-Ag-residues, which therefore end up in the iron residue as well. [16]

As a consequence, a variety of metals of economic interest are contained in jarosite, but also goethite precipitation residues. Table 2 gives an overview of typical concentration ranges of valuable metals present in common jarosite and goethite residues next to their current market price in pure form to underline their economic relevance.

Table 2: Typical concentration ranges and current market price of valuable metals contained in jarosite and goethite

Concentration	Jarosite [18–28]	Goethite [25]	Price [USD/kg]
Zn [wt%]	4.11±1.42	5.34±2.40	2.81 [29]
Pb [wt%]	4.38±2.50	2.22±0.33	1.93 [30]
Cu [wt%]	0.33±0.26	<1.5	8.94 [31]
In [g/t]	239±137		340 [32]
Ag [g/t]	239±197	80 – 2000 [33]	795 [34]
Ge [g/t]	49±11		1911 [32]
Ga [g/t]	99±46		534 [32]

At increasing temperatures, these residues stepwise decompose by first releasing water in the order of adsorbed, loosely bonded crystal water and structurally bonded water in the OH-group. Subsequently, the sulfate group is separated. This general thermal decomposition behaviour is shown exemplary for the case of sodium jarosite in Equations 6–8: [16]



Evidently, being heated to temperatures higher than 800 °C, the jarosite material significantly decreases in mass by evaporating volatile compounds, which make up a theoretical amount of around 36 wt.% for sodium jarosite. The solid residue primarily consists of the remaining iron oxide. Yet, metals shown in Table 2 are expected to show the same behaviour and therefore are converted into either sulfates or oxides, depending on their structural incorporation in the primary residue and stability of the formed compound at given temperature. [16]

1.1.3 Significance of metals contained in precipitation residues

Next to their economic value, some contained metals are of other importance. The aforementioned metals indium, germanium and gallium are assessed among the most critical raw materials for the EU. This property corresponds to both high economic importance and supply risk. Indium is essential to industrialized societies because of its hardly or non-substitutable application in screens and solar panels, resulting in a strong average demand growth of 4.5–8 % per year. However, as there is no significant production of indium within the EU, an increasingly tight supply is predicted [4]. Around 837 tons of refined indium were produced in 2018 [3]. This is in a similar magnitude of the annually lost indium in precipitation residues considering previously addressed production quantities and concentrations. Including the amount of already produced residue which has accumulated throughout the past decades, it bears an unneglectable source of valuable materials.

Although their high potential as a secondary resource, iron precipitation residues have been disposed of by a range of different means. Being stored in sole-purpose caverns, discharged in oceans, or combined with other tailings from mining are just examples of how jarosite has been directly released into the environment. There, it not only presents monetary loss from the economic point of view, but also causes environmental hazards by releasing elutable, toxic elements like Pb or Cd. [35]

1.2 Recycling concepts and innovative new approach

Processing and converting iron precipitation residues into a marketable product, thus reintroducing its valuable components into the material cycle and minimizing environmental pressure, has been focus of numerous research activities. Generally, the approaches can be categorized into pyro- and hydrometallurgical methods. Through hydrometallurgical treatments, the extraction of a generally smaller and defined number of metals is pursued by complex procedures consisting of numerous leaching and extraction steps. Therefore, different solutions have been investigated, including:

- Bio-leaching with special bacterial strains [36],
- alkaline leaching and cyanidation [37, 38], or
- leaching with NH_4Cl and reduction with Zn-powder [22].

Pyrometallurgical treatments aim to extract a variety of metals by means of high temperatures and, alternatively, also reducing agents. For iron precipitation residues, only pyrometallurgical methods are applied on an industrial scale in China [22]. They generally reach high metal recovery rates, yet must face several disadvantages such as high investment and operational costs, resource consumption and CO_2 -emissions as well as the necessity of air pollution control [39]. Pyrometallurgical treatment options include:

- Application in industrial facilities like waelz process or lead smelters [39],
- processing in plasma furnaces [40], or
- reduction and magnetic separation [41, 42].

Although comprehensive research has been done to find procedures for an economically and ecologically efficient recycling of valuable components of iron precipitation residues, they generally are still abandoned in sealed storage areas. To minimize disposal costs and environmental liabilities, several techniques have been developed with the pursuit of immobilizing concerning components in jarosite. According to the BREF paper of the European Union [11], the Jarofix process presents the best available treatment option. Hereby, the residue is mixed with around 15 wt.% cement, lime and water, resulting in a seemingly chemically und physically stable material. However, depending on the chemical composition of the input material, various mineralogical assemblages are possible, including some which are known to be spalling and dissolvable. The actual long-term stabilization over a period of more than 50 years is therefore questionable [11, 35]. Sinha et al. [43] calculated the annually produced and dumped amount of jarofix to around 0.5 million tons by only one zinc plant run by Hindustan Zinc Ltd. in Chittorgarh, Rajasthan state, India, accumulating to reach a total of around 23 million tons in India [43, 44]. Regardless of yet many unsuccessful attempts of developing methods for material recovery, a novel approach has been proposed by

Steinlechner and Antrekowitsch [45] in 2019. It was claimed that valuable metals such as zinc, indium or silver could be selectively extracted from jarosite by a reductive chlorine roasting. In this process, they are converted into volatile chlorides which evaporate at given temperatures and are separated from the remaining material through the off-gas. The so formed combined product can be processed in existing infrastructure for the separation of zinc, indium and silver [45]. Small scale experiments confirmed the potential of this novel treatment method [26]. Also, Wang et al. achieved extraction rates higher than 95 % for zinc, lead, copper and silver by treating a mixture of jarosite, CaCl_2 and coal at 1250 °C [46].

The scope of this work is to evaluate this multi-metal recovery by selective chlorination of valuable metals contained in jarosite for a range of different metals and scenarios in order to acquire a better understanding of how the process mechanisms work and are influenced by a variable set of conditions.

1.3 Impact of an alternative indium-source on the global transition to clean energy

Humanity is facing a series of urging problems, setting its survival to serious threats. The often discussed outbreak of a global pandemic became reality in late 2019, still striking global society and economy one and a half years later. A more underlying, less acute but potentially even more devastating threat is the rapidly changing climate. In the last 50 years, the global mean surface temperature rose by 0.7 °C, a pace which cannot be explained by natural forcing. The consequences of this rapid increase can be already observed as ocean acidification, mass decrease of arctic ice shields, sea level rise, unstable surface water flows and precipitation, local heat waves and droughts or altered migration behaviours of animals. There is no doubt that these anomalies are caused by human activity, namely the accelerating emission of greenhouse gases, primarily CO_2 by the combustion of fossil fuels, since the beginning of industrialization [47]. The main driver of the still increasing global CO_2 -emissions is the ongoing economic and population growth, which is coupled with and reflected in many sectors like primary energy use, transportation, telecommunication or international tourism. Steffen et al. illustrated the coupling of various strongly accelerating growth processes, of which a selection is shown in Figure 3. [48]

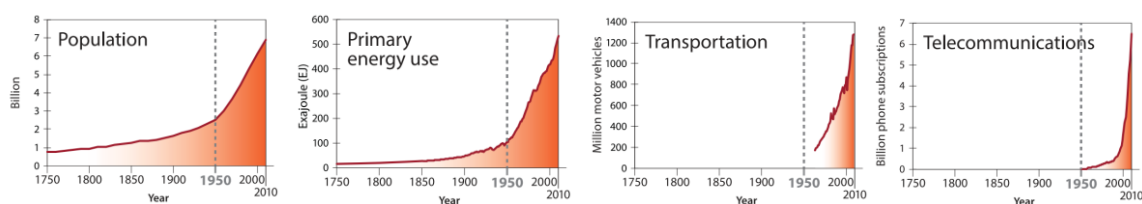


Figure 3: Coupling of accelerating economic and population growth with other sectors since the beginning of industrialization in 1750 [48]

Continued emissions of greenhouse gases will lead to further warming and long-lasting changes in all components of the climate system, increasing the likelihood of severe, pervasive and irreversible impacts on humans and ecosystems. Limiting climate change requires substantial and sustained reductions in greenhouse gas emissions. [47]

Energy systems for electricity and heat production are the main source of anthropogenic GHGs responsible for climate change, accounting for about 25 %, not including other forms of energy use for transport or industry [47]. Energy is applied in practically all sectors which are necessary to guarantee human wellbeing, which is why it plays a crucial role in development processes, leaving its impact on the climate even more important. In 2019, the primary global energy demand was supplied by about 81 % of fossil fuels, namely oil (31 %), coal (26 %) and natural gas (23 %) in declining order [49]. Apparently, a transition to renewable forms of energy such as photovoltaics (PV), wind and hydropower is essential in the fight against climate change and, according to the International Energy Agency, already well in progress. Electricity generation from wind and solar power is expected to triple in developed economies and to increase sixfold in emerging and developing economies in the period 2019–2030. [50]

These forecasted capacity increases also result in an elevated consumption of resources necessary to construct new energy systems. Per solar kilowatt-peak produced, approximately 0.045 kg of indium and 0.011 kg of silver are used. 74 % of total indium demand is converted into indium tin oxide, being applied as a transparent conductor in LCD screens and photovoltaic modules. However, end-of-life recycling rates of indium are below 1 %, resulting in a loss of practically the entire amount of metal applied in final products [51]. This is partly due to its increasingly complex integration and mix with other materials in constructional designs of current technological devices as well as their geographical dissipation resulting from the incorporation of only tiny amounts per device [52]. The fact, that primary indium is almost exclusively produced as a side-product in primary zinc extraction is yet another factor contributing to an insecure supply [53]. Furthermore, the yield of indium achieved during the extraction of primary zinc ores is below 50 % [54].

It is evident, that unlocking an alternative source of indium would relieve the supply stress created by rapidly growing renewable energy technology and therefore enable a more secure transition to a carbon-free energy system. The assessment of a recovery strategy for relevant metals from iron precipitation residues of the zinc industry is therefore an important part of increasing resource efficiency, thus lowering anthropogenic burdens on both the climate and environment.

2 Theoretical evaluation of selective chlorination extraction processes

Selective chlorination is a pyrometallurgical enrichment process based on altering the aggregate state of the component to be extracted by converting it into a volatile chloride compound. In primary metallurgy, chlorination reactions are commonly applied for production or refining purposes, including:

- Production of MgCl_2 from oxidic or carbonate ores,
- production of TiCl_4 and ZrCl_4 followed by Kroll-process,
- production and separation of NbCl_5 and TaCl_5 ,
- refining of aluminium (removal of Mg),
- refining of tin (removal of As, Bi, Pb), or
- refining of gold in the Miller-process (removal of Ag). [13]

Recently, high research activity considering the application of chlorination reactions for recycling purposes of residues or waste materials can be observed. There, selective vaporization of formed chloride compounds is not conducted for the removal of impurities from a product as in refining, but to the contrary pursues the recovery of certain metals through the developed gas phase. For this purpose, chlorine can be applied in various forms.

One option for applying chlorine for chlorination purposes is the use of gaseous compounds such as gaseous Cl_2 or HCl. Kanari et al. [55] assessed the chlorination of iron from wüstite (FeO) and hematite (Fe_2O_3) samples in the presence of Cl_2 at different conditions [55]. In another assessment, Kanari et al. [56] successfully decontaminated a treated jarosite material by chlorination of contained heavy metals using a gas mixture of Cl_2 and air. They achieved reductions of heavy metal compounds of above 90 % [56]. Barbosa et al. [57] observed significant extraction of lithium from spodumene mineral through chlorination with pure chlorine gas [57].

Huang et al. [58] found that the application of gaseous HCl promotes the vaporization of the metals Cd, Zn and Pb contained in municipal solid waste incineration fly ash [58]. Yajima et al. [59] assessed the weight loss of pure ZnO under variable Ar-HCl-O atmospheric conditions and found that chlorination increased with increasing partial pressure of HCl [59].

However, gaseous chlorine carrying agents can present disadvantages for industrial applications such as difficult handling and low selectivity for heavy metals, as they seem to favour chlorination of unwanted elements like Ca or Fe. Therefore, solid chlorination agents (SCA) appear to present higher potentials. [60]

SCAs are typically metal salts but in theory every solid carrier of chlorine can be applied. In literature, a wide variety of solid chlorides have been assessed, including NaCl, CaCl_2 ,

MgCl₂ [60], AlCl₃ [61], FeCl₃ [62], NH₄Cl [63], or even polyvinylchloride PVC [64]. Generally, SCAs present a number of advantages when compared to gaseous chlorination agents, including low cost, high availability and low toxicity [65]. Their applicability depends on the ability to deliver chlorine for the chlorination of to be extracted metals [66]. To compare different SCAs based on thermodynamic calculations, their schematic behaviour in the chlorination process must be evaluated first.

2.1 Behaviour of solid chlorination agents in the course of extraction processes

To draw conclusions about an SCA's potential for chlorinating favoured metal compounds contained in a given material, certain behaviours must be considered. Figure 4 outlays different fates of an SCA during temperature increase of a roasting process. In the scope of this work, the SCAs NaCl, CaCl₂, MgCl₂, AlCl₃ and FeCl₃ are to be assessed in more detail subsequently.

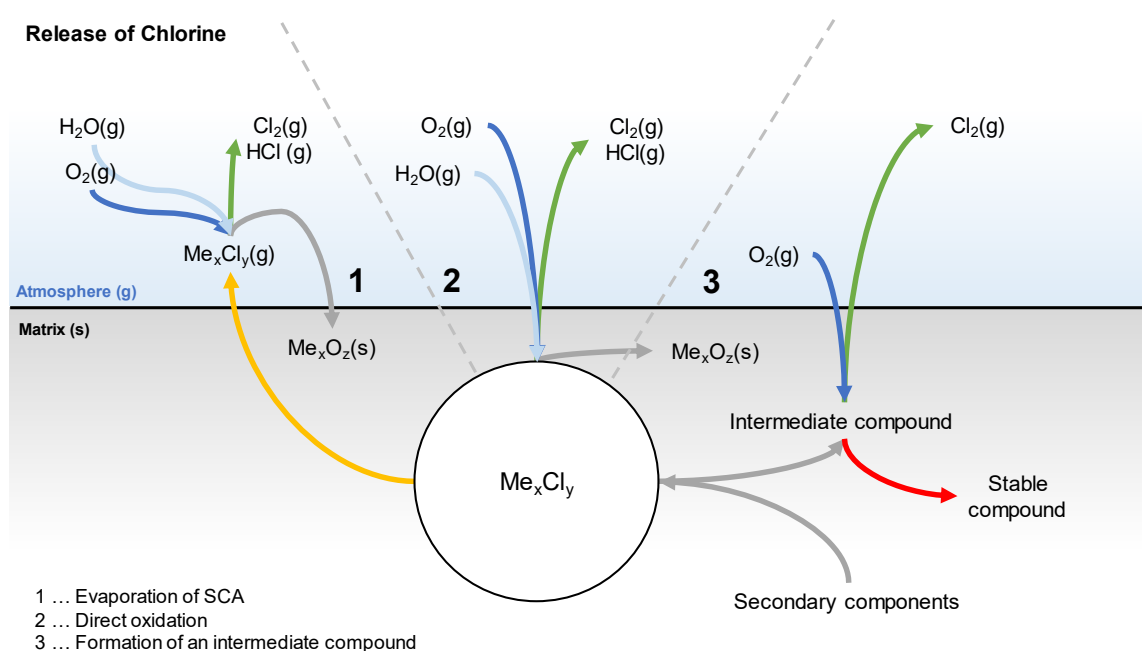


Figure 4: Different behavioural paths of an SCA during the chlorination roasting process

2.1.1 Evaporation of the solid chlorination agent

Volatile chlorides can develop significant vapor pressures even at considerably low temperatures, thus transfer into the reactor's atmosphere. To compare volatility of assessed SCAs, thermodynamic calculations were carried out in HSC Chemistry v6.12 [67] considering the vaporization described by Equation 9. Vapor pressure curves for the assessed SCAs were plotted in accordance to Steinlechner and Antrekowitsch's approach [16]. The results are shown in Figure 5.

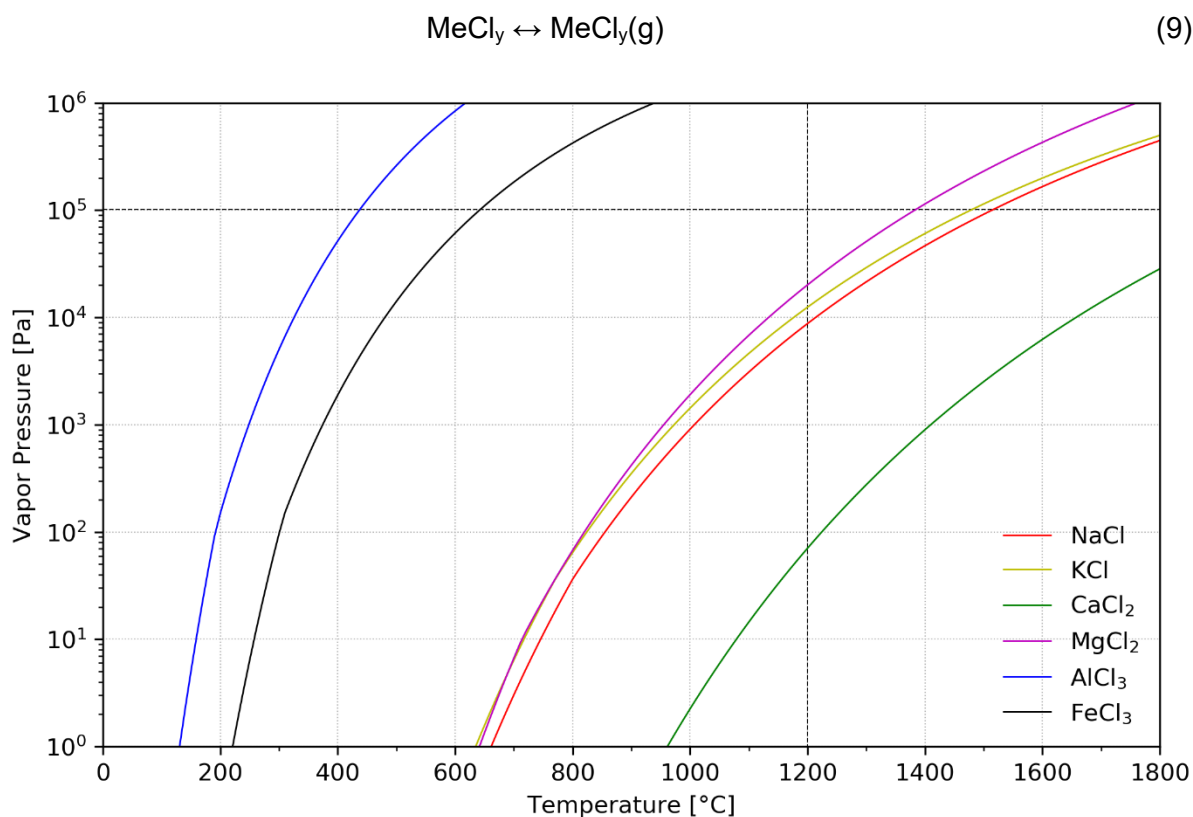


Figure 5: Comparison of the vapor pressure of assessed SCAs as a function of temperature

The trivalent chlorides AlCl_3 (blue line) and FeCl_3 (black line) are the first to develop a rapidly increasing significant vapor pressure above 1 Pa shortly after 100 °C and 200 °C respectively. Next, MgCl_2 (magenta line), KCl (yellow line) and NaCl (red line) begin to significantly evaporate at around 600 °C, showing lower increasing rates. Just slightly below 1000 °C evaporation of the least volatile CaCl_2 (green line) starts at a similar rate as MgCl_2 . Only AlCl_3 and FeCl_3 reach their boiling points at ambient pressure of 1 atm (black dashed horizontal line) before the chosen maximum process temperature of 1200 °C is obtained.

When in the gaseous state, two scenarios for further behaviour have been reported for different SCAs. NaCl tends to be inert, not reacting with neither O_2 nor $\text{H}_2\text{O}(\text{g})$ in the atmosphere. It therefore is discharged from the reactor without releasing chlorine, thus not being a suitable chlorination agent. [60, 66]

On the other hand, AlCl_3 shows high reactivity with oxygen and atmospheric water after evaporation, forming HCl available for chlorination of the metal oxides [60]. However, it releases its chlorine already at such a low temperature, at which the chlorination of metal oxides does not yet occur, thus it may not be suitable for the recovery of all metals [60]. This problem occurs predominantly in combination with metals which require high temperatures for chlorination such as silver, where CaCl_2 was reported to show the same behaviour. [68]

2.1.2 Direct oxidation of the solid chlorination agent

Another possible behaviour is the SCA's direct oxidation by atmospheric compounds O₂ or water, releasing its chlorine under formation of a stable metal oxide or hydride, depending on the presence and availability of water as well as temperature. These reactions are exemplary shown for MgCl₂ in Equations 10 and 11 and conducted for the other SCAs for always one mole metal chloride accordingly.



In Figure 6 the Gibbs free energy ΔG of given reactions is shown as a function of the temperature in degrees Celsius. Solid lines represent the reaction with oxygen as given in Equation 10, dashed lines consider reactions with water (Equation 11). Negative values indicate a shift of the reaction equilibrium to the product side, which in this case implies that chlorine release proceeds spontaneously.

Thermodynamically, the potential of chlorine release in dry and humid atmosphere was found to be AlCl₃>FeCl₃>MgCl₂ while CaCl₂, KCl and NaCl are chemically stable under given conditions and in the observed temperature range. Generally, reactions with water vapor are increasingly favourable at higher temperatures whereas the formation of chlorine gas in dry atmosphere slightly increases until reaching a thermodynamic maximum at moderate temperatures, after which it decreases. Thus, thermodynamics suggest that AlCl₃ favours formation of HCl above 600 °C and FeCl₃ above 1000 °C. MgCl₂ releases chlorine preferably in humid atmospheres, starting at around 600 °C. However, as seen before, some SCAs tend to evaporate already at low temperatures. In their gaseous state, reactivity thus chlorine release of mono- and bivalent SCAs increases drastically as shown in Figure 43 in the Appendix.

The behaviour of chlorine release via reaction with atmospheric compounds was described for MgCl₂ [69] and CaCl₂ [65]. They suggest a two step conversion in humid atmosphere. First, a conversion into Mg(OH)Cl or Ca(OH)Cl is observed, which decomposes under the formation of HCl at temperatures higher than 500 °C or 400 °C subsequently. [65, 69]

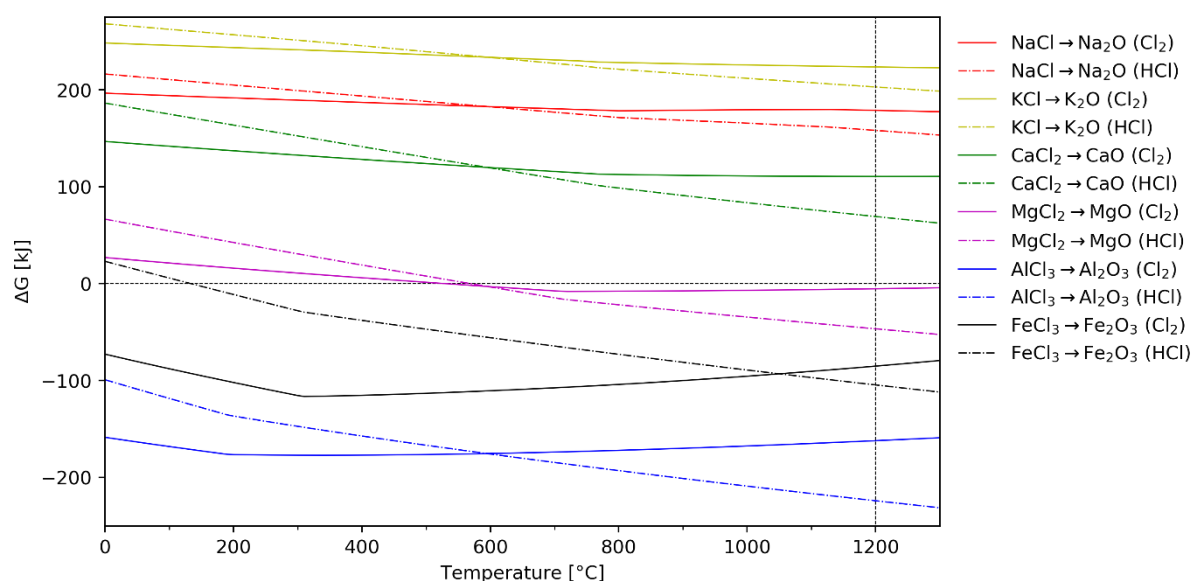
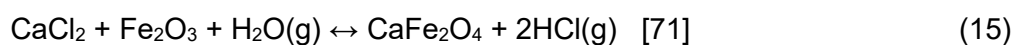


Figure 6: Comparison of different chlorine release potentials of selected SCAs

2.1.3 Formation of an intermediate compound

Finally, SCAs can form an intermediate compound via reactions with secondary compounds contained in the mixture or atmosphere, thus increasing or decreasing its chlorine releasing potential. For the considerably stable CaCl_2 , the presence of several components was found to significantly increase its decomposition. Equations 12–15 show examples of chlorine release reactions with sulphur, silicon and iron compounds:



A comparison of free Gibbs energy of given reaction paths with chlorine release potentials without the presence of secondary components are shown in Figure 44 (for CaCl_2) and Figure 45 (for MgCl_2) in the appendix.

Furthermore, certain thermodynamic requirements regarding the to be extracted metals contained in iron precipitation residues, must be met. To assess these, possible behavioural paths of metals during the chlorine calcination process must be identified.

2.2 Behaviour of to be extracted metal compounds

Different behaviours for various metals and their compounds during a chlorination process can be described, which are schematically categorized into three paths as shown in Figure 7.

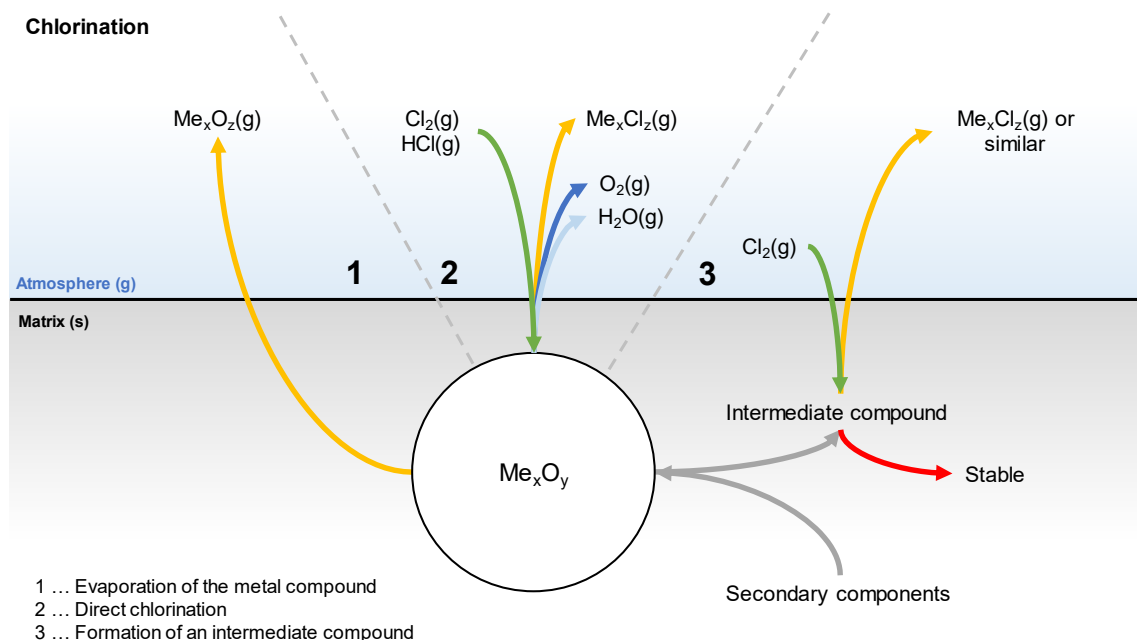


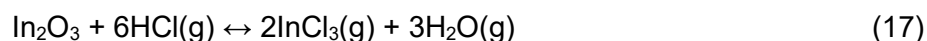
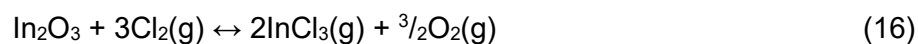
Figure 7: Different behavioural paths of a metal compound during a chlorination calcination process

2.2.1 Evaporation of the metal compound

If a metal is present in form of a volatile and stable component, it can be evaporated and discharged from the reactor via the off-gas without being chlorinated. This behaviour was documented for lead, which is preferably evaporated as PbO than chlorinated into PbCl₂ at temperatures higher than 800 °C [72]. However, this step also depends on other reaction conditions and can not be declared as generally valid. [73]

2.2.2 Direct chlorination of the metal compound

To be extracted from a given material mixture, the present metal compounds must form chlorides at process temperature ranges. In the course of this work, chlorination potentials are assessed for the metals indium, silver, zinc, lead and iron, whereas their presence in the form of their most stable oxides was assumed. This is largely the case for thermally treated residues. Based on these assumptions, chlorination reactions with gaseous chlorine and HCl are evaluated, which are exemplary shown for indium in Equations 16–17.



The results are shown in Figure 8. According to thermodynamics, lead oxide (blue solid line) can be chlorinated by $\text{Cl}_2(\text{g})$ even below $100\text{ }^\circ\text{C}$ followed by zinc oxide (magenta solid line) at slightly below $500\text{ }^\circ\text{C}$. Both indium oxide (red solid line) and silver oxide (green solid line) begin to form volatile chlorides with gaseous chlorine at temperatures above $600\text{ }^\circ\text{C}$. Iron oxide (black solid line) shows the lowest chlorination potential, remaining stable until temperatures higher than $1,200\text{ }^\circ\text{C}$. Through chlorination with $\text{HCl}(\text{g})$, chlorination potentials (dashed lines) are generally higher than with chlorine gas at moderate temperatures. However, they decrease with rising temperatures, reaching gaseous chlorine's potential at $800\text{ }^\circ\text{C}$, $700\text{ }^\circ\text{C}$ and $600\text{ }^\circ\text{C}$ for PbO (blue dashed line), ZnO (magenta dashed line) and In_2O_3 (red dashed line) respectively. Silver oxide (green dashed line) is easily chlorinated by gaseous HCl at all temperatures. Iron oxide (black dashed line) can be chlorinated with $\text{HCl}(\text{g})$ only until about $150\text{ }^\circ\text{C}$, where chlorine release of the SCA is still little. These results suggest that observed valuable metals can theoretically be chlorinated selectively, while iron stays oxidic.

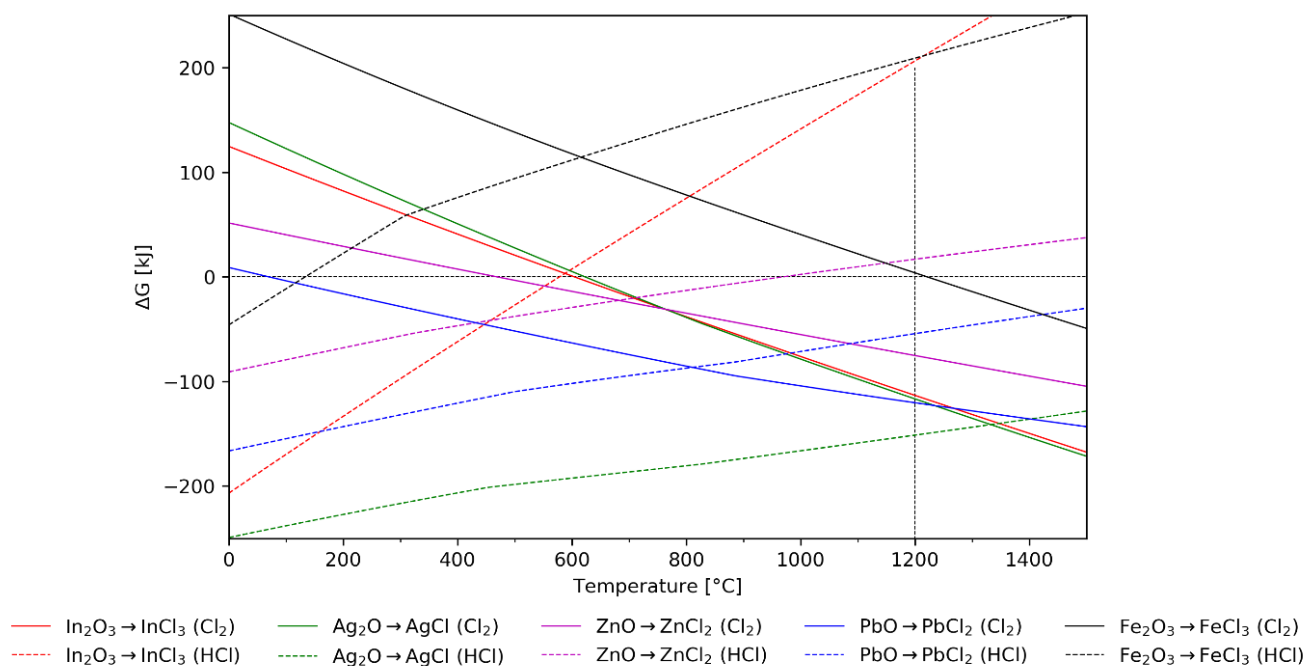


Figure 8: Comparison of different chlorination potentials of certain metal oxides with chlorine gas and HCl as a function of temperature (calculated in a closed system)

To sufficiently separate the chlorides from the iron fraction, they must be volatile at the applied temperature range. The boiling points of assessed metals, their most stable chlorides and, if applicable, their oxides as well as the difference between highest and lowest, ΔT_b , are shown in Table 3.

Table 3: Boiling points of assessed metals, their most stable chlorides and, if applicable, their oxides according to HSC Chemistry [67]

	Compound	T _b [°C]	ΔT _b [°C]
Indium	In	2072	1272
	InCl ₃	800 [74]	
Silver	Ag	2162	615
	AgCl	1547	
Zinc	Zn	907	1628
	ZnO	2360 [75]	
	ZnCl ₂	732	
Lead	Pb	1749	797
	PbO	1535	
	PbCl ₂	952	
Iron	Fe	2861	2545
	FeCl ₃	316	

Regarding the chlorides' boiling points, all chlorinated metals reach boiling at a temperature below 1200 °C apart from silver, which has by far the highest boiling point amongst assessed chlorides of 1547 °C. Iron and indium show large differences between metallic and chloride state of +2545 °C and +1272 °C respectively. Zinc chloride starts boiling only 175 °C lower than the pure metal while its oxide requires +1628 °C higher temperatures. This suggests that the necessity of conversion of a metal into its chloride for transferring it into the gaseous state varies. However, evaporation generally starts prior to reaching the actual boiling point and is described by the vapor pressure. To investigate volatile behaviour, vapor pressure curves are plotted in Figure 9.

At moderate temperatures, the volatility of all metals (solid lines) is considerably low, except for zinc, which starts developing a rapidly increasing vapor pressure at around 300 °C. At higher temperatures, also lead, indium and silver show significant vapor pressures higher than 1 Pa at around 700 °C, 900 °C and 1000 °C respectively. However, at moderate temperatures below 1200 °C (black dotted vertical line) and an ambient pressure of 1 atm (black dotted horizontal line), an extraction of them in their metallic state via the gas phase is limited by low vapor pressures. Considering a successful conversion into chlorine compounds (dashed lines) as shown before in Figure 8, their partial pressures all reach atmospheric levels and can therefore be easily evaporated and extracted through the vapor. This holds true for all metals, apart from silver. Vapor pressure of silver chloride (green dashed curve) starts to slowly increase at around 700 °C, reaching a maximum of around $3 \cdot 10^3$ Pa at 1200 °C. Iron(III) chloride (black dashed curve) demonstrates the highest vapor pressure among chlorine compounds until about 500 °C where it is surpassed by indium(III) chloride, showing a steeper

increase. Yet, as chlorination of iron(III) oxide does not occur below 1200 °C, the chloride is neither formed nor evaporated in the relevant temperature range.

Only for zinc (magenta dotted line) and lead oxide (blue dotted line) a stable gas phase exists, developing a significant vapor pressure above 1400 °C and 800 °C respectively. Only PbO can be evaporated in the applied temperature range, which coincides with information found in literature [72].

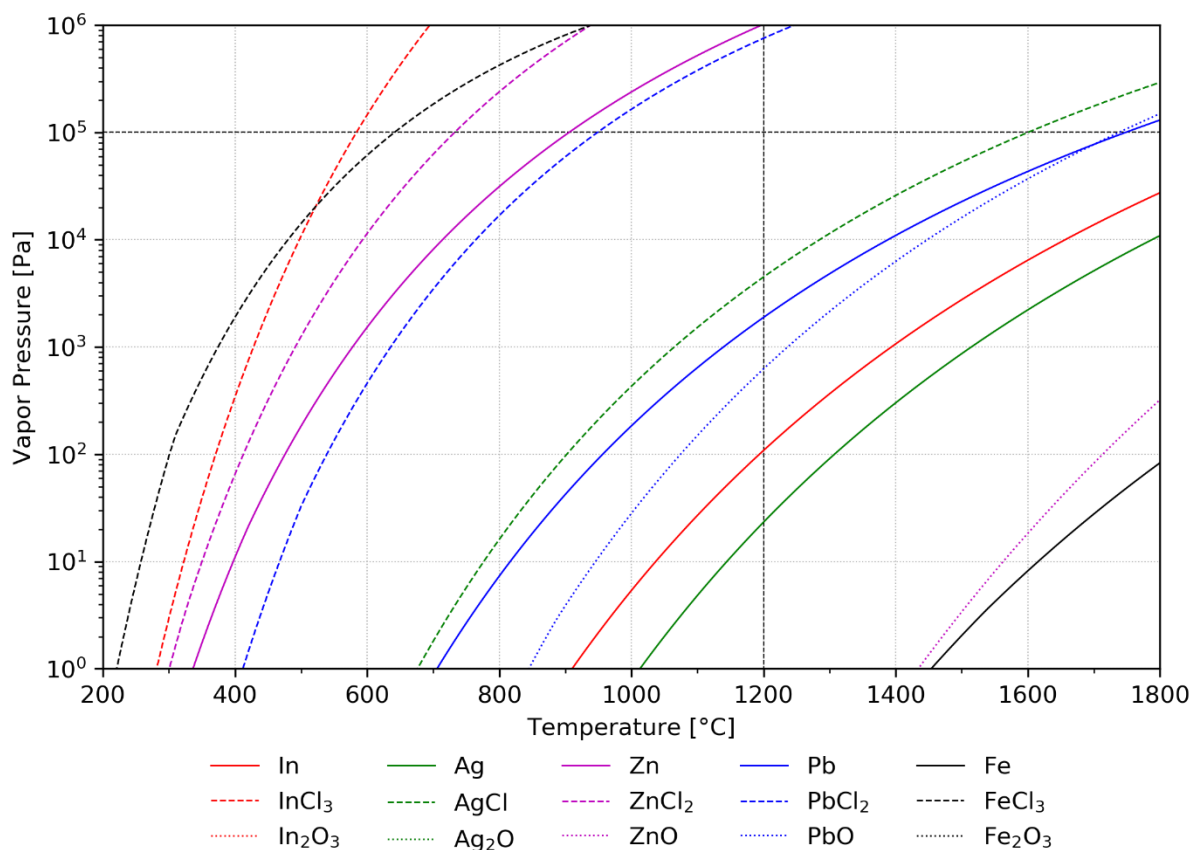


Figure 9: Comparison of vapour pressures of indium (red), silver (green), iron (magenta), zinc (blue) and lead (black) in their metallic form (solid lines), their corresponding chlorides (dashed lines) and, if applicable, oxides (dotted lines) as a function of temperature (calculated in a closed system)

To conclude, according to the thermodynamic assessment of chosen metals, a selective chlorination of the most stable oxides with chlorine gas or gaseous HCl and vaporization of the formed chlorides while iron remains in the solid residue is possible. Under observed conditions, the temperature should not surpass 1200 °C to avoid the formation of highly volatile iron(III) chloride. On the other hand, only high temperatures favour evaporation of silver chloride, which develops the lowest vapor pressure amongst assessed chlorides, reaching its boiling point at only 1547 °C. Selectively extracting silver from the iron based residue may therefore require a challenging balance of temperature. However, it must be noted that these results may vary significantly under realistic process conditions since a great variety of influences such as different atmospherical conditions are neglected.

2.2.3 Formation of a volatile or stable compound

For certain metals, a third possible behavioural path is described in literature, reacting with secondary components of the material matrix to form intermediate compounds. Zinc can be immobilized when ZnO reacts with Al₂O₃, forming a more stable aluminate ZnAl₂O₄ [72, 73]. On the other hand, extraction can be improved by formation of volatile double salts through reactions with alkali metals like Na or K. Kurashima et al. describe the evaporation of KZnCl₃ [72], while Chan and Kirk identified the chemical phases Na₂ZnCl₄·3H₂O and K₂ZnCl₄ [76]. The same behaviour was observed for lead, being converted into the double salt KPb₂Cl₅ [76]. These findings show that present secondary components in the material matrix can influence the chlorination process of to be extracted metals either positively or negatively.

2.3 Direct reaction between the metal compound and SCA

So far, behaviours of chlorination agents and to be extracted metal compounds have been evaluated separately. However, when direct contact between these two species exists, a direct reaction is possible. The SCA's cationic group X is bound by oxygen delivered by the metal oxide MO, which on the flipside consumes the SCA's chlorine under formation of the metal chloride. [76] The scheme of this reaction is described in Equation 18:



A comparison of thermodynamic reaction potentials of previously assessed chlorine release or chlorination paths with a direct reaction between MgCl₂ and ZnO is shown in Figure 10.

The results show that thermodynamic chlorination potential of ZnO with gaseous HCl (green dashed line) and chlorine (green solid line) is higher than of direct reaction with MgCl₂ (magenta solid line). However, this requires already available chlorine released by the SCA. Chlorine release of MgCl₂ with oxygen (red solid line) or atmospheric water (red dashed line), is enabled only above 525 °C and 575 °C respectively, while the direct reaction path (magenta solid line) proceeds naturally at already lower temperatures of about 475 °C. This suggests that the direct reaction is the preferred pathway in the MgCl₂-ZnO-system.

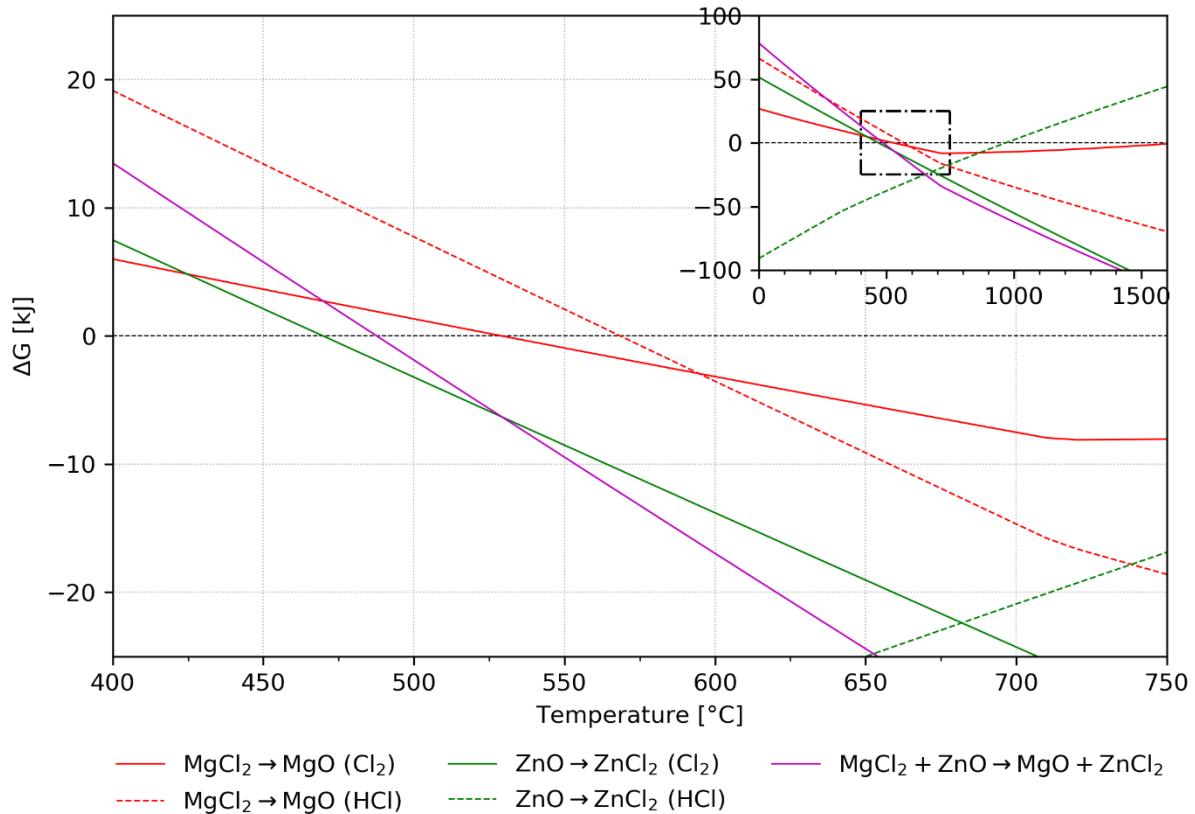


Figure 10: Comparison of thermodynamic reaction potentials of previously assessed chlorine release or chlorination paths with a direct reaction between MgCl_2 , ZnO

2.4 Summary of potential influences on chlorination processes

In given theoretical evaluations, certain influences on chlorination processes have been assessed. Thermodynamic reaction potentials and volatile behaviour of different chlorination agents and metals have been compared, considering dry and humid atmospheres and dependency of temperature. It was found that secondary compounds present in the material mixture can both increase and decrease success of chlorination processes. To summarize, observed influences include:

- Temperature and pressure,
- type of chlorination agent,
- type of metal compound, and
- presence of water and secondary components

However, all results are based on simplistic assumptions, neglecting interdependencies and variability of numerous other relevant parameters, aside of kinetic aspects.

3 Thermochemical modelling of advanced chlorination processes

To assess a greater variety of influences on chlorination reactions, a comprehensive simulation algorithm has been developed in the course of this work.

3.1 Approach and methodology

FactSage Thermochemical Software and Databases v8.0 [77] was used for calculations. Its software module Equilib simulates the reaction of individually selectable compounds according to thermodynamic laws and values contained in a comprehensive database. The module consists of four windows, whereof two are meant to define input and adjust reaction conditions. First, the reactants must be defined by their quantity and species in the “Reactants” window. For quantity, input of either moles or masses is possible while species are defined by the substances’ chemical formulas. Two variables <A> and are provided for iteration of a range of species’ quantities in one run. If preferred, initial conditions can be defined, which include physical state or different solid phases, if applicable. In the second step, a set of parameters must be set in the “Menu” window. This includes products’ compound species, where desired aggregate states are selected. If applied in the reactants window, variable <A> must be defined by three consecutive numbers representing minimum, maximum and step size. The same method can be applied to set a range of different temperatures and pressures. Variable can represent only one fixed number. By clicking “Calculate >>”, calculations are performed according to the given input.

The results are presented in the “List” window, where all output species are listed alongside their quantity categorized by their aggregate state and the “Results” window, where a summary for every single calculation is given in a text format. Exporting output data is possible in various forms, including Microsoft Excel-files. To do so, product species and properties desired to be exported must be selected.

3.1.1 Limitations of FactSage Equilib’s input interface

The described pathway for implementing input parameters into FactSage comes with certain limitations. Firstly, only one variable for reactant quantity can be applied, iterating always linearly. Mathematical operations can be conducted to vary the variable for different reactants, however, they can not be altered independently. Thus, one individual run must be manually conducted for each parameter of observations, where only one variable iterates while the others are fixed. Moreover, no advanced functional relationships can be implemented between different reactants. Aside functional limitations, FactSage Equilib is not capable of performing

more than 9999 calculations for up to 48 reactants per run. Only Excel sheets with less or 256 columns can be exported, which presents the maximum number of assessable output species per run.

These limitations drastically decrease the software's potential application for this work's purpose. If chlorination potentials for a certain metal with variable amounts of different SCAs is to be assessed, one calculation run must be conducted for each individual scenario, rapidly leading to an immense number of trials, which is associated with a degree of labour that would soon exceed the scope of this work. As a consequence, a new method of parameter input was developed, using the "Reaction Table" function.

The reaction table displays values for temperature, pressure and quantities of manually added reactant species, where each row represents one reaction trial. These values can either be manually inserted or imported from a simple text file. To create a suitable file including desired input parameter variations, an algorithm was developed in the Python 3 programming language.

3.1.2 Algorithmic automatization of reaction parameter input

The objective of this development is to obtain an automatized method to transfer easily implementable input criteria into a text file which represents a set of chlorination roasting scenarios to be directly imported and calculated by the thermochemical computation software. Thus, a profound analysis of possible influences can be conducted which would barely be feasible manually. First, a set of desired parameters to be assessed is defined. These include:

- Type of metals in various compounds,
- type and relative quantity of SCAs,
- temperature and pressure ranges,
- variable atmospheric conditions, and
- type and relative quantity of secondary compounds.

These parameters must be set by both qualitative and quantitative input. To define reactants, four strings must be defined by implementing chemical formulas of deserved metals, SCAs, secondary compounds and atmospherical components, which will be processed as separate categories subsequently. There are four available forms of metallic compounds, namely oxide, sulfate, hydride and metallic, which can be added to the metal reactant category by defining their associated Boolean as true. For quantifying the species, a minimum, maximum and step width can be defined as integers or floats if a range is desired. If only one single quantity is sufficient for a particular run, the range-Boolean can be set to false, whereas only the given maximum amount is considered. The same holds true for temperature and pressure, whereby logarithmic ranges can be applied for the second. Furthermore, two stoichiometric functions

are available, which set input quantities of metallic compounds and SCAs in relationship. The first option adjusts the reactants' quantities, so that one mole of metal contained in the compound reacts with one mole of chlorine contained in the SCA. On the other hand, the actual stoichiometric quantity of chlorine, which is needed to form the chloride of present moles of metal is calculated. Additionally, a factor can be applied, which allows assessing different stoichiometric ratios, alternatively in a range as mentioned above.

For processing and transforming the given input parameters into an implementable format, the Python libraries NumPy [78], Pandas [79] and chemlib [80] are used. At first, given reactant strings are joined alongside pressure and temperature into a list, which is set as columns of a pandas DataFrame. Subsequently, numeric values are converted into lists containing the given value range. Finally, the DataFrame is filled row by row, iterating through an expansive set of for-loops. Stoichiometric calculations are applied directly in the filling-step, using chemical data provided by chemlib library. Thus, every possible combination of the input parameters is contained as one row of the final DataFrame-matrix, representing one chlorination scenario accordingly. If the maximum of 9,999 rows is surpassed, the loops break and an error message is printed. In such cases, adjustments of the input criteria must be carried out to obtain less scenarios per run. The final matrix is exported as an Excel-file which must be saved as text-file after removing index and columns manually, as FactSage can not read automatically generated .txt files by Python. The so created text file is subsequently imported into the FactSage Equilib model via "Table > Reactants Table > Import Table > from simple text file without headers ...". It is crucial to set the right quantity unit as desired before processing to the calculation.

After running the calculations in FactSage Equilib, the results are exported as an Excel file, where the product quantities of selected species are contained for every scenario, represented by one row. Thus, the product file also is a matrix, bearing the same number of rows as the generated input matrix. Therefore, they can be imported into and joined in a second Python algorithm. There, each chlorination scenario can be automatically analysed by the calculation of values, which describe extraction efficiencies. To evaluate extraction of assessed metals, the total quantity of their gaseous state in the reaction product $N_{\text{Met,product,(g)}}$ was selected as output species. Extraction values are calculated via Equation 19 subsequently:

$$E_{\text{met}} = N_{\text{met,out,(g)}} / (N_{\text{metComp,in,(s)}} \cdot n_{\text{met,metComp}}) \quad (19)$$

E_{met} [-] is the extraction rate, $N_{\text{met,out,(g)}}$ [mol] the number of gaseous moles of the metal in the reaction's product as calculated by FactSage Equilib, $N_{\text{metComp,in,(s)}}$ [mol] the number of reacting moles of the input metal compound and $n_{\text{met,metComp}}$ [-] is the number of moles of metal per mole metallic compound. The extraction rate demonstrates a representative value for evaluating the general vaporization potential of an assessed metal. However, it does not

contain any information about the gaseous components, thus no insight into the actual chlorination process is given. To overcome this limitation, a more detailed evaluation of individual components must be conducted. As FactSage Equilib does not support a joint result exportation of more than 256 species, which is surpassed in almost all relevant cases, a full automatization of the in-depth analysis was not achieved. Yet, a manual selection of relevant components is possible, enabling a further investigation of chlorination scenarios that show unexpected results in the preceding more perfunctory run.

3.2 Results

Numerous simulations have been conducted according to the aforementioned procedure to obtain a more profound understanding of how and to which extent the variation of several parameters influence metal extraction during a chlorination process. In this chapter, an overview of selected findings is presented. As the simulation algorithms offer an almost infinite palette of individually variable parameters, given results represent only a limited set of examples. A selection of further calculations which are not mentioned in the written text can be found in the Appendix.

3.2.1 Assessment of individual metals

A series of simulations has been conducted to observe behaviours of individual metals. Therefore, in every given reaction, only one type of metal is chlorinated under various conditions. Extraction efficiencies are expressed in form of the extraction rate.

Firstly, parameters that are expected to have a major influence on extraction rates are examined. These include temperature, pressure and stoichiometric quantity of SCA. For this series, the metals indium, silver, zinc, lead and iron are present in their oxidic form and are chlorinated using NaCl, MgCl₂ or AlCl₃ as SCA. Unless otherwise stated or iterated, simulation's pressure is 1 atm, metal input is 100 mol of the contained metal, chlorine stoichiometry 1.0 and the atmosphere is inert, containing Ar and N₂. To take the existing vapor pressure into account, a number of $1 \cdot 10^7$ mol N₂ is always added to obtain more realistic vaporization behaviours.

- Influence of temperature on individual metal's extraction

First, the influence of temperature on the individual extraction of assessed metals is evaluated. The results are shown in Figure 11. Generally, extraction rates increase with increasing temperature regardless of metal type or applied SCA. All metals from investigated oxides are extracted completely using MgCl₂ (dashed lines) and AlCl₃ (solid lines). Iron chloride begins evaporating at temperatures lower than 100 °C, reaching complete extraction just before

370 °C when chlorinated with AlCl_3 . Using MgCl_2 , iron extraction starts increasing noticeably only at higher temperatures of around 350 °C, just after complete evaporation of indium-, silver- and lead chloride. At 424 °C iron vaporization reaches a plateau. Since the objective is the separation of valuable metals from the predominant iron phase, its extraction rate plays a central role for applicability of the process. Therefore, it is thoroughly analysed when irregularities occur as in this case. To assess the observed vaporization behaviour of iron, a more profound calculation run was conducted to examine the formation of different compounds in the Fe_2O_3 - MgCl_2 -system. The results for the same conditions and inputs as shown in Figure 11 of 50 mol Fe_2O_3 iron oxide and 150 mol MgCl_2 are presented in Figure 12.

Results show that the stagnation of iron extraction is caused by the formation of a solid compound $\text{MgO}\cdot\text{Fe}_2\text{O}_3$ (blue solid line), in which a maximum of 75 mol-% of the entire iron input is bound in a temperature range of 424–455 °C. From there on, the component's share decreases rapidly until reaching non-significant levels at 486 °C. At the same range, the SCA's magnesium begins forming pure MgO and iron is increasingly released, thus extraction rate resumes rising. Formation of $\text{MgO}\cdot\text{Fe}_2\text{O}_3$ takes up increasing until reaching 1.1 mol at 700 °C, where a transition to Fe_2O_3 (magenta solid line) takes place. This behaviour is also seen as a slight decrease of iron extraction in Figure 11, which vanishes at 764 °C, where all present iron is in a gaseous state. The compound analysis also shows the transition of the trivalent FeCl_3 (black dashed line) to the bivalent FeCl_2 (yellow dashed line) at temperatures higher than 487 °C. Consequently, less chlorine is needed for iron chlorination, which is why formation of gaseous Cl_2 is observed. This shows that the process temperature is a major factor in determining which iron compound is formed. The shortcoming of the algorithm's stoichiometry calculation will be discussed later.

Back to Figure 11, indium and zinc show similar extraction behaviours, reaching complete evaporation at 280 °C and 300 °C respectively with both MgCl_2 and AlCl_3 . Silver chloride is evaporated at last, reaching 100 % at around 670 °C. Extraction rates with NaCl applied as SCA reach their maximum at higher temperatures in the order lead, silver, zinc and indium. Iron from its oxide does not get significantly extracted by NaCl even at temperatures as high as 1300 °C. According to given results, assessed valuable metals can only be selectively extracted in respect to iron using NaCl as SCA and processing at a temperature of 1200 °C. Using MgCl_2 , indium, zinc and lead can be removed at temperatures of 400 °C while a residue of iron and silver is expected. However, in this scenario, individual metals are chlorinated with stoichiometric amounts of chlorine. This is not the case when being present in a mixture, where competition for available chlorine exists between the metal compounds.

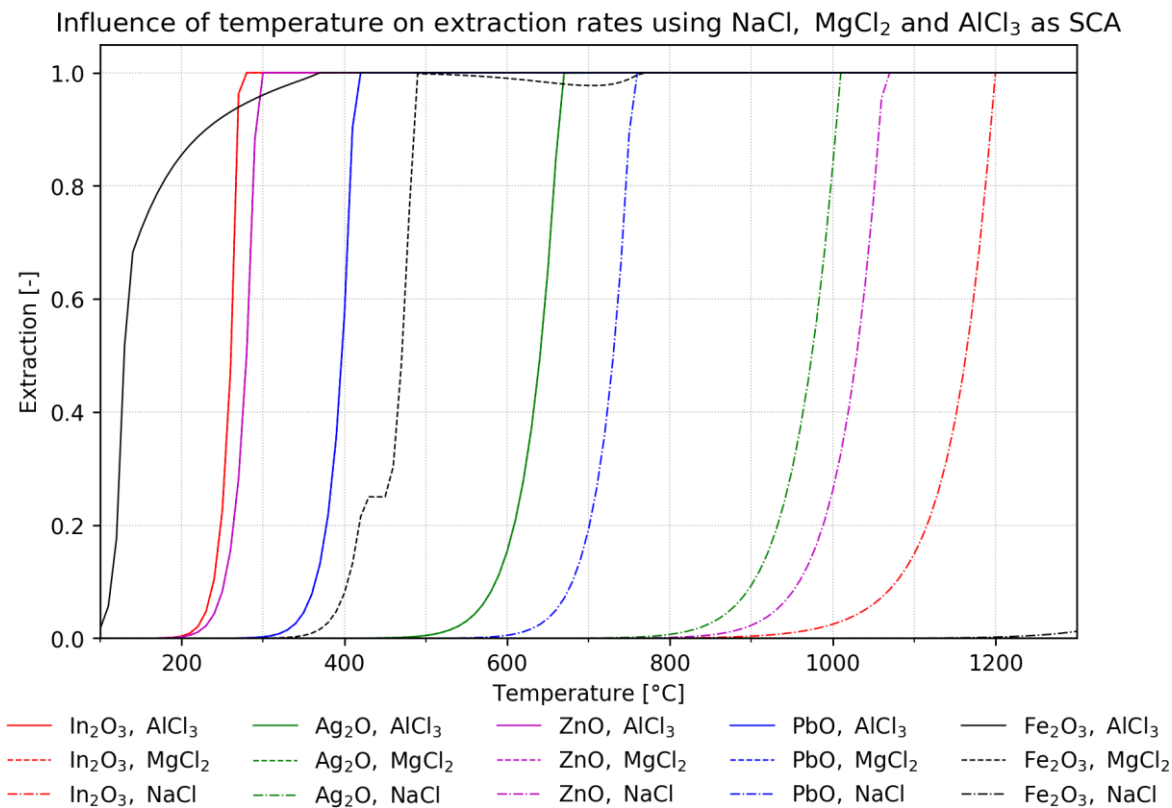


Figure 11: Influence of temperature on extraction rates of In, Ag, Zn, Pb and Fe using NaCl (dash dotted lines), MgCl₂ (dashed lines, mostly invisible because of overlapping) or AlCl₃ (solid lines)

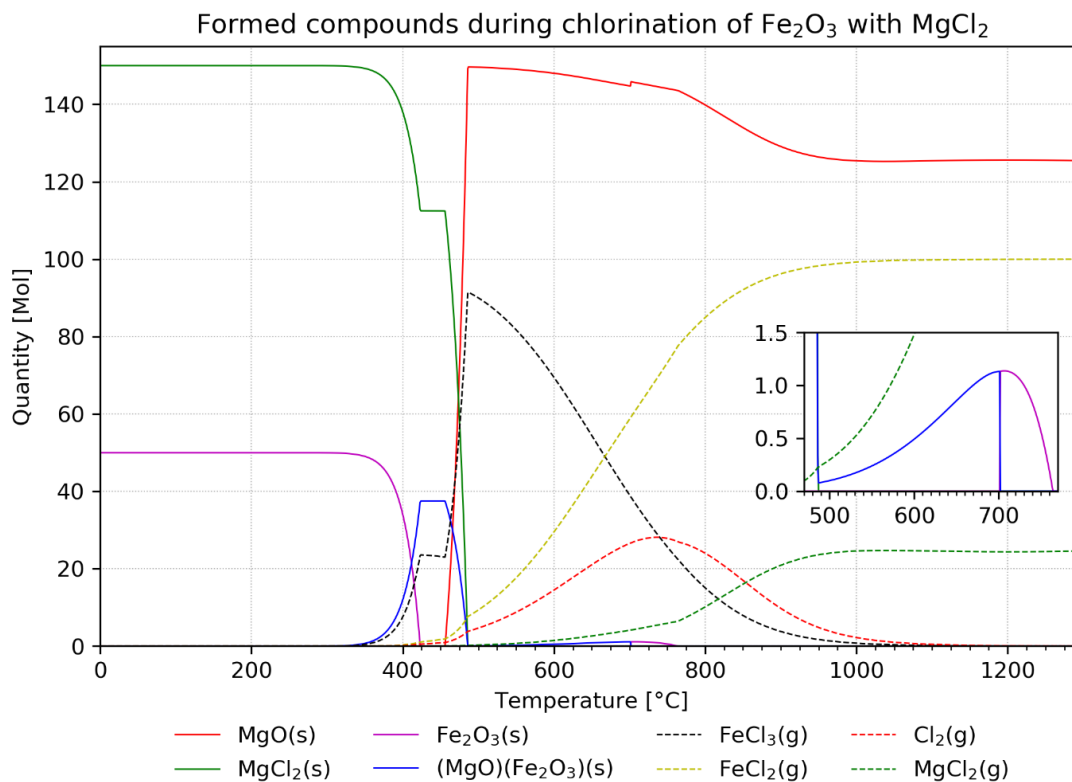


Figure 12: Formation of various solid (solid lines) and gaseous (dashed lines) compounds in the Fe₂O₃-MgCl₂-system as a function of temperature

- Influence of pressure on individual metal's extraction

When evaluating the influence of different pressures on extraction rates, significant differences are only observed when applying NaCl as an SCA. These dependencies of pressure shown in Figure 13 are potentially relevant for operative process design, whereas other observed SCAs generally result in high extraction rates at all assessed conditions.

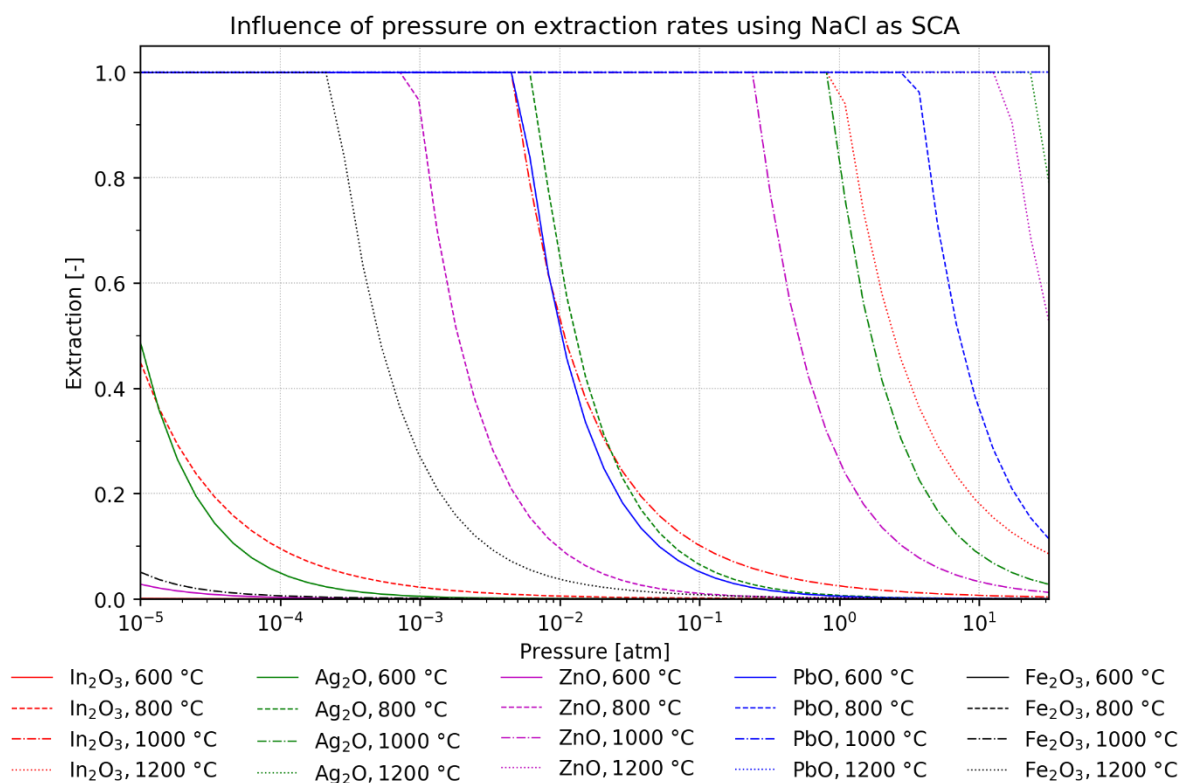


Figure 13: Influence of pressure on extraction rates of assessed metals using NaCl as SCA

As expected, vaporization generally decreases with increasing pressure. The positive interdependence of extraction and temperature can be observed well in the case of silver (green lines), which is fully evaporated until continuously higher pressures when following lines of higher temperatures (solid → dashed → dash dotted → dotted). At a vacuum of 10^{-5} atm and 600 °C, only lead reaches full extraction, while 50 % of silver chloride is evaporated. At the same pressure (10^{-5} atm) and a temperature of 1200 °C (dotted lines) all assessed metals are completely evaporated. Increasing the pressure into the range of 0.01–0.8 atm enables a possible selective chlorination of all metals, while major amounts of iron remain in the residue. The same holds true for pressures between 10^{-5} – $10^{-2.3}$ atm at 1000 °C (dash dotted lines). The results for application of MgCl₂, AlCl₃, CaCl₂ or FeCl₃ are shown in the appendix. In contrast to the significant differences when using NaCl as SCA, almost all metals are fully extracted at all investigated pressures and temperatures with MgCl₂, AlCl₃ or FeCl₃. Only silver shows a decrease in extraction at 600 °C, where the rate drops significantly when pressure increases to slightly higher than 0.1 atm. This indicates that no selective vaporization of valuable metals

can be achieved by the variation of pressure in the assessed range of 10^{-5} – $10^{1.5}$ atm in these cases.

- Influence of chlorine stoichiometry on individual metal's extraction

Next, a quantitative variation of chlorine stoichiometry is assessed. In this scenario, stoichiometry [mol Cl/mol Cl-demand] refers to the ratio of the theoretical amount of available chlorine [mol Cl] delivered by the SCA to the quantity of chlorine [mol Cl-demand] which is needed for a complete chlorination of the moles of metal contained in the input compound. For this calculation, the valency of the metal's oxidic state is considered to remain unchanged. One mole of a mono-, bi- or trivalent metal requires one, two or three moles of chlorine, respectively. The results for the application of various amounts of AlCl_3 as SCA at various temperatures, a pressure of 1 atm and inert atmosphere is shown in Figure 14.

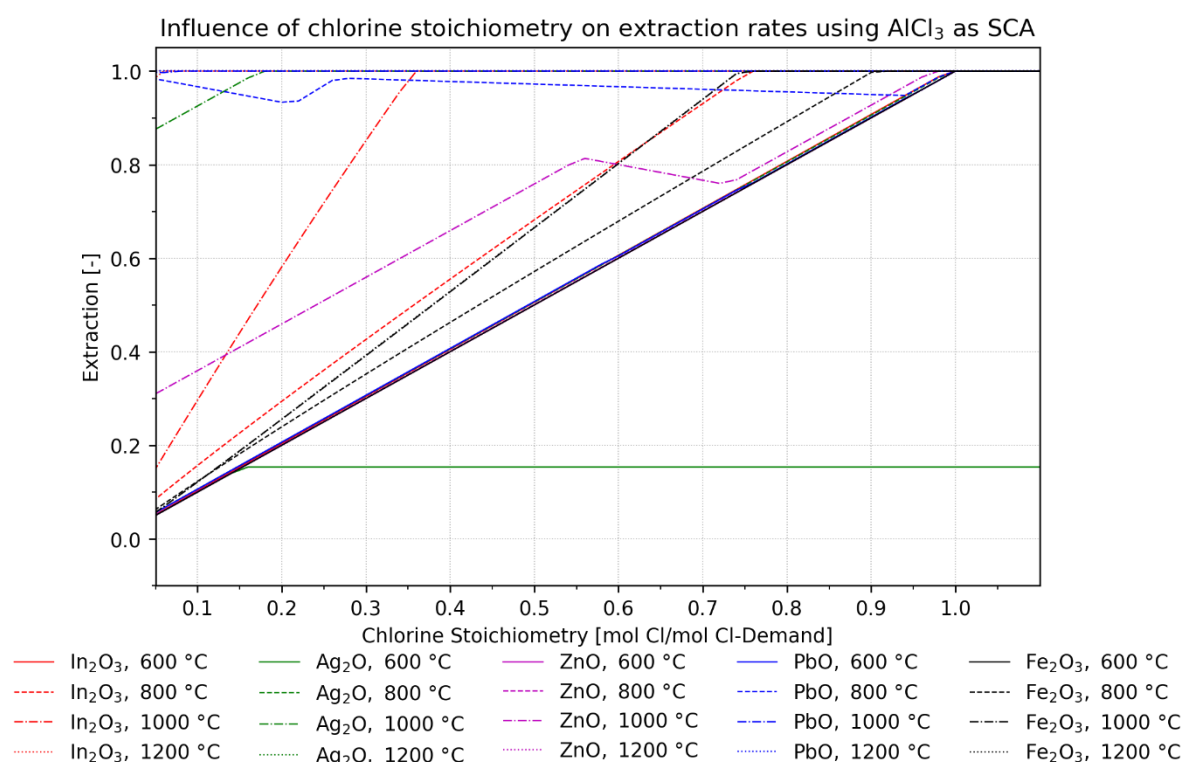


Figure 14: Influence of stoichiometry on extraction rates using AlCl_3 as SCA at various temperatures

At 600 °C (solid overlapping lines) all metals show the same correlation of extraction rates and increasing chlorine stoichiometries except for silver, of which only around 15 % evaporate. Higher temperatures result in different behaviours among assessed metals as indicated by dashed and dash dotted lines.

Zinc shows a declining extraction rate at 1000 °C (magenta dash dotted line) and stoichiometries between approximately 0.56–0.73. To evaluate the reason for this behaviour, an in-depth compound analysis for this scenario is conducted, which is shown in Figure 51 in

the Appendix. When chlorinating ZnO with AlCl_3 , a solid compound ZnAl_2O_4 (magenta solid line) is formed under given conditions, which binds gaseous zinc in the solid state. As the simultaneous presence of Zn(g) and $\text{O}_2(\text{g})$ is unlikely under given conditions, this phenomenon displays a shortcoming of the simulation which is caused by the large amounts of added $\text{N}_2(\text{g})$. While this addition leads to discrepancy in this case, it is generally necessary to model the effect of vapor pressure for other compounds, where no adverse effects are observed.

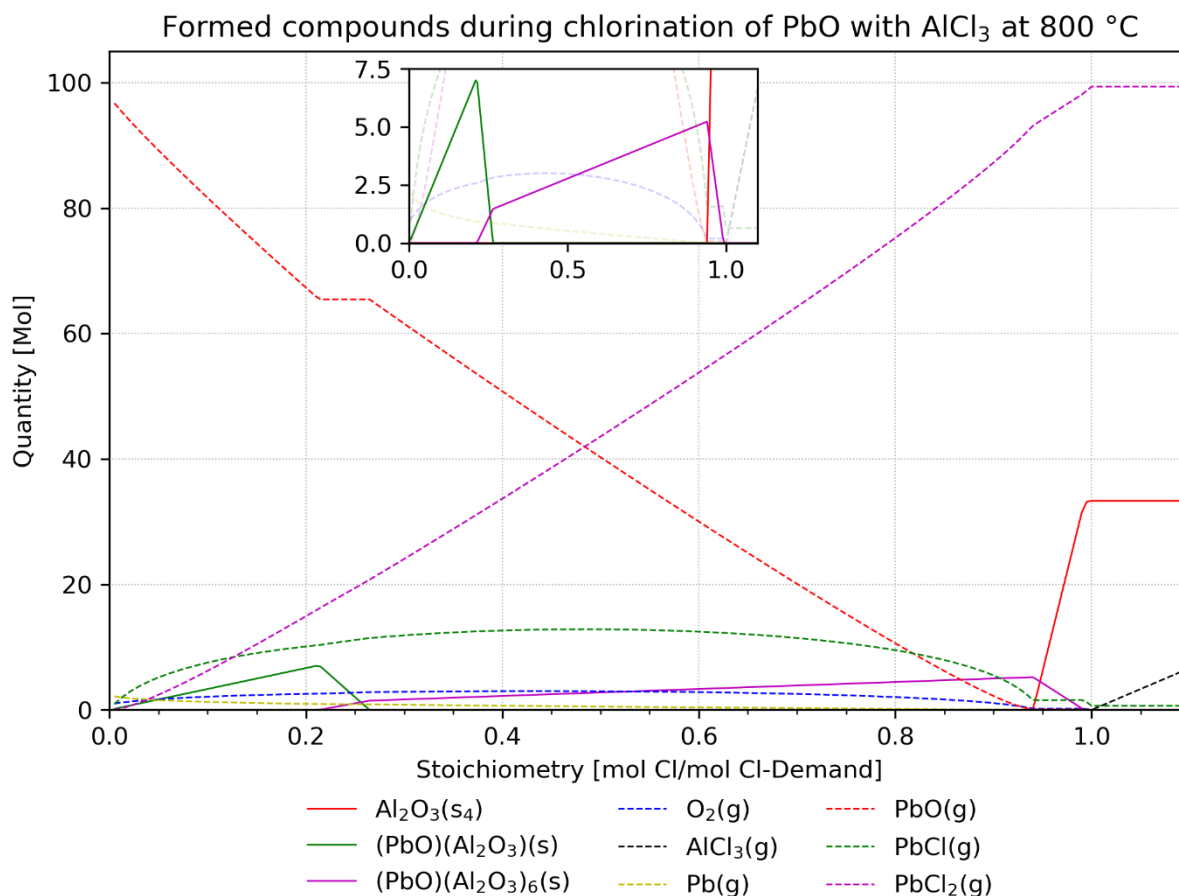


Figure 15: Formation of various solid (solid lines) and gaseous (dashed lines) compounds in the $\text{PbO}-\text{AlCl}_3$ -system as a function of chlorine stoichiometry (800 °C)

Extraction rates of lead (blue lines in Figure 14) start at almost 100 % at 800 °C, as the lead oxide is present in the gaseous state. Yet, extraction is declining with increasing addition of SCA. Through a compound analysis shown in Figure 15 that behaviour is explained by the formation of the solid compound $\text{PbO}\cdot\text{Al}_2\text{O}_3$ (green solid line), which binds increasing amounts of lead in the solid phase. Between stoichiometries of 0.21 and 0.26, a transition towards the formation of $\text{PbO}\cdot(\text{Al}_2\text{O}_3)_6$ (magenta solid line) takes place. In this period, binding of lead from gaseous PbO stagnates while formation and evaporation of lead chloride (magenta dashed line) continues increasing, thus a local maximum extraction rate of 98.4 % is reached. When applying more AlCl_3 , lead resumes being bound in a solid lead-aluminium-compound, which again lowers extraction rates. As the secondary compound binds more aluminium per mole

than the first one, lead vaporization decreases at a lower rate than initially. At stoichiometries higher than 0.96, formation of Al_2O_3 (red solid line) starts, enabling a complete lead extraction. As in the case of zinc, the binding of the to be extracted metal in a solid phase impacts only its gaseous oxide, while conversion and evaporation of the chloride compound is not affected significantly. No such behaviours are observed when using MgCl_2 or NaCl as SCA, as shown in Figure 52 and Figure 53 in the Appendix.

The different increasing rates of indium extraction (red lines, Figure 14) at different temperatures root in a shortcoming of the stoichiometric calculation. At 800 °C indium fully evaporates at an indicated stoichiometry of 0.76. At this point, it is present as 67.3 mol-% InCl_2 and only 28.7 mol% InCl_3 as an in-depth analysis shows. At 1000 °C, full extraction occurs even sooner at 0.36 because 93.3 mol-% are present as the monovalent InCl . As only the trivalent chloride InCl_3 is considered for stoichiometry calculations, an excess of chlorine is reached at already lower values than 1.0 for higher temperatures, resulting in sooner vaporization. At a temperature of 1200 °C a complete indium extraction is reached regardless of chlorine addition due to the formation of gaseous In_2O , whose share decreases in favour of InCl until an indicated stoichiometry of 0.23.

Iron shows a similar behaviour, favouring FeCl_2 instead of FeCl_3 at temperatures higher than 490 °C, as can also be seen in Figure 12. At 800 °C (black dashed line), iron reaches full extraction at an indicated stoichiometry of 0.92, where 85.3 mol-% and 14.7 mol-% are present of the bivalent and trivalent chlorides respectively. At 1000 °C and higher (overlapping black dotted and dash dotted line), no significant amounts of FeCl_3 are formed anymore. As vapor composition continuously changes with the variation of numerous parameters, no easy calculation method can be applied to always guarantee a correct chlorine availability according to demand. Therefore, stoichiometry must be interpreted as the theoretically maximum required amount for all further evaluations. However, the shown strictly positive correlation of iron extraction and increasing quantities of applied SCA is nevertheless valid.

- Qualitative assessment of further influences

To assess further influencing parameters, although quantitative iterations are possible in the same way as for preceding simulations, qualitative evaluations are carried out due to the limited scope of this work. In this study, one calculation run including scenarios of various forms of metal compounds, secondary compounds and atmospheres is conducted. For modelling the presence of secondary compounds, the same mole quantity as the to be extracted metal is added as a reactant. The same amount of the according gas is additionally applied, when considering different atmospherical conditions. The results are presented as deviation from mean extraction [%]. This value is calculated as percentage deviation of the extraction achieved by application of one individual parameter (e.g. NaCl) of the considered set of

parameters (e.g. SCA) from the overall mean extraction of all assessed scenarios for each metal individually. Therefore, the sum of all individual deviations of one set of parameters is always 0. For a better understanding, the deviation values for extractions of silver applying various SCAs at 800 °C are shown in Figure 16 and Figure 17.

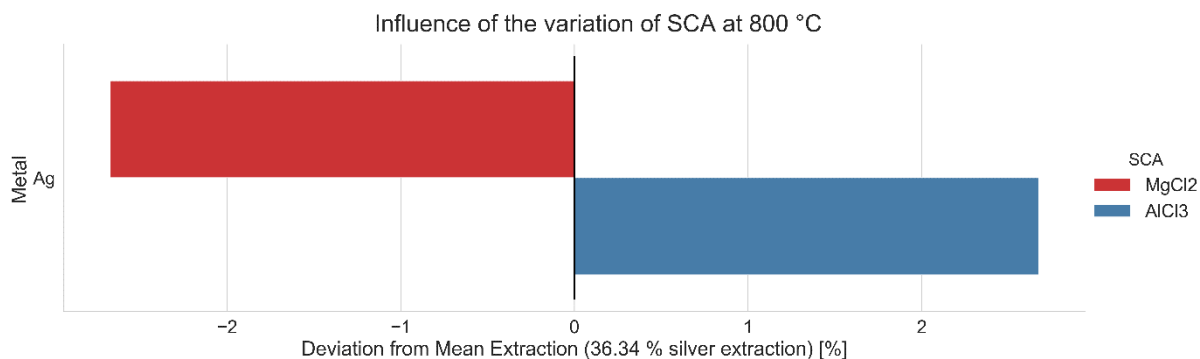


Figure 16: Influence of the variation of the SCA including MgCl₂ and AlCl₃ expressed as the deviation from mean silver extraction (36.3 %)

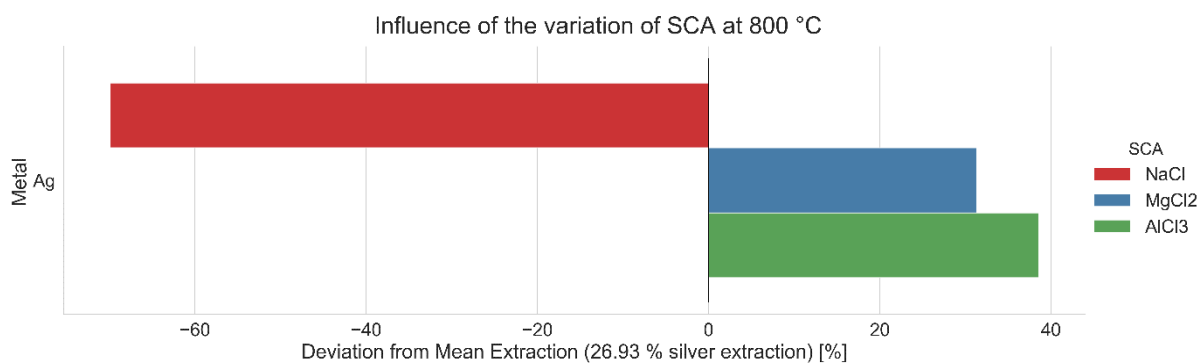


Figure 17: Influence of the variation of the SCA including NaCl, MgCl₂ and AlCl₃ expressed as the deviation from mean silver extraction (26.9 %)

In the first shown scenario MgCl₂ and AlCl₃ are applied as SCA at 800 °C. The use of MgCl₂ achieves extractions which are around 2.7 % below the average value (35.4 % silver extraction) calculated by the mean of both considered SCAs, which is 36.3 % silver extraction in this case. Consequently, application of AlCl₃ reaches values 2.7 % above the mean extraction (37.3 % silver extraction). When NaCl, whose application results in only 8.1 % silver extraction, is additionally assessed, the mean extraction is reduced to 26.9 % silver extraction thus new deviations are obtained for each individual SCA accordingly (-69.9 % for NaCl, +31.3 % for MgCl₂, +38.5 % for AlCl₃). Through this calculative approach, conclusions about the positive or negative influence of various conditions can be drawn for each set of parameters. Due the low chlorination potential of NaCl, it will be excluded for future considerations. The following results only represent an exemplary selection of all potentially assessable sets of parameters. The metals indium, silver, zinc, lead and iron are introduced as their most stable oxides, sulfates, hydrides or in their metallic state. Chlorine is delivered by

the SCAs CaCl_2 , MgCl_2 , AlCl_3 and FeCl_3 while SiO_2 , CaF_2 , FeS_2 and K_2SO_4 are evaluated as secondary compounds. Furthermore, reactions occur in a reductive (CO), oxidative (O_2), humid (H_2O), SO_2 - or inert (Ar -) atmosphere. The pressure is set to 1 atm, chlorine stoichiometry to 1.0 and temperature includes 800 and 1000 °C. The results are graphically shown in Figure 18–Figure 21 while all numeric values of this simulation run can be found in Table 6 in the Appendix.

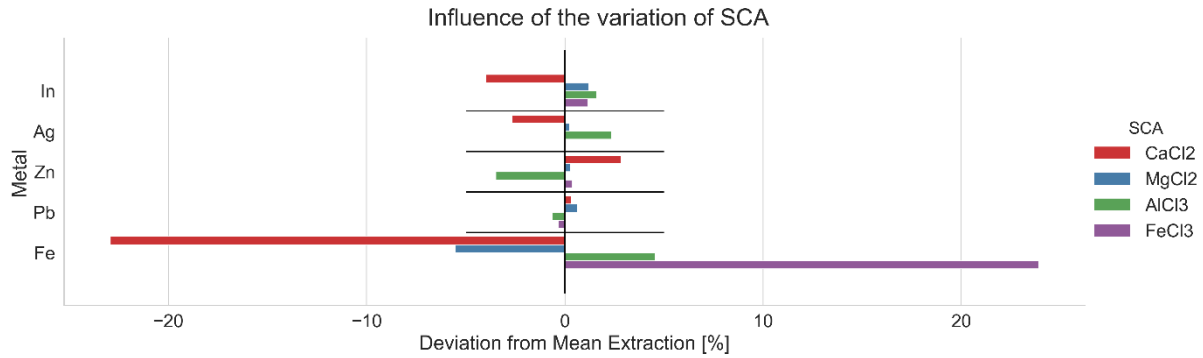


Figure 18: Influence of the variation of SCA on extraction rates

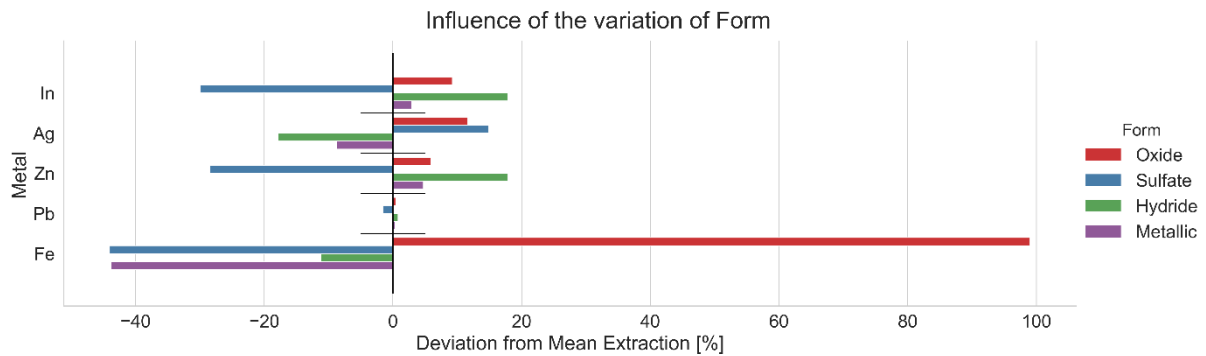


Figure 19: Influence of the variation of the metal's form on extraction rates

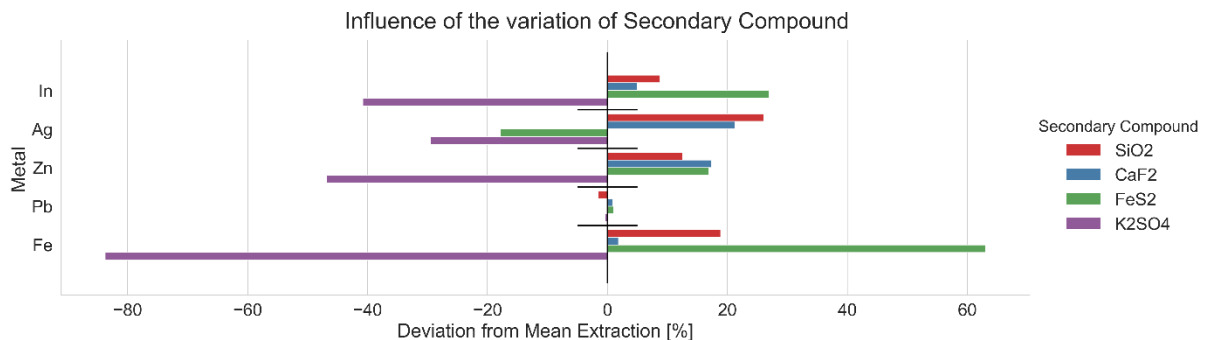


Figure 20: Influence of the variation of secondary compounds on extraction rates

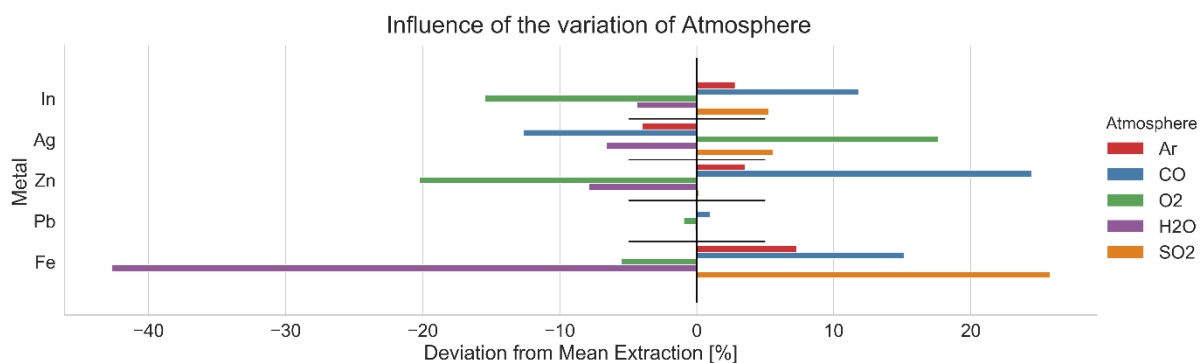


Figure 21: Influence of the variation of the atmosphere on extraction rates

Considering all given scenarios, lead shows the highest mean extraction rate of 99.0 %, followed by indium, zinc and silver with 78.7 %, 73.1 % and 63.8 % whereas only 39.0 % of iron evaporate on average. Figure 18 shows the influence of the application of various SCAs. AlCl_3 chlorinates indium and silver most efficiently while CaCl_2 and MgCl_2 present highest chlorination potentials for lead and zinc respectively. The choice of SCA has the biggest influence on iron extraction, which reaches its maximum by addition of FeCl_3 . However, high iron extraction rates with iron chloride result from evaporated shares of the SCA which can not be distinguished from actually extracted iron from the metal compound in this simulation. The form in which the metal is present during the chlorination process drastically determines iron vaporization, as shown in Figure 19. When applied as iron oxide, extraction is twice as high as the mean rate. Indium and zinc are best extracted from their hydrides, silver from its sulfate compound. Lead extraction does not show any significant dependency on its present form, neither is it affected by any kind of secondary compound, as Figure 20 indicates. K_2SO_4 lowers extraction of all other assessed metals between -29.5 % in the case of silver to -83.7 % for iron. Pyrite FeS_2 improves indium, zinc and iron extraction by 27.0, 16.9 and 63.0 % respectively but inhibits silver vaporization by -17.8 %. SiO_2 and CaF_2 benefit the extraction of all assessed metals, whereas increases caused by the first are generally more pronounced. Finally, also the atmosphere substantially determines extraction efficiencies of all metals except for lead. The presence of water reduces extraction rates of all metals, while on the contrary SO_2 has a generally positive influence. Oxygen remarkably lowers zinc and indium vaporization by -20.2 % and -15.5 % respectively. On the other hand, silver extraction is enhanced by 17.4 % under oxidative conditions.

So far, metals have only been assessed individually to examine different chlorination behaviours among them. Yet, no practically relevant conclusions regarding extraction potentials of present mixtures can be drawn from previously presented results. To obtain insights about theoretical chlorination behaviours of a simulated iron precipitation residue, further calculative modelling is necessary.

3.2.2 Assessment of metal mixtures

First, the input algorithm must be altered to enable the creation of reactant tables for mixtures. As in practice, the usage of mass as the unit for quantity is more common than of moles, input values are set accordingly. To facilitate the simulation of real residues, the input of total mass alongside the concentrations of to be assessed metals are sufficient as input parameters. In accordance to the set form of present metal compounds (oxidic, sulfatic, etc.), the algorithm distributes the metal input mass and calculates their individual input quantities based on chemical formular and molar mass. The stoichiometric calculations must now result in the total chlorine amount needed to chlorinate all metals at the same time, which is why an additional function is implemented for this purpose.

If not stated otherwise, 100 g of a mock jarosite mixture simulated by the implementation of previously found mean metal concentrations as shown in Table 4 is applied for further simulations. Since only indium, silver, zinc, lead and iron are assessed, the actual input quantity depends on the chosen form in which the metals are present. Therefore, input mass does not necessarily add up to 100 g but only represent the correct metal quantities. This procedure allows an easy integration of the results of chemical analysis of real residue samples. The so obtained virtual material will be referred to as “mock jarosite” in further evaluations. However, a distinct difference between mock and real jarosite must be emphasized in this context. The simulated material must not be mistaken with the chemical jarosite structure as described in Chapter 1. Instead of being bound in a basic iron sulfate, all subsequently assessed metals are present in their pure oxidic form, which corresponds to a thermally decomposed jarosite material.

Table 4: Metal concentrations used for simulating the mock jarosite mixture

	In	Ag	Zn	Pb	Fe
Concentration [wt.%]	0.0239	0.0239	4.11	4.38	29.0

- Influence of temperature on metal extraction from mock jarosite

First, a comparison of vaporization behaviours in mixtures to simulate the individual metal assessment is intended. Therefore, a simulation run examining the influence of temperature on metal extraction rates from mock jarosite shown in bold lines of Figure 22 which was carried out under identical conditions as the one in Chapter 3.2.1 (Figure 11), represented by the partly transparent lines.

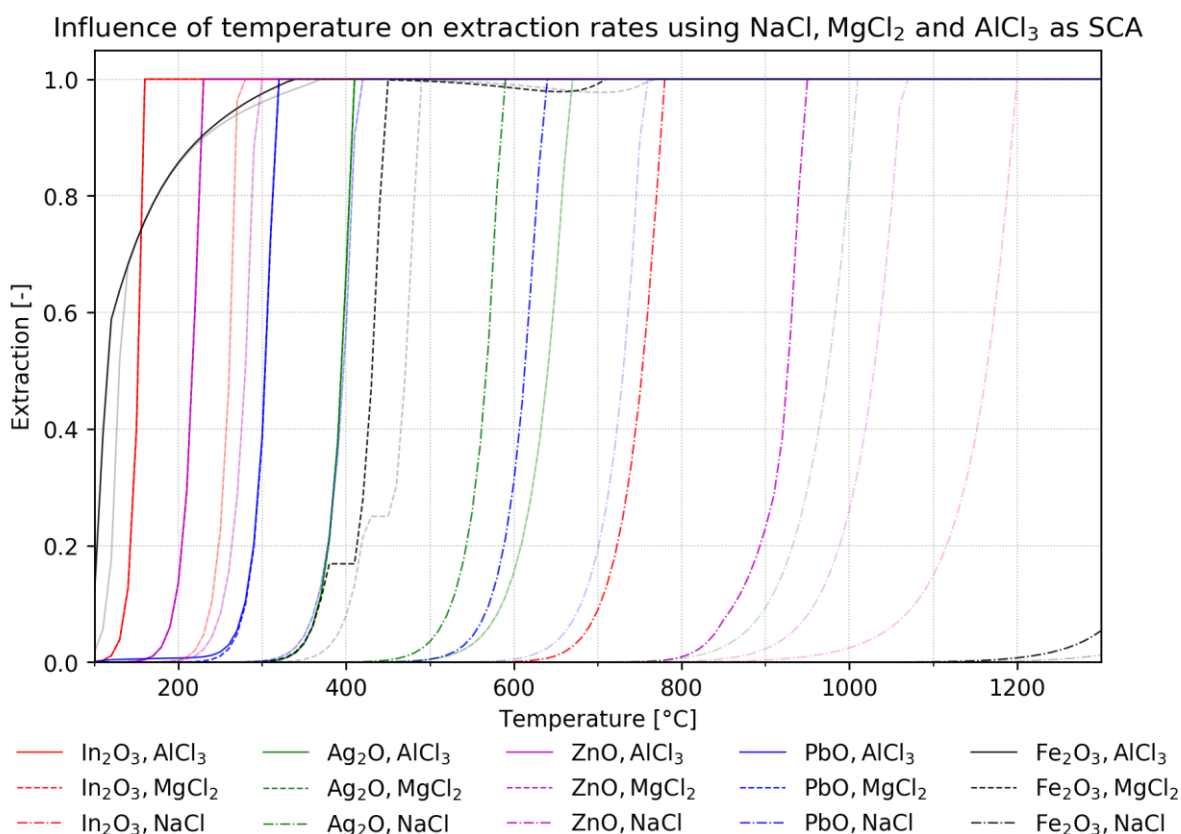


Figure 22: Comparison of extraction rates of individually assessed metals (transparent lines) and from mixtures (bold lines) as a function of temperature

At first glance the results for extractions from mock jarosite appear to be highly similar to the ones for individually assessed metals, yet, some noteworthy alterations occur. Firstly, significant evaporation generally begins at lower temperatures. Indium (red lines) reaches full extraction at already 160 °C, zinc (magenta lines) at 230 °C and lead (blue lines) at 320 °C when applying MgCl₂ or AlCl₃ (solid or dashed lines, overlapping for named metals) as SCA. By the use of MgCl₂, contrary to individual chlorination, silver is fully evaporated from the mixture subsequently at 410 °C, while only 17 % of iron is evaporated. This phenomenon is enabled by the formation of (MgO)(Fe₂O₃) which binds iron in the solid phase as discussed in previous chapters. Iron oxide reaches full extraction at only 450 °C. The order of largest chlorine potentials of NaCl is also altered to Ag>Pb>In>Zn>Fe which fully evaporate at 590, 640, 780 and 950 °C respectively, while iron does not reach extraction rates above 6 % in the assessed temperature range.

Chlorination potentials of KCl, CaCl₂ or FeCl₃ are similar to the already assessed ones of same valency, as can be seen in Figure 56 in the Appendix. However, a few but consequential differences must be noted which occur when applying CaCl₂ as SCA. The order of full extraction is found to be Pb>Ag>In>Zn>Fe as chlorination potentials appear to be lower for indium and zinc than with MgCl₂. Nonetheless, instead of already beginning to evaporate

simultaneously with silver in the case of MgCl_2 , iron does not show significant extraction rates at temperatures below 700 °C. With increasing temperatures, iron extraction rate increases until reaching an only slightly rising plateau of around 40 %. Since this behaviour presents great potential for a selective extraction of assessed metals, it is analysed in more detail.

- Influence of calcium on metal extraction from mock jarosite

For this purpose, another calculation run was carried out considering chlorination scenarios of mock jarosite with CaCl_2 under various atmospherical conditions. The results are shown in Figure 23 below.

Influence of temperature and atmosphere on extraction rates from mock jarosite with CaCl_2

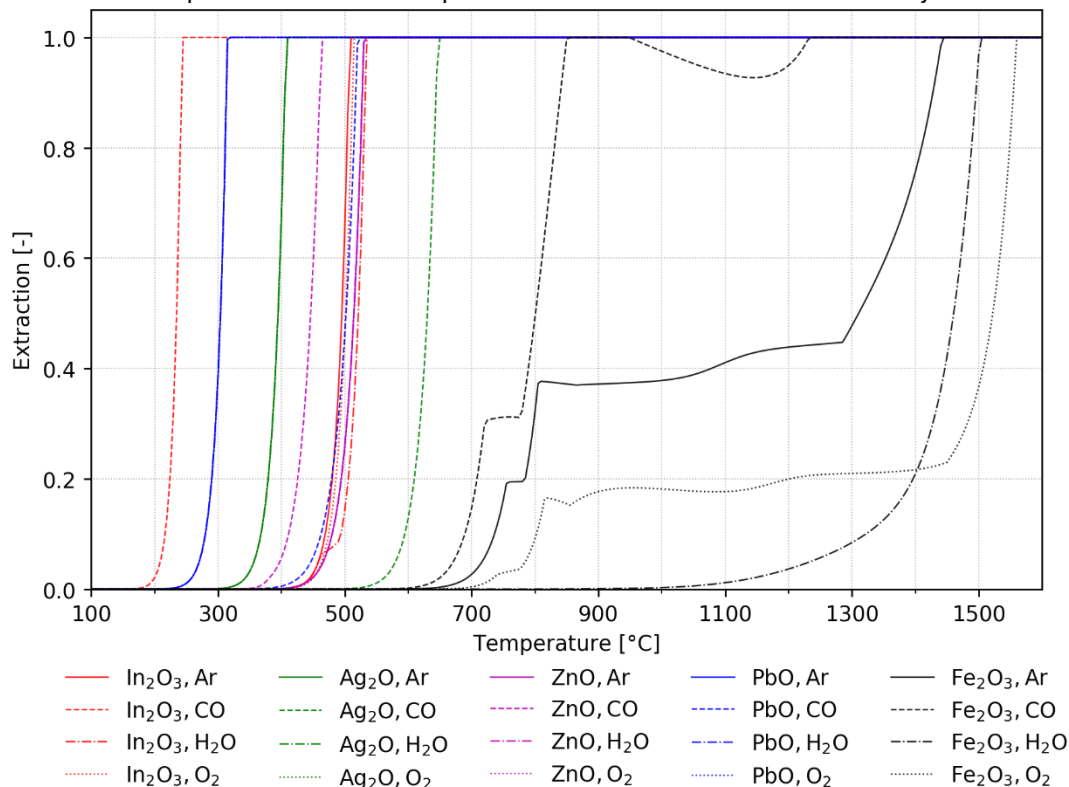


Figure 23: Influence of temperature and atmospherical conditions on extraction rates of indium, silver, zinc, lead and iron from mock jarosite using CaCl_2 as SCA

While the desired metals indium (red lines), lead (blue lines), silver (green lines) and zinc (magenta lines) reach full extraction at temperatures below 650 °C regardless of atmospheric conditions, iron (black lines) behaves rather differently in regard to vaporization progression and sensitivity to different atmospheres. In a CO-atmosphere extraction is most favoured, leading to a full extraction at a temperature of 850 °C. However, the rate begins to decrease at 945 °C until a local minimum of 92.7 % at 1175 °C before recommencing to increase to complete extraction at 1235 °C. The least iron extraction occurs in humid atmosphere, in which first significant rates of higher than 1 % evolve above 1090 °C. At a previously defined

maximum retort temperature of 1200 °C, only 3.7 % of present iron evaporates. In presence of water, full iron extraction occurs at 1505 °C. Subsequently, an in-depth compound analysis is conducted to acquire knowledge about these mitigation effects. For this purpose, only compounds which contain either iron (solid and dashed lines) or the SCA and compounds thereof (dash dotted and dotted lines) are plotted. Since the humid atmosphere demonstrates the most significant reducing capacity, it is assessed more profoundly in Figure 24, while the plots for other atmospheric conditions can be found in the Appendix.

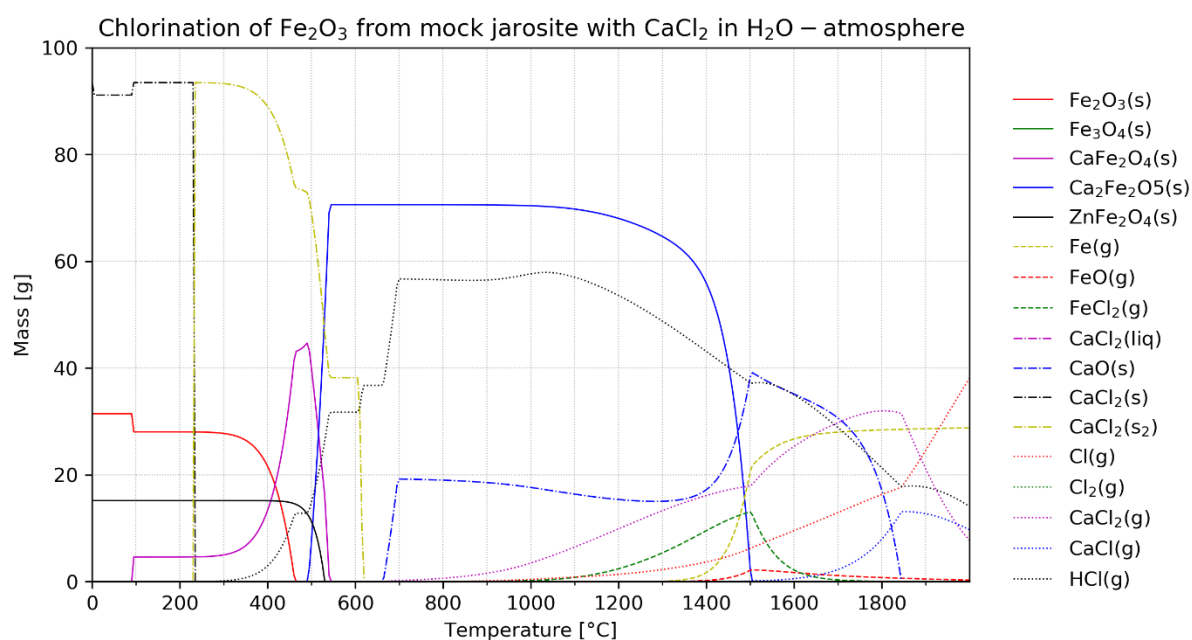


Figure 24: Formation of various solid (solid lines) and gaseous (dashed lines) iron compounds as well as solid (dash dotted) and gaseous (dotted) compounds of CaCl_2 during chlorination of mock jarosite as a function of temperature

Results show that during chlorination of mock jarosite with CaCl_2 , iron is bound in a solid CaFe_2O_4 or $\text{Ca}_2\text{Fe}_2\text{O}_5$ compound, thus is not chlorinated and evaporated but remains in the solid phase in relevant temperature ranges. Only in the presence of CO significant amounts of FeCl_2 (green dashed line) evolve at temperatures higher than 650 °C. In case of exposure to water, input Fe_2O_3 (red line) quickly reacts with the SCA to form CaFe_2O_4 (solid magenta line) which transitions to a higher calcium-carrying compound $\text{Ca}_2\text{Fe}_2\text{O}_5$ at 500 °C, resulting in a more rapidly decreasing amount of solid CaCl_2 (yellow dash dotted line). The solid iron compound decomposes slowly under formation of gaseous FeCl_2 at temperatures higher than 1000 °C. Exceeding 1400 °C, gaseous Fe (yellow dashed line) becomes the predominant iron gas phase as FeCl_2 amounts decline.

Since the inhibition of iron extraction is mainly due to its binding in a calcium compound, its vaporization behaviours may presumably also be reduced by the addition of calcium carrying secondary compounds. To assess such an application's potential, chlorination scenarios of mock jarosite with MgCl_2 , AlCl_3 and FeCl_3 in presence of $\text{Ca}(\text{OH})_2$, CaCO_3 , CaF_2 and CaSO_4

will be carried out. Before, several adaptations of the simulation's approach are altered to guarantee a more practical and realistic observation.

- Reducing complexity through the integration of a joint extraction factor

Since the main pursuit of jarosite chlorination is the separation of valuable metals from the predominant iron phase, a combinational representation of their behaviour is senseful and favours comprehensibility. Therefore, extraction rates of valuable metals are reduced into one single value "Valuables Extraction" (Valex). Furthermore, the stoichiometric chlorine amount to chlorinate iron contained in the mock jarosite is subtracted from the total chlorine demand. To approach the comprehension of valuable's extraction rates, their current market price given in Table 2 above is taken for weighting individual metals. The Valex is then calculated according to Equation 20, where E_{met} is the metal's extraction rate and P_{met} its current market price. The Valex can be interpreted as the ratio of financial output achieved by the extraction of value embodied by contained valuable metals in the mock jarosite material, ranging from zero to one.

$$\text{Valex} = \frac{\sum_{\text{met}} E_{\text{met}} \cdot P_{\text{met}}}{\sum_{\text{met}} P_{\text{met}}} \quad (20)$$

Repeating the previously conducted calculation run on temperature dependency with the aforementioned adjustments, results are more easily interpretable in terms of practical application potential of assessed scenarios, as visualized in Figure 25. MgCl_2 , AlCl_3 and FeCl_3 (green dotted/double dotted/triple dotted line, overlapping) are all equally suitable for selective valuable metal extraction from mock jarosite. Thereby, full valuable extraction occurs at 410 °C while for CaCl_2 (green dash dotted line), NaCl (green dashed line) and KCl (green solid line) higher temperatures of 510, 830 and 860 °C respectively are required. On the other hand, iron extraction starts at 800 °C, increasing to 12.5 % at 1200 °C when applying the for Valex preferable SCAs (green dotted/double dotted/triple dotted line, mostly overlapping), whereas monovalent SCAs (solid and dashed lines) lead to no significant iron vaporization up to this temperature. However, as high Valex values are possible at considerably lower temperatures, only MgCl_2 , AlCl_3 and FeCl_3 will be evaluated for further simulations.

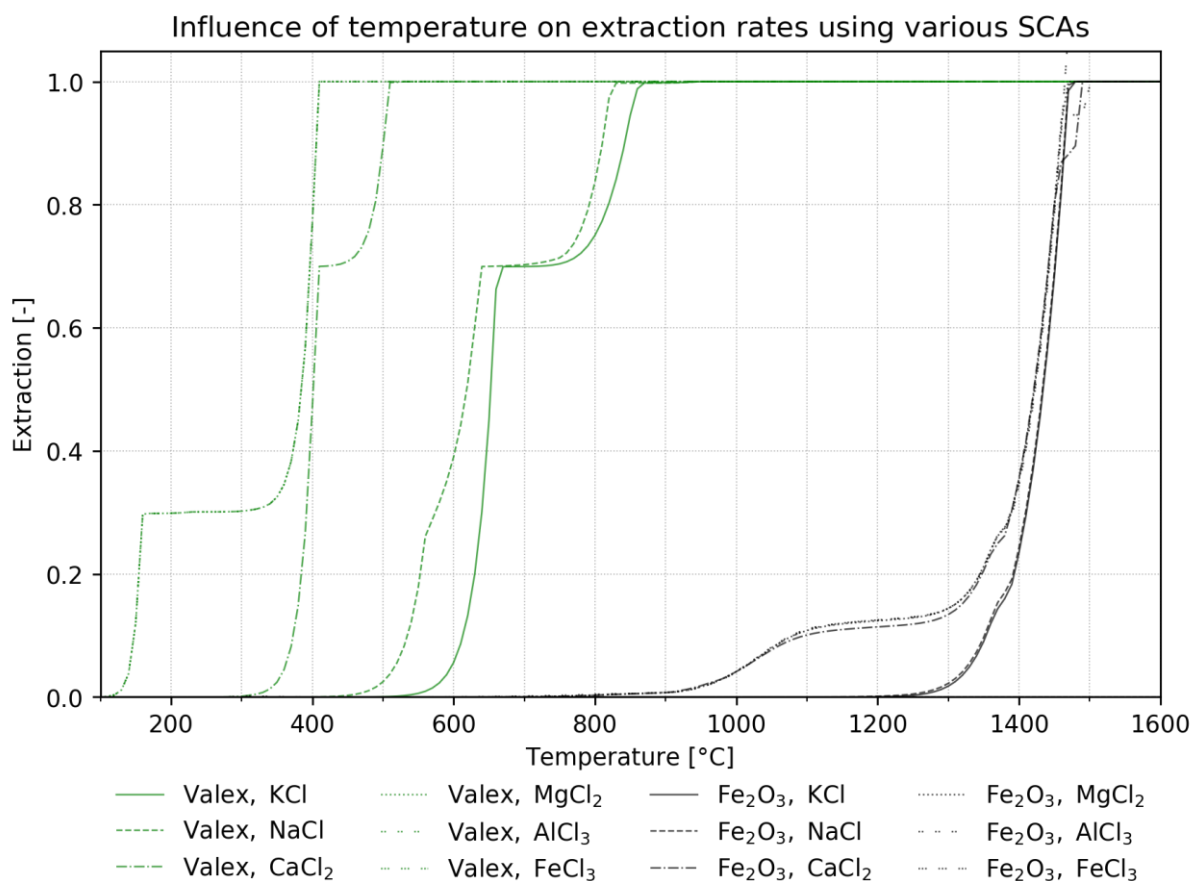


Figure 25: Influence of temperature on Valex and iron extraction from mock jarosite mixture using NaCl, KCl, MgCl₂ (mostly overlapping), CaCl₂, AlCl₃ or FeCl₃ (mostly overlapping) as SCA, pressure of 1 atm, stoichiometry of 1 and inert atmosphere

- Qualitative assessment of further influences

For the evaluation of further qualitative influences on both Valex and iron extraction, similar scenarios are chosen as for the individual assessment in Chapter 4. The quantity of secondary compounds is chosen to be the remaining share of mass next to metallic compounds in mock jarosite to complete 100 g. Atmospheres are modelled by adding 50 g of respective gas as a reactant.

Figure 26 gives an overview of extraction rates for all assessed influential categories. Values for each category represent the calculated mean including all other influences of other categories respectively, which is why interconnections between certain pairs or triplets of influences are not visible and maximum or minimum values can differ between plots. For example, results for the influence of the applied SCA shown in the left column represent mean values for all investigated secondary compounds and atmospheres. Generally, extraction rates increase with temperature in all cases. Valex (upper plots) reaches its maximum in almost all scenarios at 1000 °C and in some at already 800 °C. The choice of SCA does not influence extraction significantly. In the case of secondary compounds, K₂SO₄ and Ca(OH)₂ generally

lower Valex while SiO_2 and CaSO_4 brings improvements. Reductive atmospheres of CO decrease Valex at 400 and 600 °C while increasing it at 800 °C. The presence of water behaves similarly but less pronounced. Iron extraction is comparably low at moderate temperatures, reaching a maximum mean extraction of 8 % at 1200 °C. AlCl_3 causes more extraction in respect to other assessed SCAs. The presence of CaF_2 and FeS_2 favour iron evaporation significantly, reaching maximum values of 0.26 in the case of CaF_2 and 1200 °C. Humid conditions always reduce iron extraction to a minimum, resulting in only 1 % even at the highest observed temperature. On the other hand, CO drastically enhances iron extraction. The difference between Valex and the 5-fold iron extraction displays a generally parabolic shape, as high temperatures favour more iron extraction, lowering the desired pure valuable metal output.

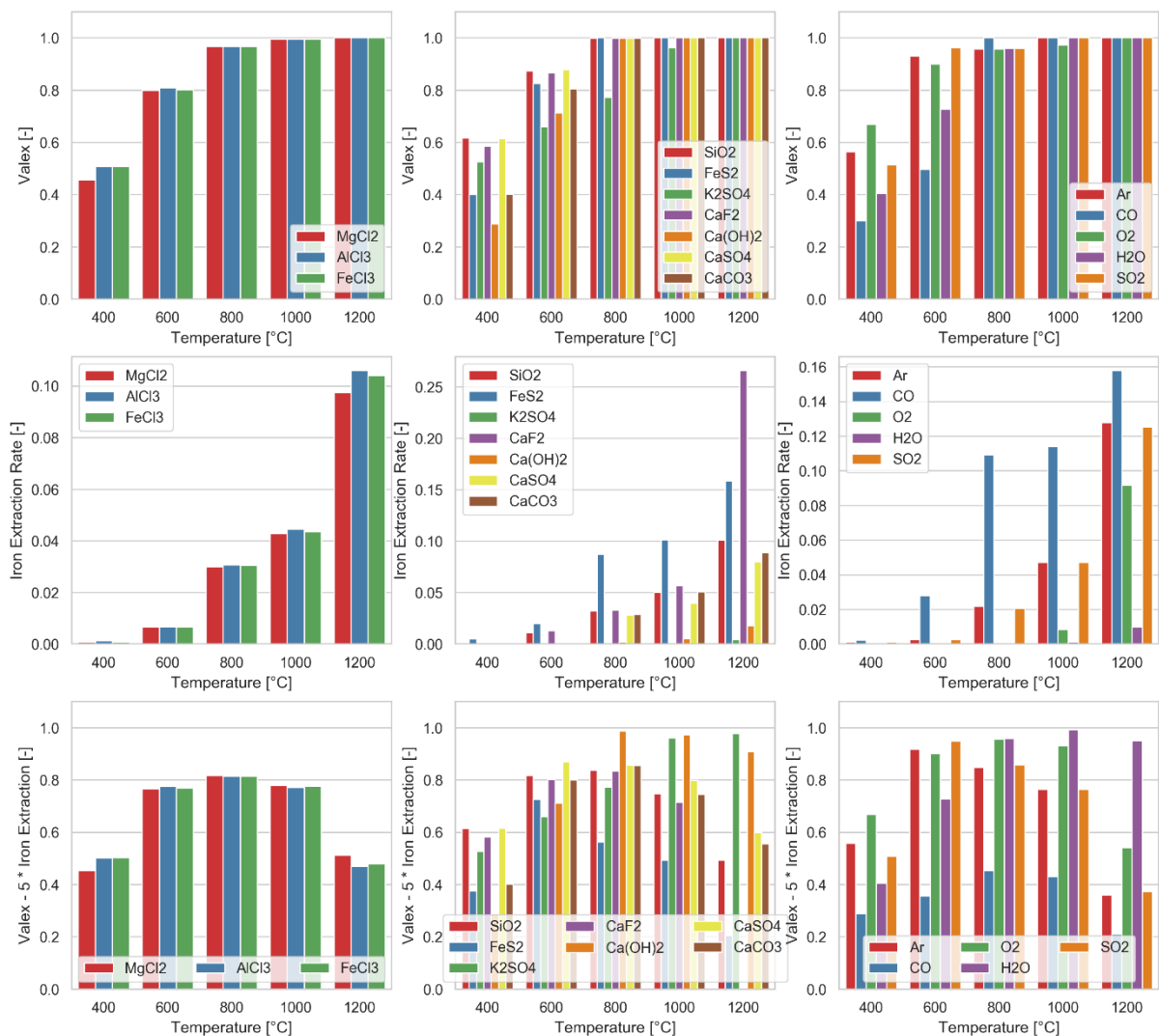


Figure 26: Influence of various SCAs (left), secondary compounds (middle) and atmospheres (right) on extraction rates of Valex (upper) and iron (middle) and the difference between both (lower), where iron extraction is weighted 5-fold, pressure of 1 atm and stoichiometry of 1

To visualize the percentual deviation from mean extraction of each influence in dependence of the atmosphere, further deviation plots are created in accordance with previously described approach. Two of these are shown exemplary in Figure 27 and Figure 28 below. Results underline previous findings, CaF_2 drastically improves iron extraction in combination with all atmospheres, peaking with O_2 at $1200\text{ }^\circ\text{C}$ while CO causes the largest decrease of Valex, climaxing in combination with K_2SO_4 at $600\text{ }^\circ\text{C}$.

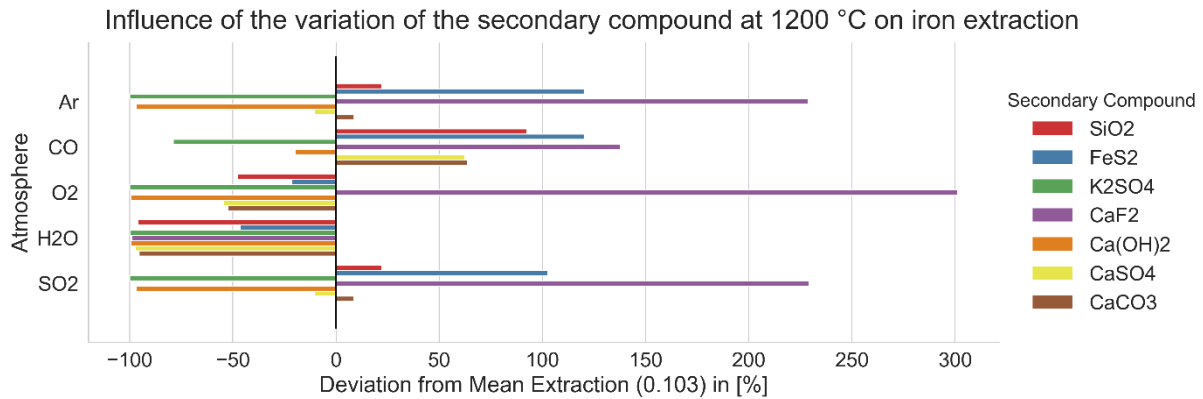


Figure 27: Influence of the variation of atmosphere and secondary compounds on iron extraction rates at $1200\text{ }^\circ\text{C}$, 1 atm and stoichiometry of 1

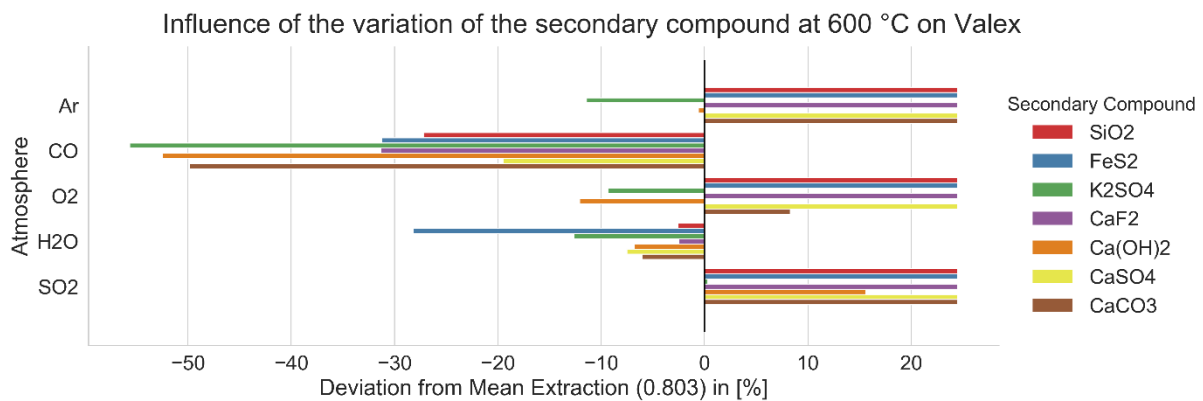


Figure 28: Influence of the variation of atmosphere and secondary compounds on Valex rates at $600\text{ }^\circ\text{C}$, 1 atm and stoichiometry of 1

The heatmap of assessed influences on Valex rates presented in Figure 29 highlights the best and worst case scenarios for valuables recovery from mock jarosite while showing general tendencies of individual effects. Valex peaks in an oxidative atmosphere in presence of FeS_2 and reaches its minimum in presence of Ca(OH)_2 in inert or humid atmospheres. O_2 consistently improves Valex whereas a reductive atmosphere containing CO results in low rates. For iron extraction, maximum and minimum influences are considerably more distinct as in the case for Valex, as shown in Figure 60 in the Appendix. The presence of FeS_2 increases iron evaporation almost ten-fold in CO -, SO_2 - and Ar -atmosphere, leaving interpretation of other influences difficult.

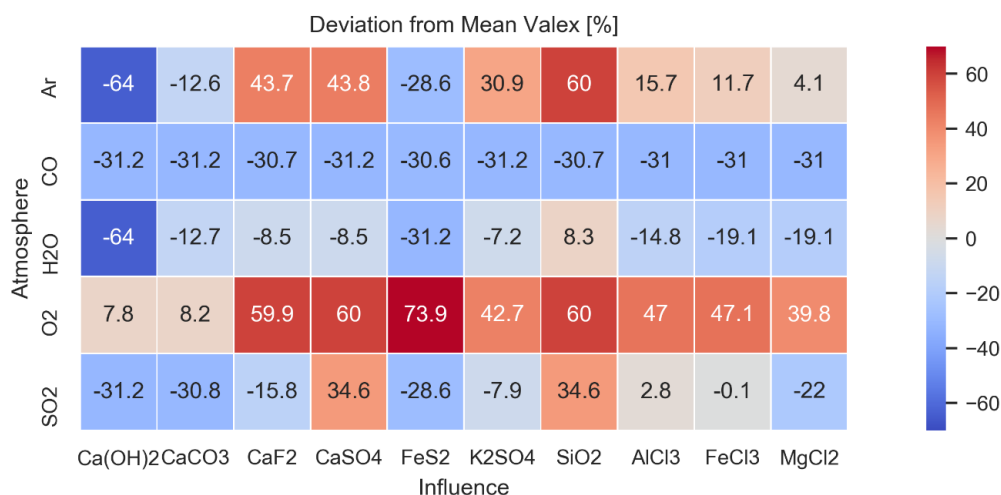


Figure 29: Deviation from mean Valex for various atmospheres in combination with different secondary compounds and SCAs for full temperature range, 1 atm and stoichiometry of 1

As for practical reasons a combined evaluation of both Valex and iron extraction is necessary to determine ideal process scenarios, their difference is plotted in Figure 30. As before, iron extraction is weighted 5-fold in order to better visualize its impact. The least preferable scenarios (deep blue) include CO as atmosphere and the presence of CaF_2 or FeS_2 . Best results (deep red) are obtained in O_2 -atmosphere and FeS_2 or CaSO_4 as secondary compound. However, information about the temperatures is compromised by the formation of mean values to achieve this simple illustration. Therefore, given findings may be less or more valid at individual temperatures.

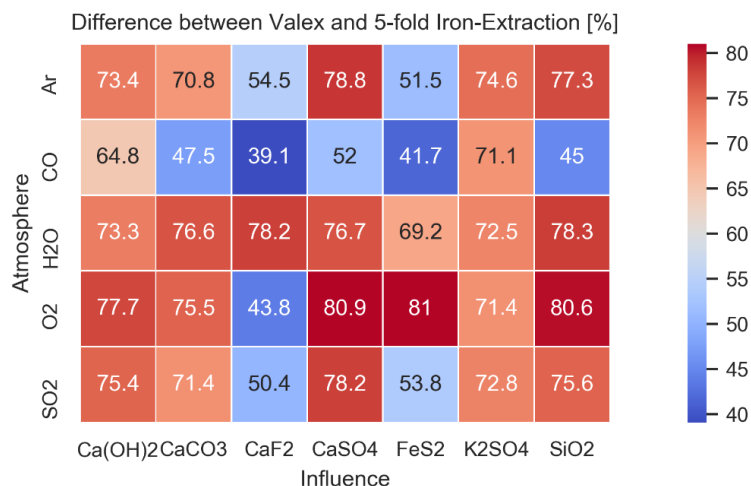


Figure 30: Difference between Valex and 5-fold iron extraction for various atmospheres in combination with different secondary compounds, mean of all assessed temperatures, pressure of 1 atm and stoichiometry of 1

All previously assessed SCAs were assumed to be anhydrous. However, due to their hygroscopic nature, MgCl_2 , AlCl_3 and FeCl_3 are generally applied as hydrates. To examine the influence of the SCA-form, the hexahydrates $\text{MgCl}_2 \cdot 6\text{H}_2\text{O}$, $\text{AlCl}_3 \cdot 6\text{H}_2\text{O}$ and $\text{FeCl}_3 \cdot 6\text{H}_2\text{O}$ are

assessed in comparison to their anhydrous form. Since the differences between the hydrated and anhydrous form affects all assessed SCAs in a similar way, as Figure 61 in the Appendix shows, the influence of hydration is categorized. Figure 31 displays the difference between Valex and the fivefold iron extraction in combination with different secondary compounds and atmospheres in dependence on the SCA's form. Generally, better extraction results are obtained by application of hydrated SCAs, showing the biggest improvements in CO-atmosphere and presence of FeS_2 or CaF_2 . This behaviour might be mainly explained by the previously examined mitigation effect water has on iron extraction.

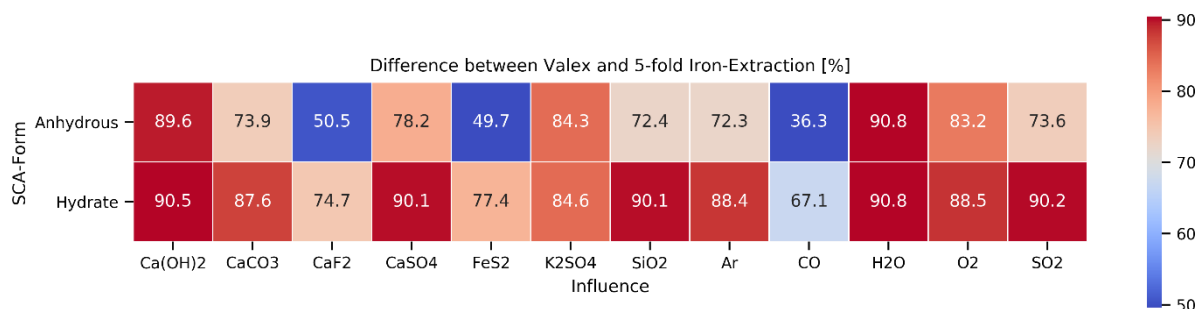


Figure 31: Difference between Valex and 5-fold iron extraction for various atmospheres in combination with different secondary compounds, anhydrous and hydrated SCAs, mean values for temperatures, pressure of 1 atm and stoichiometry of 1

To include temperature and stoichiometry into a joint Valex-iron-visualization, a bubble chart is plotted with relevant values as shown in Figure 32 below. Generally, an increase of stoichiometry positively affects Valex only at temperatures lower than 800 °C while it favours iron extraction at all assessed temperatures. The positive correlation between temperature and extraction holds true for both Valex and iron. Therefore, a moderately high temperature at which Valex reaches sufficient levels and low stoichiometry appear as best suitable for selective extraction. At 800 °C Valex reaches values above 96.6 % regardless of stoichiometry. At the same temperature, iron extraction ranges from 0.7 % at 0.25 mol Cl/mol Cl-Demand to 3.0 % at 1.00. At 1000 °C and a stoichiometry of 0.25, 99.4 % of value is extracted alongside 1.0 % of iron. This chart can further be adjusted to each desired scenario. Figure 62 and Figure 63 in the Appendix show the least preferable scenario in CO-atmosphere and presence of CaF_2 and the most favourable one in O_2 -atmosphere and CaSO_4 as secondary compound, respectively.

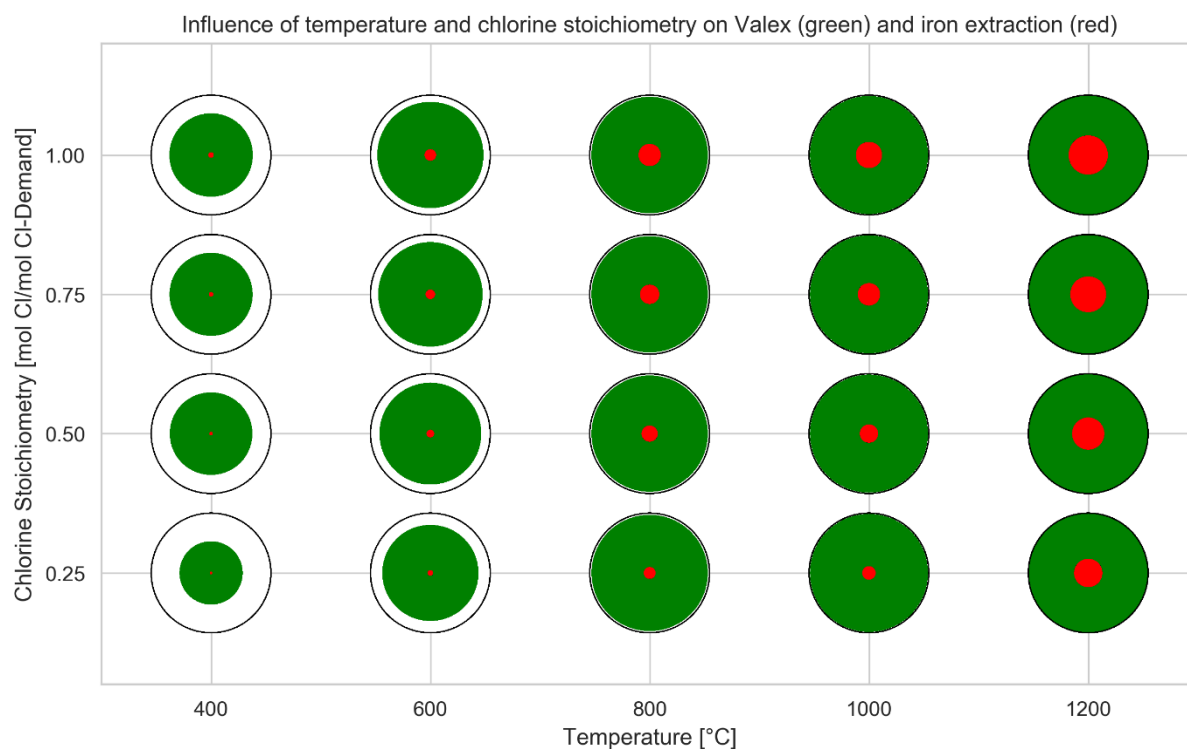


Figure 32: Influence of temperature and chlorine stoichiometry on mean Valex (green) and iron extraction (red) including all previously stated parameters, the black circle represents a value of 1.00

To conclude the assessment of qualitative influences on extraction rates, the selective chlorination of valuable metals from a mock jarosite material is generally possible on a thermochemical basis. However, it displays a complex system of various interconnected parameters, which can influence the feasibility either positively or negatively. Moreover, only a small number of almost infinite parameters were selected in the course of this work. More comprehensive simulations are easily performed by an individual selection of other or further valuable metals, SCAs, atmospheres or secondary compounds.

Regardless of the expansion of chosen reaction parameters, a theoretical simulation is restricted to fundamental thermodynamic and chemical laws. Thus, they fall short of explaining the complex mechanisms of real processes. Therefore, a set of experiments is carried out in order to determine kinetic characteristics and reaction mechanisms of real chlorination scenarios.

4 Kinetic study of chlorination reactions

The purpose of this kinetic study is to obtain insights regarding the reaction mechanism of chlorination processes of the assessed metal compounds. In literature, the term reaction mechanism is used to describe either the fit of experimental data to a mathematical model or the chemical steps leading to a transformation of reactants into products. While the first definition can be obtained by mathematical analyses only, the latter must include an evaluation of chemical properties but offers a more logical and comprehensive picture of reaction processes. However, both rely on a set of measurements, within which the extent of reaction (α) can be determined by any quantitatively related dimension (e.g. mass) as a function of both time and temperature. Obtained results deliver information about the extraction rate's dependency on temperature as described by the Arrhenius equation given in Equation 21, where T is the temperature in [K], E_a the energy barrier to be passed for the reaction to occur, namely activation energy in [J/mol], A the frequency of occurrence of product formation, namely frequency factor [-] and R the gas constant ($= 8.314$ [J/K · mol]). Moreover, the rate of change of reaction extent $d\alpha/dt$ can be described by a rate equation as shown in Equation 22, where $f(\alpha)$ is an individual function which describes the amount of reactant, also referred to as the kinetic model. [81]

$$\alpha(T) = A \cdot \exp\left(-\frac{E_a}{R \cdot T}\right) \quad (21)$$

$$\frac{d\alpha}{dt} = \alpha(T) \cdot f(\alpha) \quad (22)$$

Traditionally, isothermal experiments were the most commonly employed approach to obtain the Arrhenius parameters (E_a and A), where rates of reactions are measured at a set of predefined temperatures. However, non-isothermal experiments, where usually the reactant's quantity is measured at a set of different heating rates $\beta = dT/dt$, have become increasingly popular in the course of the late 20th century. [81]

4.1 The Kissinger-Method for kinetic parameter assessment

The upswing of isothermal kinetic studies was majorly provoked by the proposal of an easily applicable method for kinetic parameter determination using differential scanning calorimeters (DSC) by Homer E. Kissinger in 1957. Kissinger combined the Arrhenius equation with the rate equation for solid state reactions and differentiated it by parts to obtain a general rate equation according to Equation 23. [82, 83]

$$\frac{d\left(\frac{d\alpha}{dt}\right)}{dt} = A \cdot \exp\left(\frac{-E_a}{R \cdot T}\right) \cdot \frac{d[f(\alpha)]}{dt} + A \cdot f(\alpha) \cdot \frac{d\left[\exp\left(\frac{-E_a}{R \cdot T}\right)\right]}{dt} \quad (23)$$

Through the integration of the heating rate β in the second term and specifying T as the maximum temperature of an exothermic peak $T = T_{\max}$, where the change of the rate of reaction $\frac{d(d\alpha/dt)}{dt} = 0$, and substituting $\frac{d[f(\alpha)]}{dt}$ for $f'(\alpha) \cdot \frac{d\alpha}{dt}$ the equation simplifies to Equation 24 which can be solved for $\frac{\beta}{T_{\max}^2}$ to obtain Equation 25.

$$0 = A \cdot \exp\left(\frac{-E_a}{R \cdot T_{\max}}\right) \cdot f'(\alpha) + \frac{E_a \cdot \beta}{R \cdot T_{\max}^2} \quad (24)$$

$$\ln\left(\frac{\beta}{T_{\max}^2}\right) = \ln\left(\frac{A \cdot R}{E_a}\right) + \ln[-f'(\alpha)] - \frac{E_a}{R \cdot T_{\max}} \quad (25)$$

After a final assumption, that reaction order $n=1$, $f'(\alpha)$ becomes -1 and simplifies Equation 25 to obtain the final Kissinger equation, as shown in Equation 26:

$$\ln\left(\frac{\beta}{T_{\max}^2}\right) = \ln\left(\frac{A \cdot R}{E_a}\right) - \frac{E_a}{R \cdot T_{\max}} \quad (26)$$

Based on this equation, a series of small scale experiments, where the to be observed material is heated up at different heating rates (β) is sufficient for Arrhenius parameters determination. Therefore, the exothermic peak temperatures (T_{\max}) of respective trials are plotted as $\ln\left(\frac{\beta}{T_{\max}^2}\right)$ versus $\frac{1}{T_{\max}}$, whereas the slope of the obtained line represents $-\frac{E_a}{R}$ and the intercept $\ln\left(\frac{A \cdot R}{E_a}\right)$. From these values, the activation energy E_a and frequency factor A can easily be calculated. After its first publication on November 1st, 1957, the original article proposing this method has been viewed over 18,000 times on the publishers website and has been cited in more than 9,000 research papers on a great variety of scientific fields. Aside applications in various disciplines of material sciences it also has already been employed to determine characteristics of metal extraction reactions. [84]

Cui et al. [61] examined a selective chlorinating roasting of nickel, copper and cobalt, Liu et al. [85] assessed the roasting of spent lithium-ion battery cathode materials for lithium recovery and Yang et al. [86] conducted a kinetic study of a borax roasting process to recover rare earth elements from slags.

4.2 Approach and methodology

In this work, four experimental series of chlorination reactions between previously assessed metal compounds and SCAs, as shown in Table 5, are carried out. Isothermal measurements of mass loss and thermocurrent are performed in a Netzsch STA 409 PC differential scanning calorimeter. With regards to previously stated literature [61, 85, 86], four different heating rates of 5, 10, 15 and 20 K/min are selected for each individual campaign. For the preparation of mixtures, a chlorine stoichiometry of 1.5 is chosen to guarantee sufficient chlorine availability. All compounds are used in the form of powders. To increase homogeneity, the SCAs are ground up manually using a ceramic mortar before the preparation of the mixtures. For the calculation of individual masses required to obtain a stoichiometric mixture of given metal compound-SCA pairs an algorithm is developed in Python 3. The definition of the chemical formulas of to be mixed compounds, the desired stoichiometric factor (1.5) and the quantity of the firstly weighed substance directly delivers the necessary mass of the respective second substance. This algorithm replaces manual stoichiometric calculations, which are generally more prone to error. Subsequently, around 100 mg of the obtained mixture is transferred into 0.3 ml Netzsch alumina crucibles (NGB810411) for non-isothermal measurements. A gas flow of 0.3 l/min of synthetic air (80 % N₂ and 20 % O₂) is used for all trials. Additionally, all pure substances are tested for comparison reasons.

Table 5: Assessed metal compounds and SCAs alongside the maximum temperature

	Metal Compound	SCA	Maximum Temperature [°C]
Campaign 1	Ag ₂ O	AlCl ₃ ·6H ₂ O	1400
Campaign 2	In ₂ O ₃	MgCl ₂ ·6H ₂ O	1000
Campaign 3	ZnO	FeCl ₃ ·6H ₂ O	1000
Campaign 4	Fe ₂ O ₃	AlCl ₃ ·6H ₂ O	1400

The scope of this work was not primarily the determination of Arrhenius parameters of given reaction systems according to the Kissinger method but to a greater extent this assessment's automatization by means of an algorithmic analysis of obtained experimental data. This was realized in the Python 3 programming language. At first, the raw data obtained by the DSC measurement is exported as .csv file. In the importation step, the data is modified to be recognized as numeric values by changing the decimal symbol and conversion into a float type. The so obtained DataFrame contains all values of temperature, time, mass and DSC signal of an individual measurement. In the second step, the DSC-signal is parsed for peaks in respect to temperature by integration of the SciPy library [87]. As not all extrema may be relevant for further evaluations, a temperature range as well as the prominence and step width between individual peaks can be set for both exothermic and endothermic peaks separately.

This results in a list of peak temperatures T_{\max} , which is finally integrated into a DataFrame making use of the measurement's heating rate β as index, which is read from the original data file automatically.

All aforementioned steps are converted into a function, which requires only the name of the data file as input. This enables a rapid analysis of the measurements of all four different heating rates of one campaign through a simple for-loop, which results in a matrix that contains the temperatures of all detected peaks (columns) at their respective heating rates (rows). This is used as the basis for the Arrhenius parameter determination via the Kissinger method. At first, $\ln\left(\frac{\beta}{T_{\max}^2}\right)$ is calculated for every peak to obtain a list of respective y-values and $\frac{1}{T_{\max}}$ as x-values. Subsequently, a linear regression is conducted for every peak making use of SciPy's curve fitting function 'linregress'. The frequency factor A and activation energy E_a are then simply calculated from the function's slope and intercept output parameters. The final results are both plotted as DTA-/mass loss vs. temperature-plot and Kissinger-plots, which show the peak's activation energy alongside their R-square values. Yet, it is not clear which chemical reactions are represented by the assessed peaks. Therefore, a progression-analysis is carried out before, which aims to gain further insight into the chlorination process. This analysis is accomplished by another Python algorithm which compares measurements of the chlorination mixture with their respective pure substances. After defining the metal oxide's and SCA's chemical formula and their original quantities weighed in during the mixture preparation, mass shares of potentially remaining compounds are calculated. These are plotted as horizontal lines, named residue-lines, together with the mass-loss and DTA-curve. By matching plateaus of the measured mass signals with calculated residue-lines, conclusions about previous reactions can be drawn.

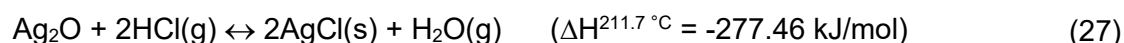
4.3 Results

The presentation of the results happens for each campaign separately for reasons of clarity.

4.3.1 Campaign 1: Ag_2O with $\text{AlCl}_3 \cdot 6\text{H}_2\text{O}$

Figure 33 shows the progression-analysis of the first campaign where Ag_2O is chlorinated by $\text{AlCl}_3 \cdot 6\text{H}_2\text{O}$. Pure silver oxide (green line) does not show changes in mass until its dissociation at an observed temperature of $426.9\text{ }^\circ\text{C}$, where it stays at the pure silver residue-line until the end of measurement. The dissociation is shown as an endothermic peak in the according DTA curve (green dash dotted line). A second endothermic peak is found at $963.9\text{ }^\circ\text{C}$ which has no effect on mass, as it is identified as silver's melting point in literature [67]. The blue line presents the behaviour of pure $\text{AlCl}_3 \cdot 6\text{H}_2\text{O}$. A distinct mass loss of around 80 wt.% occurs between 150–

350 °C, which is represented as endothermic peak at 250.9 °C in the DTA-curve. The mass curve remains practically constant up to 876.2 °C, where it slightly drops to fit the Al₂O₃ residue-line perfectly. This drop, represented by an exothermic peak, might be caused by a phase transition into a γ - Al₂O₃, which was found to occur between 800–900 °C [88]. This suggests, that pure AlCl₃·6H₂O is dried and oxidized to form aluminium oxide in only one observable step. As water is available, the chlorine release is suspected to result in the formation of gaseous HCl. Heating up the chlorination mixture (magenta lines), a more complex mass-curve is obtained. Two endothermic peaks at 144.4 and 235.4 °C mark the temperature of the highest conversion rate of two separate mass-declines, leading to a remaining mass plateau of around 5 wt.% less than the dry AlCl₃ + Ag₂O line. At 455.8 °C an endothermic peak occurs in the mixture's DTA-curve (magenta dash dotted line), which resembles the previously described melting of silver. However, in this case the peak represents the melting of AgCl, whose melting point is found to be between 455–456.9 °C in literature [67, 89]. As a consequence, the chlorination of silver must have already taken place at lower temperatures. Since thermodynamic calculations suggest that the chlorination reaction shown in Equation 27 is exothermic, it could be determined as the negative peak at 211.7 °C, diminishing the highly endothermic peak occurring in the pure AlCl₃·6H₂O DSC-curve.



Further temperature increases do not alter mass balance significantly until reaching temperatures higher than 1000 °C. From there on, liquid silver chloride is suspected to evaporate at an increasing pace up to slightly below 1400 °C, where the mass-curve finally hits the Al₂O₃ residue-line. Furthermore, the DSC-curve shows either two endothermic or one exothermic peak between 764.0–858.3 °C. Since the temperature range is similar to the previously defined phase transition of Al₂O₃, the same explanation seems apparent also in this case.

The variation of the heating rate and the so obtained activation energies of selected peaks are shown in Figure 34. Unfortunately, the low temperature peaks, where the chlorination reaction is suspected to take place, show a variability of prominences to such an extent, that the algorithm cannot spot and distinguish them precisely. Consequently, also the suggested activation energy of 25.24±1.29 kJ/mol for peak 1 is flawed since different peaks are picked for evaluation. The E_a of the melting of AgCl, peak 2, was found to be 1553.8±68.57 kJ/mol, which is questionable because of its great dimension and low R²-value of 0.788. On the contrary, R²-values for peak 4, a probable Al₂O₃ phase transformation, and peak 5, the evaporation of liquid AgCl, reach 0.993 and 0.982, with activation energies of 245.41±1.75 and 126.56±1.44 kJ/mol respectively, which suggest an adequate fit. No comparable values are found in literature, which is why no statement can be made about their correctness.

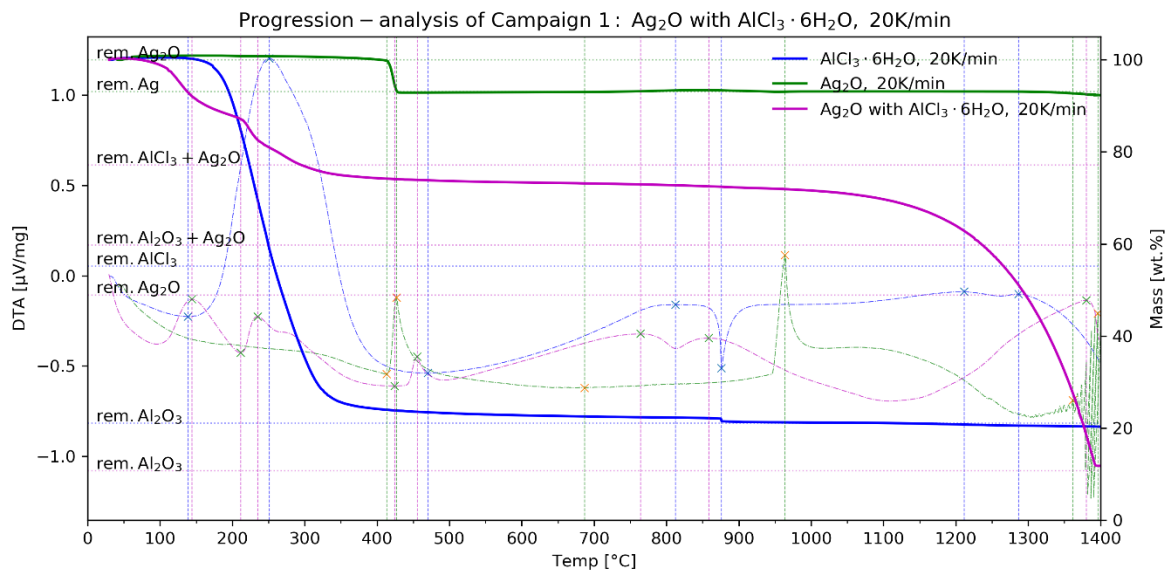


Figure 33: Progression-analysis of the chlorination of Ag_2O with $\text{AlCl}_3 \cdot 6\text{H}_2\text{O}$, mass- and DTA-signals of pure Ag_2O (green lines), pure and $\text{AlCl}_3 \cdot 6\text{H}_2\text{O}$ (blue lines) and the mixture (magenta lines)

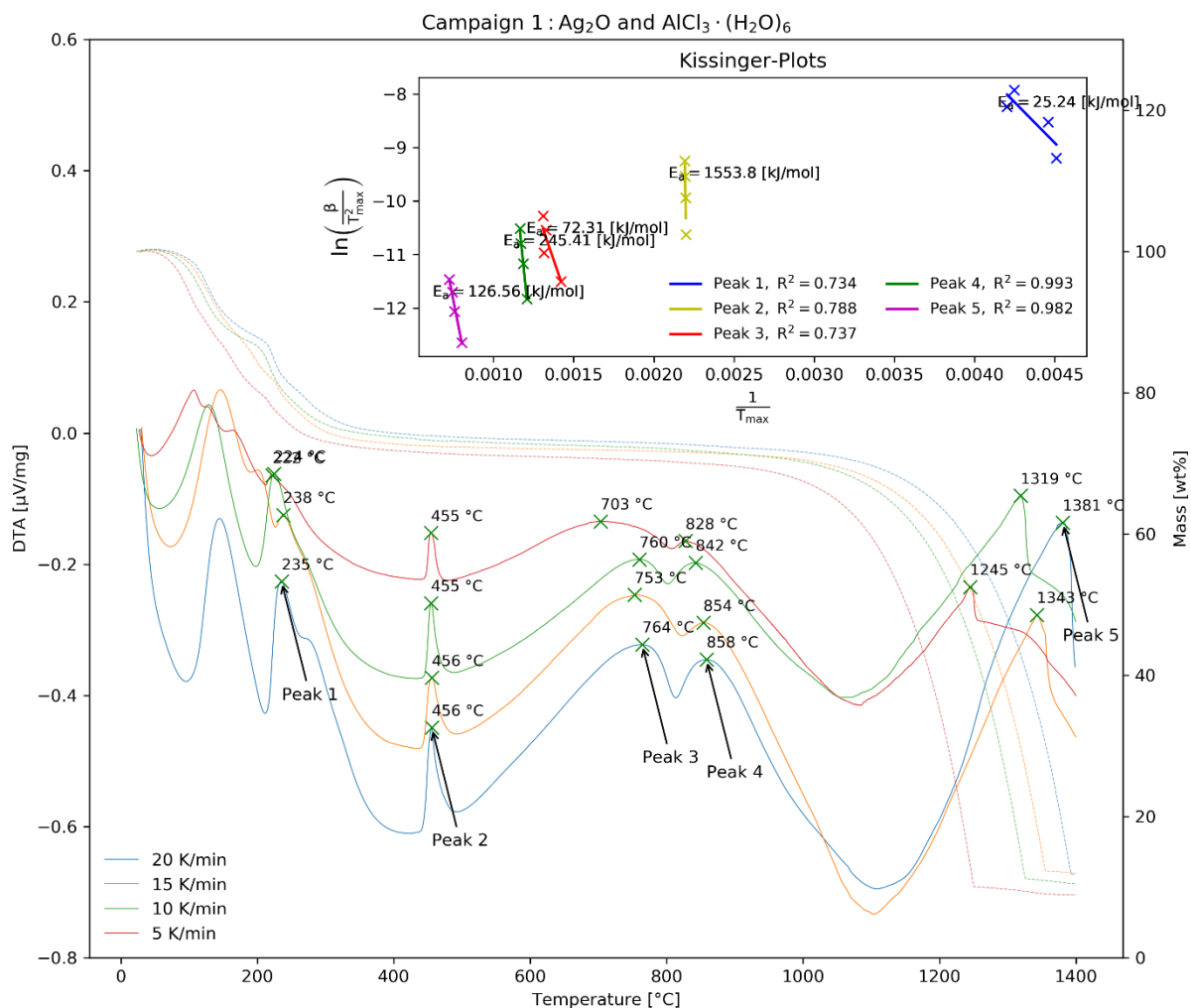
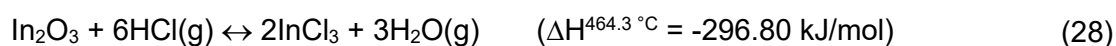


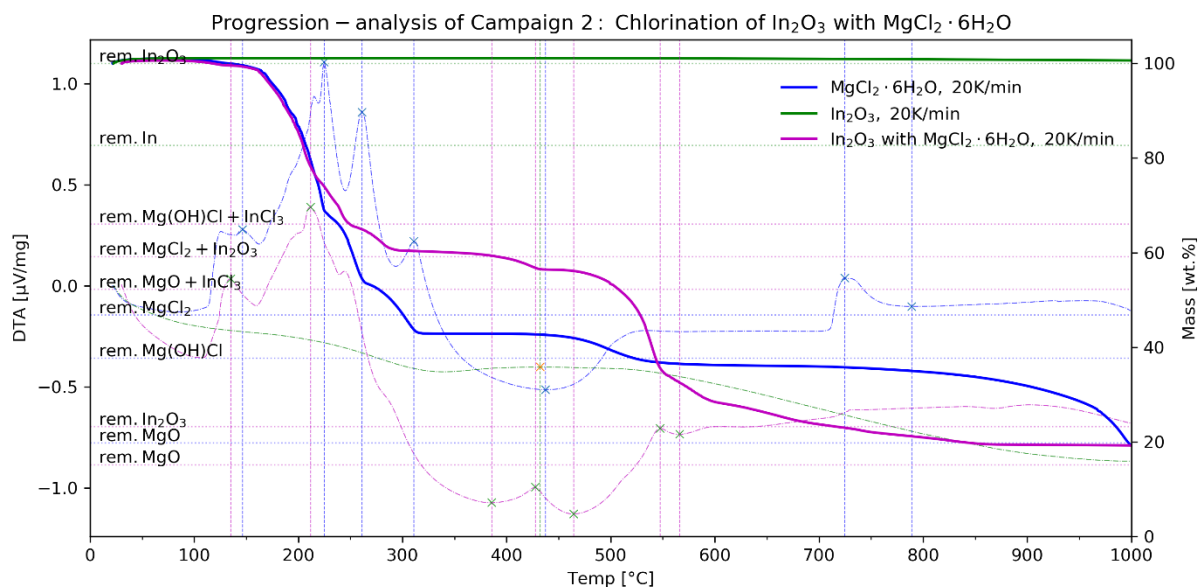
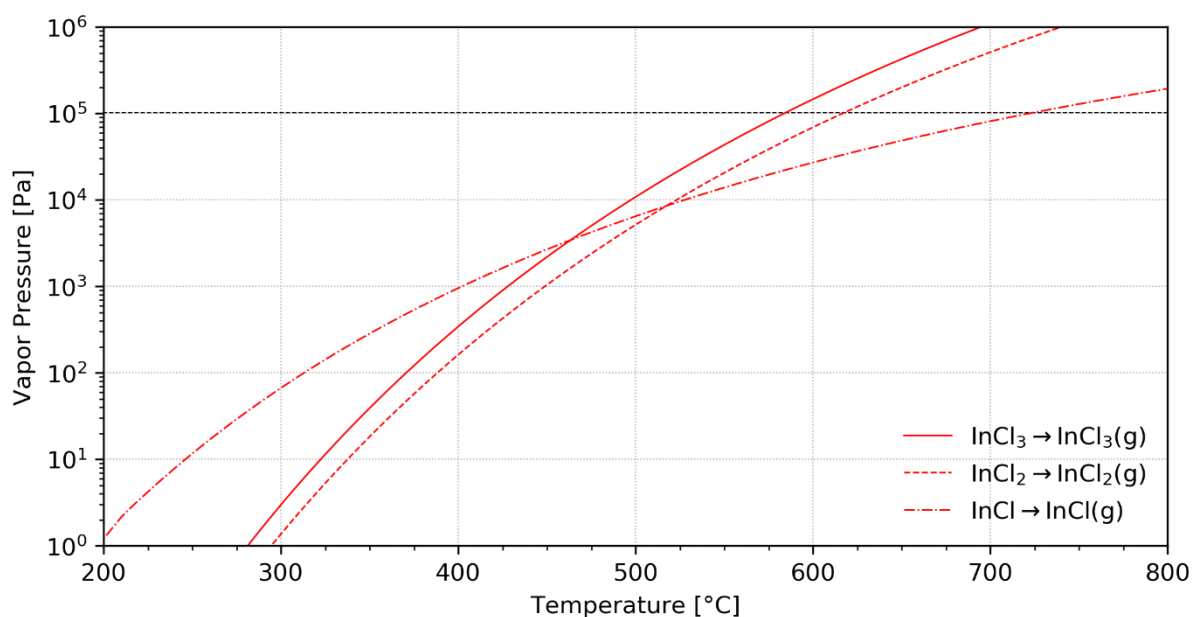
Figure 34: DTA- (solid lines) and mass-curves (dashed lines) for the chlorination of Ag_2O with $\text{AlCl}_3 \cdot 6\text{H}_2\text{O}$ at 5, 10, 15 and 20 K/min, assessed endothermic (green crosses) and exothermic (red crosses) peaks and their Kissinger-plots with calculated activation energy

4.3.2 Campaign 2: In₂O₃ with MgCl₂·6H₂O

Figure 35 gives insight into the progression-analysis of campaign 2 where chlorination of indium oxide with magnesium chloride hexahydrate is assessed. The mass-curve of pure In₂O₃ (green line) remains stable at 100 wt.% and does not show any mass loss. In comparison to the previously analysed aluminium chloride, the SCA MgCl₂·6H₂O (blue lines) shows a complex decomposition behaviour in several stages, which are meticulously described by Huang et al. [90]. The apparent five endothermic peaks in the DTA-curve (blue dash dotted line) which mark the maximum rate of mass-loss of each individual decomposition step refer to the formation of MgCl₂·4H₂O, MgCl₂·2H₂O, MgCl₂·nH₂O (1 ≤ n ≤ 2), Mg(OH)Cl and finally MgO, respectively. The magenta lines represent mass- and DTA-data of the mixture's heating trial, which both show qualitatively identical peaks and mass-losses as the SCA decomposition. However, additional endothermic peaks are observed at 427.7 and 547.6 °C which mark the end of Mg(OH)Cl formation and a major mass decrease of around 20 wt.%, respectively. Moreover, two changes in mass-loss-rate take place after the major decrease at temperatures higher than 550 °C before the mass-curve remains stable at around 5 wt.% above the MgO-residue line. According to the observed behaviours an evaporation of indium in form of chlorides is likely. After dehydration the SCA starts releasing its chlorine at around 300 °C under formation of the Mg(OH)Cl compound, which carries only one mole of chlorine. The endothermic peak at 427.7 °C presents the end and maximum rate of this endothermic decomposition as to be expected in respect to the pure SCA's DTA-curve (blue dash dotted line). The accelerating chlorine availability enables the exothermic indium chlorination as shown in Equation 28, whose maximum rate is believed to be represented as the endothermic peak at 464.3 °C.



However, the formation of other chlorides such as In₂Cl₆, InCl and InOCl is reported in literature, leaving precise conclusions about chlorination reactions difficult without additional analysis [91, 92]. As the sublimation point of InCl₃ is reported to occur in a temperature range of around 400–450 °C, it already evaporates at given temperatures, resulting in the observed mass-loss. When all trichloride is evaporated, as indicated by the endothermic peak at 547.6 °C, chlorides of lower valences evaporate, as suggested by the generally lower and changing rate of mass-loss at higher temperatures. Thermodynamic calculations of the development of vapor pressures of mono-, bi- and trivalent indium chloride shown in Figure 36 supports the assumption of stepwise indium evaporation in the order of InCl₃>InCl₂>InCl in a similar temperature range as measured.

Figure 35: Progression-analysis of the chlorination of In_2O_3 with $\text{MgCl}_2 \cdot 6\text{H}_2\text{O}$ Figure 36: Development of vapor pressures of InCl_3 , InCl_2 and InCl at rising temperatures

The kinetic assessment of campaign 2 is shown in Figure 37. The R^2 -values of Kissinger-regressions range between 0.93–0.999, suggesting a valid fit. For the endothermic peak 4 which is believed to represent indium chlorination, an activation energy of 66.59 ± 0.19 kJ/mol ($R^2=0.999$) is calculated. E_a of the evaporation of InCl_3 was found to be 97.87 ± 2.29 kJ/mol ($R^2=0.930$). No literature data was found for comparison of obtained values.

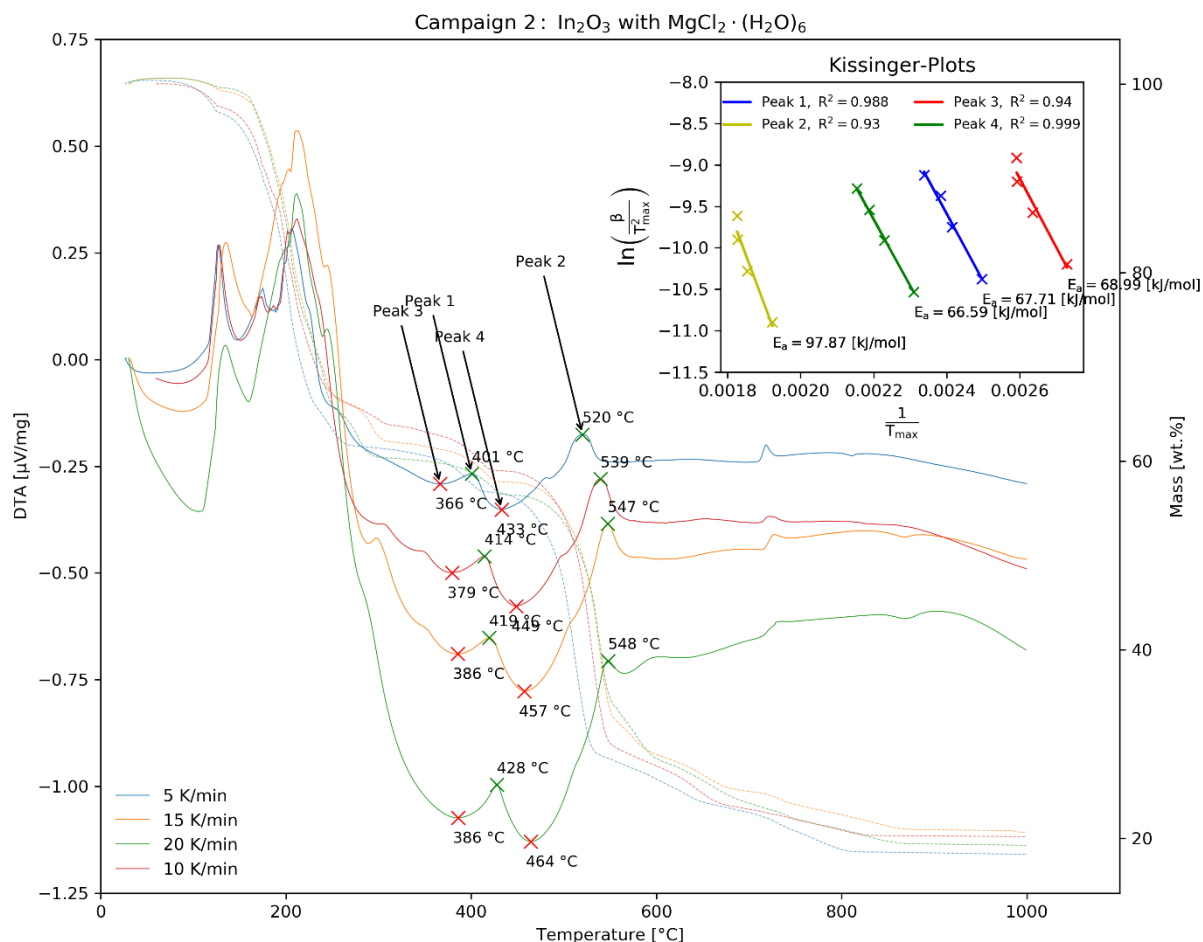
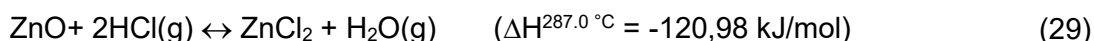


Figure 37: DTA- (solid lines) and mass- (dashed lines) curves for the chlorination of In_2O_3 with $\text{MgCl}_2 \cdot 6\text{H}_2\text{O}$ at 5, 10, 15 and 20 K/min, assessed endothermic (green crosses) and exothermic (red crosses) peaks and their Kissinger-plots with calculated activation energy

4.3.3 Campaign 3: Fe_2O_3 with $\text{AlCl}_3 \cdot 6\text{H}_2\text{O}$

The progression-analysis of campaign 3, where the chlorination of ZnO with $\text{FeCl}_3 \cdot 6\text{H}_2\text{O}$ is evaluated, is shown in Figure 38. As expected, no mass-loss occurs during the heating of pure zinc oxide (green lines) up to 1000 °C. The decomposition of the SCA (blue lines) progresses in stages. Both Müller et al. [93] and Kanungo [94] obtained similar mass- and DTA-curves in their assessment of thermal decomposition of $\text{FeCl}_3 \cdot 6\text{H}_2\text{O}$. They found the stages to be $\text{FeCl}_3 \cdot 6\text{H}_2\text{O} \xrightarrow{97\text{ °C}} \text{Fe}(\text{OH})\text{Cl}_2 \cdot \text{H}_2\text{O} \xrightarrow{188\text{ °C}} \text{Fe}(\text{OH})_2\text{Cl} \xrightarrow{207\text{ °C}} \text{FeOOH} \xrightarrow{437\text{ °C}} \text{Fe}_2\text{O}_3$ accompanied by the release of gaseous HCl during the first transitions [93]. Although the measured peaks and steps are similar to literature data, the residue-lines do not fit properly. This may be caused by the absorption of additional water during handling and grinding of the hygroscopic powder. This hypothesis is supported by the fact, that residue-lines fit better when considering higher water contents in the input material. Since the distinct endothermic peak of FeOOH -formation is not present in the mixture's DTA-curve (magenta dash dotted line), an endothermic reaction

is suspected to occur in the same temperature range. This reaction may be the chlorination of zinc oxide according to Equation 29, presenting an exothermic peak at 287.0 °C.



At a slightly higher temperature of 303.8 °C an endothermic peak is registered, which corresponds to the melting point of ZnCl_2 of 304 °C as found in literature [95]. The formed zinc chloride is then evaporated at an increasing rate until the remaining mass is precisely described by the Fe_2O_3 -residue-line. The highest rate of ZnCl_2 evaporation is marked by an endothermic peak at 658.3 °C.

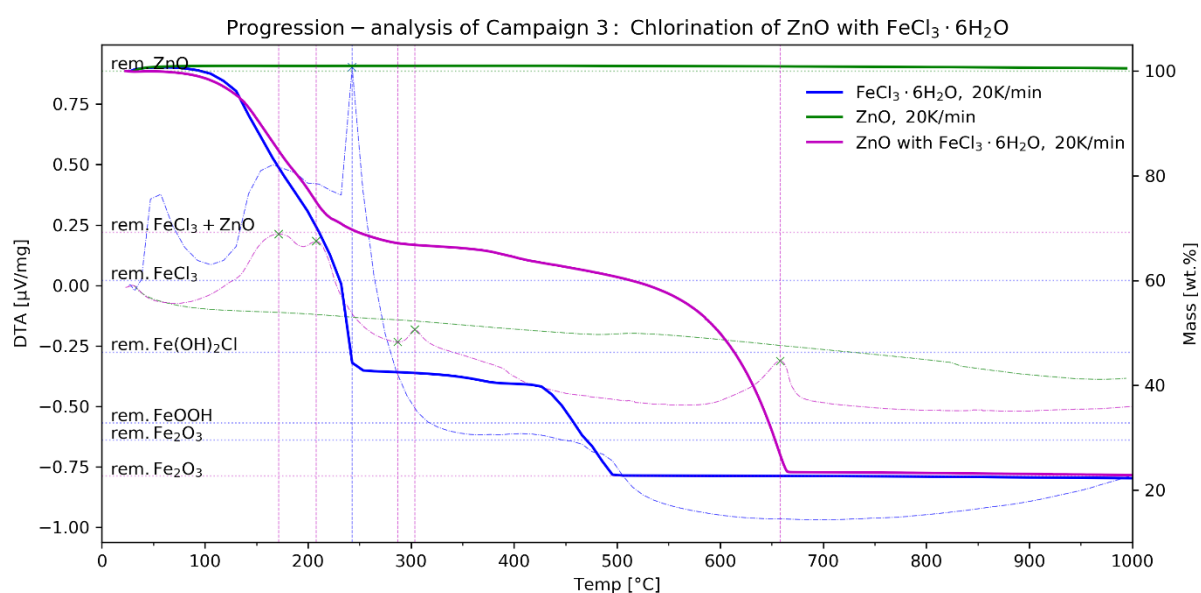


Figure 38: Progression-analysis of the chlorination of ZnO with $\text{FeCl}_3 \cdot 6\text{H}_2\text{O}$

The results of the kinetic assessment of Campaign 3 are shown in Figure 39. The activation energy of zinc chlorination (peak 3) is found to be 50.40 ± 1.10 kJ/mol with $R^2 = 0.938$. As in the case of AgCl , the melting of formed zinc chloride (peak 1) does not deliver plausible values through the applied Kissinger-method. A negative E_a of -91.85 kJ/mol is calculated with an R^2 of 0.043. On the other hand, the method generates a well fitting regression line ($R^2 = 0.992$) for the vaporization of ZnCl_2 (peak 2) resulting in an activation energy of 69.75 ± 0.52 kJ/mol. As before, literature did not provide evidence for validation of the obtained values.

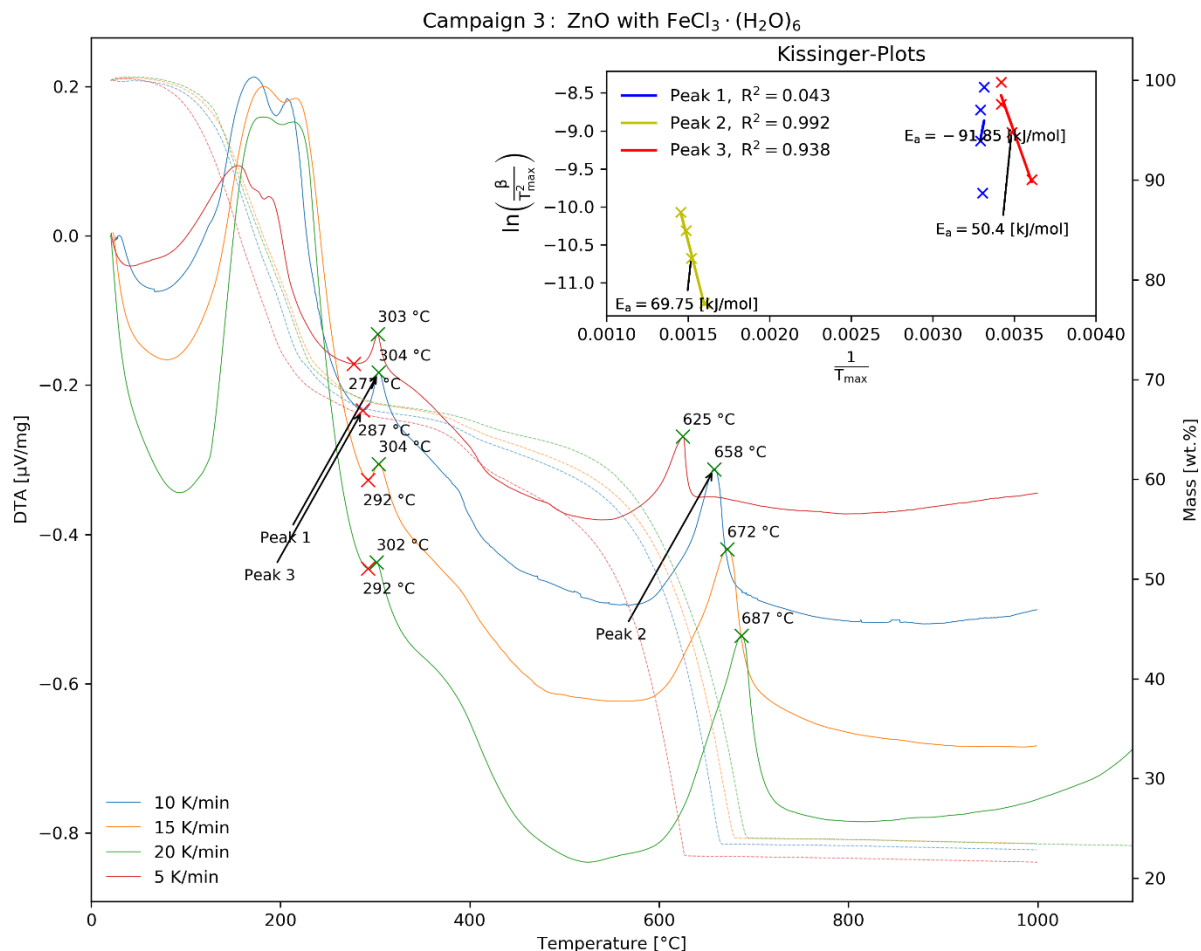
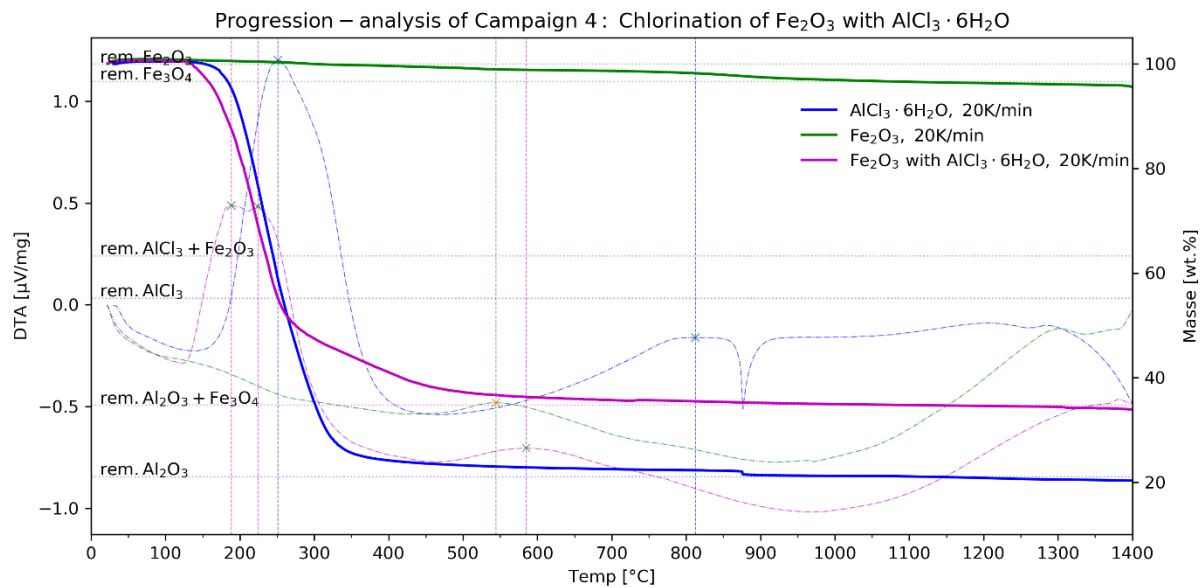


Figure 39: DTA- (solid lines) and mass- (dashed lines) curves for the chlorination of ZnO with $\text{FeCl}_3 \cdot 6\text{H}_2\text{O}$ at 5, 10, 15 and 20 K/min, assessed endothermic (green crosses) and exothermic (red crosses) peaks and their Kissinger-plots with calculated activation energy

4.3.4 Campaign 3: Fe_2O_3 with $\text{AlCl}_3 \cdot 6\text{H}_2\text{O}$

Finally, the chlorination of Fe_2O_3 with $\text{AlCl}_3 \cdot 6\text{H}_2\text{O}$ is assessed in Figure 40. A slight decrease in mass is noticed for pure Fe_2O_3 (green line), which can be well described by a transition into Fe_3O_4 , as the according residue-line fits the observed mass-loss. This behaviour was also described by Charvin et al. [96]. The thermal decomposition of $\text{AlCl}_3 \cdot 6\text{H}_2\text{O}$ (blue line) has already been analysed previously. The chlorination mixture represents the sum of both individual trials. The distinct initial mass-loss is most likely caused by decomposition of the SCA, while the slowly decreasing trend reflects the iron phase transition. The final mass-loss is best described by the $\text{Al}_2\text{O}_3 + \text{Fe}_3\text{O}_4$ residue-line. This strengthens the assumption, that iron oxide is neither chlorinated nor evaporated in the given chlorination scenario. Thus, the kinetic study shown in Figure 64 in the Appendix is not discussed in more detail.

Figure 40: Progression-analysis of the chlorination of Fe_2O_3 with $\text{AlCl}_3 \cdot 6\text{H}_2\text{O}$

5 Discussion

Before summarizing the obtained results, relevant aspects about their interpretation and validity are discussed for each assessment individually.

5.1 Comprehensive algorithmic simulation of chlorination reactions

In chapter 3, a comprehensive simulation algorithm based on thermochemical calculations was developed to thoroughly examine chlorination processes. The algorithm enables the evaluation of up to 9999 highly individualizable chlorination scenarios of freely selectable metals in one run by first generating a suitable reactant table, which can be imported into the FactSage Equilib computational software. Through the integration of various functions, quantitative iterations of all reaction conditions such as temperature, pressure or chlorine stoichiometry are possible. Moreover, all kinds of metals, SCAs, atmospheres and secondary compounds forming a virtual material matrix can be assessed. After exportation of the calculation results, products can be automatically set into comparison with input values, thus enabling the evaluation of the success of each individual scenario. Extraction rates are calculated and utilized for the discovery of conditions with favourable outcomes.

In the first step, the metals indium, silver, zinc, lead and iron are assessed individually to obtain knowledge about their respective behaviours and spot potentially exploitable differences among them. Their extraction rates generally increase with rising temperatures, reaching full extraction at lower temperatures when applying bi- or trichlorides instead of NaCl or KCl. The same holds true for the iteration of pressure, which only has significant impact on the monochlorides' extraction potential. Also increasing chlorine availability by rising relative SCA quantities favours metal extraction. Iron was found to be bound into solid compounds by certain species such as Ca or Mg. In an assessment of various atmospheres, secondary compounds and the present form of the to be extracted metal, scenarios of positive and negative influence have been identified. The heatmap shown in Figure 41 presents the deviations from mean extraction rates of assessed influential categories. Dark red squares indicate a significant improvement of 25 % or higher in respect to the mean metal extraction while dark blue colours illustrate a decrease of at least -25 %.

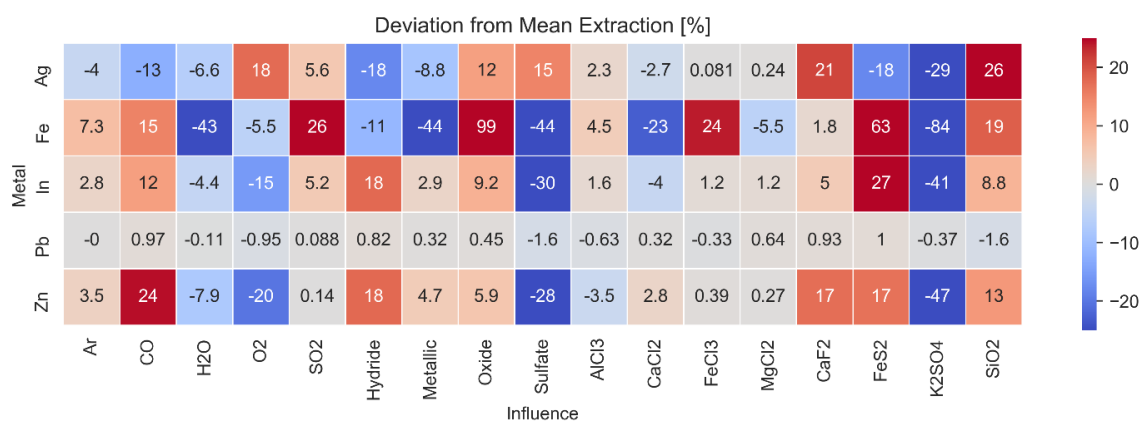


Figure 41: Deviations from the mean extraction rates considering all observed influences in [%], shades of red colours represent a positive influence, blue colours a negative one

Subsequently, a virtual jarosite mixture was assembled based on average concentrations found in literature [18–28] to simulate the chlorination behaviours of metal mixtures. However, it must be noted that all metals are present in their pure oxidic form instead of being bound in a jarosite structure, due to a lack of respective thermodynamic data.

Furthermore, a comprehensive extraction factor “Valex”, which represents the share of extracted value from the mock jarosite, was introduced to identify relevant scenarios more easily. When assessing metal mixtures competition for available chlorine exists, which favours the extraction of the ones with the highest affinity. Results showed that this condition distinctively enhances the selective chlorination of valuables in respect to the predominant iron phase. Numerous scenarios were identified, in which a practically full separation of the two phases is theoretically possible at considerable low temperatures. Also, the mitigation of iron extraction through binding in a solid phase in the presence of calcium compounds was found to present a possible way of increasing selectivity. Subsequently, qualitative evaluations of different atmospheres in combination with a set of secondary compounds showed that the least preferable scenarios include a reductive atmosphere and the presence of CaF₂ or FeS₂. The most positive influences on selective valuables extraction were observed in O₂-atmosphere and FeS₂ or CaSO₄ as secondary compound.

Finally, the effect of temperature and chlorine stoichiometry was assessed. High temperatures and chlorine additions turned out to be disadvantageous as increasing amounts of iron are extracted alongside the valuable metals. In the best scenarios, as illustrated in Figure 42, almost full Valex values (green circles) were achieved at already 600 °C and a chlorine stoichiometry of 1.00 or 800 °C and 0.25 respectively, while practically no iron enters the gas phase. Higher temperatures and chlorine additions lead to the extraction of increasing amounts of iron, as represented by the growing red circles, and should therefore be avoided.

Influence of temperature and chlorine stoichiometry on Valex (green) and iron extraction (red), O_2 – atmosphere and $CaSO_4$

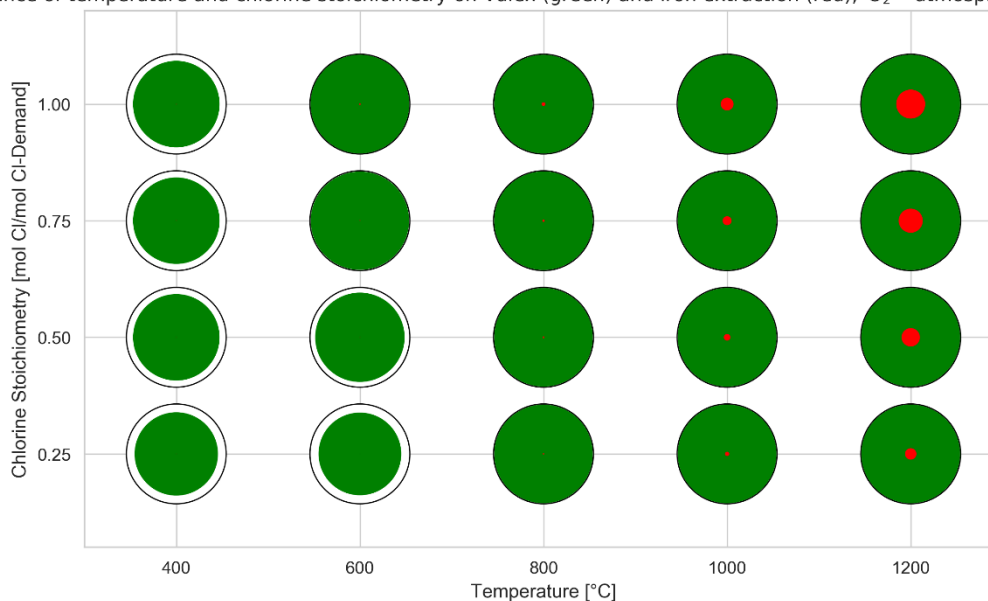


Figure 42: Influence of temperature and chlorine stoichiometry on Valex (green) and iron extraction (red) in O_2 -atmosphere and the presence of $CaSO_4$, the black circle represents a value of 1.00

To conclude, a broad variety of different influences was assessed on a thermochemical basis. Nevertheless, some potentially tremendous effects on chlorination reactions can not be implemented into the proposed simulation algorithm. Real mixtures are naturally inhomogeneous, which is further enhanced by incomplete mixing or segregation of the input material. This has significant consequences on chemical reactions and their products, as no complete contact of each present compound is guaranteed [73]. This inhomogeneity can also be increased by the melting of solid phases, thus reducing particle porosity, which inhibits the penetration of gaseous chlorine compounds [70]. Moreover, also temperature is not homogeneously distributed throughout the mixture, thus various reaction routes are possible simultaneously on different locations of the material. All these influences root in reaction kinetics, which are neglected in basic thermochemical calculations and can only be assessed by experimental investigation.

Furthermore, it must be pointed out that temperature dependencies obtained through simulation do not represent heating curves as produced by DTA measurements. Although mass-loss plots are easily realized by the algorithm, the theoretical basis is fundamentally different since all original input reactants are brought to reaction at every assessed temperature. On the contrary, in heating trials only the reaction products of already surpassed temperatures are available at respectively higher temperatures. Consequently, only isothermal experiments where the sample is brought to individually assessed temperatures as quickly as possible are suitable for the evaluation of correlations between simulation and practice.

5.2 Kinetic study of selected chlorination scenarios

In this work's final part, a kinetic study of four chlorination scenarios was carried out. A profound algorithm was developed to facilitate the identification of reaction mechanisms in terms of the exact sequence of chemical steps in which reactants are transformed into products as well as in the form of kinetic parameters. Through measurements of sample mixtures at different heating rates using a differential scanning calorimeter, an automatic calculation of the activation energies and frequency factors of relevant occurring reactions was achieved by the algorithm according to the Kissinger method. The maximum rate of chlorination reactions of Ag_2O , In_2O_3 and ZnO with previously released gaseous HCl were identified as an exothermic peak in the DTA-signal, which occurred at considerably low temperatures of $211.7\text{ }^\circ\text{C}$, $464.3\text{ }^\circ\text{C}$ and $287.0\text{ }^\circ\text{C}$ respectively. These assumptions are strengthened by the occurrence of subsequent endothermic peaks which correspond to the respective metal chloride's melting or sublimation point stated in literature. While an automatic evaluation of the activation energy of the chlorination of Ag_2O with $\text{AlCl}_3\cdot 6\text{H}_2\text{O}$ did not succeed, a value of $66.59\pm 0.19\text{ kJ/mol}$ ($R^2=0.999$) was found for In_2O_3 with $\text{MgCl}_2\cdot 6\text{H}_2\text{O}$ and $50.40\pm 1.10\text{ kJ/mol}$ ($R^2 = 0.938$) for ZnO with $\text{FeCl}_3\cdot 6\text{H}_2\text{O}$. Iron oxide was not chlorinated by $\text{AlCl}_3\cdot 6\text{H}_2\text{O}$ throughout the entire assessed temperature range of $20\text{--}1400\text{ }^\circ\text{C}$, in which a transition to Fe_3O_4 was observed instead.

Although activation energies of most relevant reactions of assessed chlorination scenarios were easily obtained and present considerably small standard deviations, they must be treated with caution. The simplicity of Kissinger-method's application often sacrifices validity as underlying assumptions are neglected. While in many cases the reaction order is falsely assumed as first order, this flaw generally does not result in large errors. On the other hand, major weakness of the method is its assumption of single-step kinetics. Since most processes to which the method is applied to occur in multiple steps, the yield of one single activation energy leads to inadequate conclusions. Moreover, a set of prerequisites must be met for the specific process in order to be suitable for the Kissinger method. For example, it only delivers valid outcome for melting processes where overheating occurs. This fact might also have led to the flawed activation energies of melting peaks assessed in this work. However, numerous improvements of the original Kissinger method have been developed to deal with certain shortcomings. Consequently, more profound research is necessary to either approve the applicability of the simplified Kissinger method for chlorination reactions or to identify better suitable evaluation schemes. [97]

6 Summary and outlook

In this work, a profound examination of problems and potentials related to iron precipitation residues from the zinc industry was conducted. The majority of globally produced zinc is won by roasting, leaching and electrowinning of predominantly sulfuric ores, which contain significant amounts of iron. To decrease zinc loss, leaching conditions are employed which also lead to the dissolution of comprised iron, which must be removed to avoid complications in the zinc electrolysis. For this purpose, the most commonly applied removal technique employs the precipitation of a complex basic iron sulfate with a jarosite structure. Next to iron and zinc, this material contains a wide range of other metals including indium, silver or lead. Regardless of its great potential as a secondary resource for the contained highly critical and valuable metals, the material has been directly or indirectly disposed of into the environment in the past decades until today. Although numerous recycling techniques have been developed to reduce ecological pressure and exploit the material's economic value, none of them is applied on an industrial scale apart from simple stabilization with cement. This is mainly due to either high investment costs of complex process design of hydrometallurgical approaches or the disadvantageous high energy demand and carbon emissions of pyrometallurgical solutions. Recently, a new promising technique was proposed which pursues the selective vaporization of valuable metals through their conversion into volatile chlorides.

An in-depth evaluation of the multi-metal recovery potential of such a process was carried out in the course of this work. The results derived from comprehensive thermochemical simulations underlined the great potential of a chlorination process to selectively extract valuable metals from iron precipitation residues. In many scenarios a complete extraction of indium, silver, zinc and lead was achieved while iron remained in the solid residue. Certain temperature and chlorine additions must not be surpassed to avoid the extraction of undesired iron.

To examine kinetic characteristics such as the sequence of chemical steps involved in chlorination processes or the determination of Arrhenius parameters, a set of small-scale experiments was conducted. Another algorithm was developed, which successfully enabled the automatic evaluation of reaction mechanisms and respective activation energies via the Kissinger method. Although the suitability of this scheme's application for chlorination processes is yet to be validated, the algorithm is not limited to reactions of this kind. On the contrary, it can be freely applied to any set of isothermal measurements of suitable chemical reactions with variable heating rates, which poses a great potential of facilitating all kinds of kinetic assessments in multiple fields of science.

To further assess the applicability of selective chlorination processes for metal recovery from iron precipitation residues, a comprehensive experimental trial must be conducted. Larger-

scale campaigns with real jarosite or goethite materials are required to compare the found theoretical potential with its practical feasibility. Ideally, correlations could be drawn by combining the experimentally obtained results with the existing simulation to develop a holistic recovery model. Such a model would pave the way for larger applications of the proposed recycling technique by identifying the most favourable process conditions for the selective valuable metal extraction of individually adjustable input materials. If successful, an adaption of this scientific approach to determine the most efficient process conditions for metal recovery to a wide variety of other residue materials appears viable in the future.

7 Literature

- [1] Bouckley E.: Global zinc demand to outpace production growth in 2021, narrowing surplus: UGMK | S&P Global Platts. Internet: <https://www.spglobal.com/platts/en/market-insights/latest-news/metals/031021-global-zinc-demand-to-outpace-production-growth-in-2021-narrowing-surplus-ugmk> (Access: 2021-05-03).
- [2] Mohr S. et al.: Global Projection of Lead-Zinc Supply from Known Resources. *Resources*, 7 (2018), 17.
- [3] Brown T. J. et al.: World Mineral Production 2014-18. British Geological Survey, Keyworth, Nottingham, UK (2020).
- [4] Chapman A. et al.: Study on Critical Raw Materials at EU Level (2013).
- [5] ILZSG: End Uses of Zinc. Internet: <https://www.ilzsg.org/static/enduses.aspx?from=1> (Access: 2021-03-16).
- [6] Ciacci L. et al.: Lost by Design. *Environmental science & technology*, 49 (2015), 9443–9451.
- [7] Graedel T. E. et al.: What Do We Know About Metal Recycling Rates? *Journal of Industrial Ecology*, 15 (2011), 355–366.
- [8] Graedel T. E. et al.: The Multilevel Cycle of Anthropogenic Zinc. *Journal of Industrial Ecology*, 9 (2005), 67–90.
- [9] Meylan G. and B. K. Reck: The anthropogenic cycle of zinc: Status quo and perspectives. *Resources, Conservation and Recycling*, 123 (2017), 1–10.
- [10] Antrekowitsch J. et al.: Zinc and Residue Recycling: Handbook of Recycling: Elsevier, 113–124.
- [11] Cusano G. et al.: Best Available Techniques (BAT) Reference Document for the Non-Ferrous Metals Industries (2017).
- [12] Sinclair R. J.: The extractive metallurgy of zinc. In: *Spectrum series / the Australasian Institute of Mining and Metallurgy*, Band: no. 13. Australasian Institute of Mining and Metallurgy, Carlton South, Vic. (2005).
- [13] Pawlek F.: *Metallhüttenkunde*. De Gruyter, Berlin (1983).
- [14] Dutrizac J. E.: The Behavior of Impurities during Jarosite Precipitation. *NATO Conference Series (VI Materials Science)* (1984), 125–169.

-
- [15] Matsuura D., Y. Usami and K. Ichiya: Recent Operational Improvements of Hematite Plant at Akita Zinc Co., Ltd., 130, 865–876.
- [16] Steinlechner S. and J. Antrekowitsch: Thermodynamic Considerations for a Pyrometallurgical Extraction of Indium and Silver from a Jarosite Residue. *Metals*, 8 (2018), 335.
- [17] Anderson C., C. Fleuriaux and L. Twidwell: Optimization Of An Industrial Ammonium Jarosite Production Circuit. *American Journal of Engineering Research* (2017) online proceedings.
- [18] Palden T. et al.: Selective Metal Recovery from Jarosite Residue by Leaching with Acid-Equilibrated Ionic Liquids and Precipitation-Stripping. *ACS Sustainable Chemistry & Engineering*, 7 (2019), 4239–4246.
- [19] Wang H. B., C. Z. Zheng and S. C. Qin: Study of a Novel Chloride Volatilization Process for the Treatment of Jarosite Residue. In: Siegmund, A., Alam, S., Grogan, J., Kerney, U., Shibata, E. (Hg.): PBZN 2020. The 9th international symposium on lead and zinc processing. [S.l.]: SPRINGER NATURE, 835–845.
- [20] Zhu D. et al.: New pyrometallurgical route for separation and recovery of Fe, Zn, In, Ga and S from jarosite residues. *Journal of Cleaner Production*, 205 (2018), 781–788.
- [21] Orko I. et al.: Hydrometallurgical Processing of Jarosite Waste to Value-Added Products (2016).
- [22] Ju S. et al.: Clean hydrometallurgical route to recover zinc, silver, lead, copper, cadmium and iron from hazardous jarosite residues produced during zinc hydrometallurgy. *Journal of hazardous materials*, 192 (2011), 554–558.
- [23] Liu C. et al.: Recovery of valuable metals from jarosite by sulphuric acid roasting using microwave and water leaching. *Canadian Metallurgical Quarterly*, 56 (2017), 1–9.
- [24] González-Ibarra A. A. et al.: Decomposition kinetics of industrial jarosite in alkaline media for the recovery of precious metals by cyanidation. *Canadian Metallurgical Quarterly*, 55 (2016), 448–454.
- [25] Metal recycling. United Nations Environment Programme, Nairobi, Kenya (2013).
- [26] Wegscheider S., S. Steinlechner and M. Leuchtenmüller: Innovative Concept for the Recovery of Silver and Indium by a Combined Treatment of Jarosite and Electric Arc Furnace Dust. *JOM*, 69 (2017), 388–394.
- [27] Calla-Choque D., F. Nava-Alonso and J. C. Fuentes-Aceituno: Acid decomposition and thiourea leaching of silver from hazardous jarosite residues: Effect of some cations on

- the stability of the thiourea system. *Journal of hazardous materials*, 317 (2016), 440–448.
- [28] Hage J. L. T. H.: Autoclave reduction of jarosites and other metal sulfates. In: *Geologica Ultraiectina*, Band: 169. Univ, Utrecht (1999).
- [29] London Metal Exchange: LME Zinc, 30.03.2021. Internet: <https://www.lme.com/en-GB/Metals/Non-ferrous/Zinc#tabIndex=2> (Access: 2021-03-30).
- [30] London Metal Exchange: LME Lead, 30.03.2021. Internet: <https://www.lme.com/en-GB/Metals/Non-ferrous/Lead#tabIndex=2> (Access: 2021-03-30).
- [31] London Metal Exchange: LME Copper, 30.03.2021. Internet: <https://www.lme.com/en-GB/Metals/Non-ferrous/Copper#tabIndex=2> (Access: 2021-03-30).
- [32] Kitco: Strategic Metals, 30.03.2021. Internet: <https://www.kitco.com/strategic-metals/> (Access: 2021-03-30).
- [33] Creedy S. et al.: Ausmelt Technology for Treating Zinc Residues. *World of Metallurgy - ERZMETALL*, 66 (2013), 230.
- [34] London Metal Exchange: LME Silver, 30.03.2021. Internet: <https://www.lme.com/Metals/Precious-metals/LME-Silver#tabIndex=1> (Access: 2021-03-30).
- [35] Dutrizac J. E. and J. L. Jambor: Jarosites and Their Application in Hydrometallurgy. *Reviews in Mineralogy and Geochemistry*, 40 (2000), 405–452.
- [36] Castro L. et al.: Reductive leaching of jarosites by *Aeromonas hydrophila*. *Minerals Engineering*, 95 (2016), 21–28.
- [37] Cruells M. et al.: Cyanidation kinetics of argentian jarosite in alkaline media. *Hydrometallurgy*, 55 (2000), 153–163.
- [38] Patiño F. et al.: Alkaline decomposition–cyanidation kinetics of argentian natrojarosite. *Hydrometallurgy*, 49 (1998), 323–336.
- [39] Abadías Llamas A. et al.: Resource Efficiency Evaluation of Pyrometallurgical Solutions to Minimize Iron-Rich Residues in the Roast-Leach-Electrowinning Process. In: Siegmund, A., Alam, S., Grogan, J., Kerney, U., Shibata, E. (Hg.): PBZN 2020. The 9th international symposium on lead and zinc processing. [S.l.]: SPRINGER NATURE, 351–364.
- [40] Mombelli D. et al.: Characterization of cast iron and slag produced by jarosite sludges reduction via Arc Transferred Plasma (ATP) reactor. *Journal of Environmental Chemical Engineering*, 6 (2018), 773–783.

-
- [41] Wang Y.-y. et al.: Comprehensive recovery of lead, zinc, and iron from hazardous jarosite residues using direct reduction followed by magnetic separation. *International Journal of Minerals, Metallurgy, and Materials*, 25 (2018), 123–130.
- [42] Yayun W. et al.: Study on recovery of lead, zinc, iron from jarosite residues and simultaneous sulfur fixation by direct reduction. *Physicochemical Problems of Mineral Processing* (2018), 517–526.
- [43] Sinha A. K. et al.: Recycling Jarofix Waste as a Construction Material for Embankment and Sub Grade. *Journal of Solid Waste Technology and Management* (2012), 169–180.
- [44] Sinha A. K., V. G. Havanagi and J. T. Shahu: Stabilised jarofix waste material for road construction. *International Journal of Pavement Engineering*, 170 (2019), 1–12.
- [45] Steinlechner S. and J. Antrekowitsch: Extraction of Zinc, Silver and Indium via Vaporization from Jarosite Residue. In: Gaustad, G., Fleurialt, C., Gökelma, M., Howarter, J. A., Kirchain, R., Ma, K., Meskers, C., Neelameggham, N. R., Olivetti, E., Powell, A. C., Tesfaye, F., Verhulst, D., Zhang, M. (Hg.): *REWAS 2019*. Cham: Springer International Publishing, 189–195.
- [46] Wang Y. et al.: Comprehensive recovery and recycle of jarosite residues from zinc hydrometallurgy. *Chemical Engineering Journal Advances*, 3 (2020) online proceedings.
- [47] Pachauri R. K. and L. Mayer (Ed.): *Climate change 2014*. Intergovernmental Panel on Climate Change, Geneva, Switzerland (2015).
- [48] Steffen W. et al.: The trajectory of the Anthropocene: The Great Acceleration. *The Anthropocene Review*, 2 (2015), 81–98.
- [49] International Energy Agency: Global primary energy demand by fuel, 1925-2019. Internet: <https://www.iea.org/data-and-statistics/charts/global-primary-energy-demand-by-fuel-1925-2019> (Access: 2021-03-31).
- [50] International Energy Agency: *World Energy Outlook 2020*.
- [51] Mrotzek-Blöß A. et al.: Recyclingpotenzial von Technologiemetallen und anderen kritischen Rohstoffen als wichtige Säule der Rohstoffversorgung (Recyclingpotenzial Technologiemetalle). Fraunhofer-Institut für Umwelt-, Sicherheits- und Energietechnik UMSICHT (2015).
- [52] Exner A.; M. Held and K. Kümmerer (Ed.): *Kritische Metalle in der Großen Transformation*. Springer Spektrum, Place of publication not identified (2016).

- [53] Fthenakis V., W. Wang and H. C. Kim: Life cycle inventory analysis of the production of metals used in photovoltaics. *Renewable and Sustainable Energy Reviews*, 13 (2009), 493–517.
- [54] Kausch P. et al.: *Strategische Rohstoffe, Risikovorsorge*. Springer Spektrum, Berlin (2014).
- [55] Kanari N. et al.: Kinetics of hematite chlorination with Cl₂ and Cl₂+O₂: Part I. Chlorination with Cl₂. *Thermochimica Acta*, 497 (2010), 52–59.
- [56] Kanari N. et al.: An overview study of chlorination reactions applied to the primary extraction and recycling of metals and to the synthesis of new reagents. *Thermochimica Acta*, 495 (2009), 42–50.
- [57] Barbosa L. I., N. G. Valente and J. A. González: Kinetic study on the chlorination of β-spodumene for lithium extraction with Cl₂ gas. *Thermochimica Acta*, 557 (2013), 61–67.
- [58] Huang Q. et al.: Effect of HCl/SO₂/NH₃/O₂ and mineral sorbents on the partitioning behaviour of heavy metals during the thermal treatment of solid wastes. *Environmental technology*, 36 (2015) online proceedings.
- [59] Yajima K., H. Matsuura and F. Tsukihashi: Chlorination and Evaporation Behaviors of Zinc Oxide in Ar- HCl-O₂ Atmosphere. *High Temperature Materials and Processes*, 30 (2011), 10.
- [60] Nowak B. et al.: Heavy metal removal from MSW fly ash by means of chlorination and thermal treatment: Influence of the chloride type. *Chemical Engineering Journal*, 179 (2012), 178–185.
- [61] Cui F. et al.: The selective chlorination of nickel and copper from low-grade nickel-copper sulfide-oxide ore: Mechanism and kinetics. *Separation and Purification Technology*, 239 (2020) online proceedings.
- [62] Mu W. et al.: A novel process for simultaneously extracting Ni and Cu from mixed oxide-sulfide copper-nickel ore with highly alkaline gangue via FeCl₃·6H₂O chlorination and water leaching. *Hydrometallurgy*, 191 (2020) online proceedings.
- [63] Lorenz T. and M. Bertau: Recycling of rare earth elements from FeNdB-Magnets via solid-state chlorination. *Journal of Cleaner Production*, 215 (2019), 131–143.
- [64] Menad N. and B. Björkman: Polyvinyl chloride used as a chlorinating and a reducing agent. *Resources, Conservation and Recycling*, 24 (1998), 257–274.

- [65] Fraissler G. et al.: Influence of dry and humid gaseous atmosphere on the thermal decomposition of calcium chloride and its impact on the remove of heavy metals by chlorination. *Chemical Engineering and Processing: Process Intensification*, 48 (2009), 380–388.
- [66] Chan C. et al.: The behaviour of selected heavy metals in MSW incineration electrostatic precipitator ash during roasting with chlorination agents. *Journal of hazardous materials*, 50 (1996), 1–13.
- [67] Outotec: HSC Chemistry.
- [68] Qin H. et al.: Pyrite enhanced chlorination roasting and its efficacy in gold and silver recovery from gold tailing. *Separation and Purification Technology*, 250 (2020) online proceedings.
- [69] Yu J. et al.: Mechanism on heavy metals vaporization from municipal solid waste fly ash by $\text{MgCl}_2 \cdot 6\text{H}_2\text{O}$. *Waste management (New York, N.Y.)*, 49 (2016), 124–130.
- [70] Lei C. et al.: Reaction characteristics and kinetics of gallium in chlorination roasting of copper tailings using calcium chloride. *Rare Metals*, 16 (2015) online proceedings.
- [71] Li H. et al.: Investigation on the recovery of gold and silver from cyanide tailings using chlorination roasting process. *Journal of Alloys and Compounds*, 763 (2018), 241–249.
- [72] Kurashima K. et al.: A combined kinetic and thermodynamic approach for interpreting the complex interactions during chloride volatilization of heavy metals in municipal solid waste fly ash. *Waste management (New York, N.Y.)*, 87 (2019), 204–217.
- [73] Fraissler G. et al.: Thermodynamic equilibrium calculations concerning the removal of heavy metals from sewage sludge ash by chlorination. *Chemical Engineering and Processing: Process Intensification*, 48 (2009), 152–164.
- [74] Alfa Aesar: Indium(III) chloride, ultra dry, 99.999% (metals basis) - Product Overview. Internet: <https://www.alfa.com/de/catalog/044349/> (Access: 2021-04-01).
- [75] AZO Materials: Zinc Oxide – Properties, Applications and the Future for ZnO. Internet: <https://www.azom.com/article.aspx?ArticleID=5818> (Access: 2021-05-19).
- [76] Chan C. C.Y. and D. W. Kirk: Behaviour of metals under the conditions of roasting MSW incinerator fly ash with chlorinating agents. *Journal of hazardous materials*, 64 (1999), 75–89.
- [77] Bale C. W. et al.: FactSage. Internet: www.factsage.com (2010-2016).
- [78] Harris C. R. et al.: Array programming with NumPy. *Nature* (2020), 357–362.
- [79] Reback J. et al.: Pandas (2020).

- [80] Ambethkar H. R.: chemlib. Internet: <https://github.com/harirakul/chemlib> (2020).
- [81] Gallagher P. K., M. E. Brown and R. B. Kemp: Handbook of thermal analysis and calorimetry. Elsevier, Amsterdam, Oxford (1998).
- [82] Kissinger H. E.: Reaction Kinetics in Differential Thermal Analysis. Analytical Chemistry, 29 (1957), 1702–1706.
- [83] Blaine R. L. and H. E. Kissinger: Homer Kissinger and the Kissinger equation. Thermochemica Acta, 540 (2012), 1–6.
- [84] ACS Publications: Reaction Kinetics in Differential Thermal Analysis. Internet: <https://pubs.acs.org/doi/10.1021/ac60131a045> (Access: 2021-04-29).
- [85] Liu P. et al.: Study on the reduction roasting of spent $\text{LiNi}_{0.8}\text{Co}_{0.1}\text{Mn}_{0.1}\text{O}_2$ lithium-ion battery cathode materials. Journal of Thermal Analysis and Calorimetry, 136 (2019), 1323–1332.
- [86] Yang Y. et al.: Rare Earth Recovery from Fluoride Molten-Salt Electrolytic Slag by Borax Roasting-Hydrochloric Acid Leaching. JOM, 72 (2020), 939–945.
- [87] Virtanen P. et al.: SciPy 1.0: Fundamental Algorithms for Scientific Computing in Python. Nature Methods, 17 (2020), 261–272.
- [88] Cava S. et al.: Structural characterization of phase transition of Al_2O_3 nanopowders obtained by polymeric precursor method. Materials Chemistry and Physics, 103 (2007), 394–399.
- [89] Sigma-Aldrich: Silberchlorid. Internet: <https://www.sigmaaldrich.com/catalog/product/aldrich/204382?lang=de®ion=AT> (Access: 2021-05-01).
- [90] Huang Q. et al.: Thermal decomposition mechanisms of $\text{MgCl}_2 \cdot 6\text{H}_2\text{O}$ and $\text{MgCl}_2 \cdot \text{H}_2\text{O}$. Journal of Analytical and Applied Pyrolysis, 91 (2011), 159–164.
- [91] Takahashi K. et al.: Recovering Indium from the Liquid Crystal Display of Discarded Cellular Phones by Means of Chloride-Induced Vaporization at Relatively Low Temperature. Metallurgical and Materials Transactions A, 40 (2009), 891–900.
- [92] Park K.-S. et al.: Recovery of indium from In_2O_3 and liquid crystal display powder via a chloride volatilization process using polyvinyl chloride. Thermochemica Acta, 493 (2009), 105–108.
- [93] Müller M., J. C. Villalba and F. J. Anaisi: Decomposição térmica (TG-DTA) de sais de ferro $[\text{FeCl}_3 \cdot 6\text{H}_2\text{O}]$ e $[\text{Fe}(\text{NO}_3)_3 \cdot 9\text{H}_2\text{O}]$ com análise morfológica e química do produto final. Semina: Ciências Exatas e Tecnológicas, 35 (2014), 9.

-
- [94] Kanungo S. B. and S. K. Mishra: Thermal dehydration and decomposition of $\text{FeCl}_3 \cdot x\text{H}_2\text{O}$. *Journal of Thermal Analysis and Calorimetry*, 46 (1996), 1487–1500.
- [95] Carl Roth: Zinkchlorid, 500 g. Internet: <https://www.carlroth.com/de/de/zinksalze-zn/zinkchlorid/p/t887.1> (Access: 2021-05-02).
- [96] Charvin P. et al.: Hydrogen Production by Three-Step Solar Thermochemical Cycles Using Hydroxides and Metal Oxide Systems. *Energy & Fuels*, 21 (2007), 2919–2928.
- [97] Vyazovkin S.: Kissinger Method in Kinetics of Materials: Things to Beware and Be Aware of. *Molecules* (Basel, Switzerland), 25 (2020) online proceedings.

8 List of Figures

Figure 1:	Roasting-leaching flow-sheet [12].....	2
Figure 2:	Schematic flow sheet of the jarosite process [12]	4
Figure 3:	Coupling of accelerating economic and population growth with other sectors since the beginning of industrialization in 1750 [48]	8
Figure 4:	Different behavioural paths of an SCA during the chlorination roasting process	11
Figure 5:	Comparison of the vapor pressure of assessed SCAs as a function of temperature	12
Figure 6:	Comparison of different chlorine release potentials of selected SCAs	14
Figure 7:	Different behavioural paths of a metal compound during a chlorination calcination process	15
Figure 8:	Comparison of different chlorination potentials of certain metal oxides with chlorine gas and HCl as a function of temperature (calculated in a closed system)	16
Figure 9:	Comparison of vapour pressures of indium (red), silver (green), iron (magenta), zinc (blue) and lead (black) in their metallic form (solid lines), their corresponding chlorides (dashed lines) and, if applicable, oxides (dotted lines) as a function of temperature (calculated in a closed system)	18
Figure 10:	Comparison of thermodynamic reaction potentials of previously assessed chlorine release or chlorination paths with a direct reaction between $MgCl_2$, ZnO	20
Figure 11:	Influence of temperature on extraction rates of In, Ag, Zn, Pb and Fe using NaCl (dash dotted lines), $MgCl_2$ (dashed lines, mostly invisible because of overlapping) or $AlCl_3$ (solid lines).....	26
Figure 12:	Formation of various solid (solid lines) and gaseous (dashed lines) compounds in the Fe_2O_3 - $MgCl_2$ -system as a function of temperature.....	26
Figure 13:	Influence of pressure on extraction rates of assessed metals using NaCl as SCA.....	27
Figure 14:	Influence of stoichiometry on extraction rates using $AlCl_3$ as SCA at various temperatures.....	28
Figure 15:	Formation of various solid (solid lines) and gaseous (dashed lines) compounds in the PbO - $AlCl_3$ -system as a function of chlorine stoichiometry (800 °C).....	29

Figure 16:	Influence of the variation of the SCA including MgCl_2 and AlCl_3 expressed as the deviation from mean silver extraction (36.3 %)	31
Figure 17:	Influence of the variation of the SCA including NaCl , MgCl_2 and AlCl_3 expressed as the deviation from mean silver extraction (26.9 %)	31
Figure 18:	Influence of the variation of SCA on extraction rates	32
Figure 19:	Influence of the variation of the metal's form on extraction rates	32
Figure 20:	Influence of the variation of secondary compounds on extraction rates	32
Figure 21:	Influence of the variation of the atmosphere on extraction rates	33
Figure 22:	Comparison of extraction rates of individually assessed metals (transparent lines) and from mixtures (bold lines) as a function of temperature.....	35
Figure 23:	Influence of temperature and atmospherical conditions on extraction rates of indium, silver, zinc, lead and iron from mock jarosite using CaCl_2 as SCA.....	36
Figure 24:	Formation of various solid (solid lines) and gaseous (dashed lines) iron compounds as well as solid (dash dotted) and gaseous (dotted) compounds of CaCl_2 during chlorination of mock jarosite as a function of temperature.....	37
Figure 25:	Influence of temperature on Valex and iron extraction from mock jarosite mixture using NaCl , KCl , MgCl_2 (mostly overlapping), CaCl_2 , AlCl_3 or FeCl_3 (mostly overlapping) as SCA, pressure of 1 atm, stoichiometry of 1 and inert atmosphere.....	39
Figure 26:	Influence of various SCAs (left), secondary compounds (middle) and atmospheres (right) on extraction rates of Valex (upper) and iron (middle) and the difference between both (lower), where iron extraction is weighted 5-fold, pressure of 1 atm and stoichiometry of 1	40
Figure 27:	Influence of the variation of atmosphere and secondary compounds on iron extraction rates at 1200 °C, 1 atm and stoichiometry of 1	41
Figure 28:	Influence of the variation of atmosphere and secondary compounds on Valex rates at 600 °C, 1 atm and stoichiometry of 1	41
Figure 29:	Deviation from mean Valex for various atmospheres in combination with different secondary compounds and SCAs for full temperature range, 1 atm and stoichiometry of 1.....	42
Figure 30:	Difference between Valex and 5-fold iron extraction for various atmospheres in combination with different secondary compounds, mean of all assessed temperatures, pressure of 1 atm and stoichiometry of 1	42

Figure 31:	Difference between Valex and 5-fold iron extraction for various atmospheres in combination with different secondary compounds, anhydrous and hydrated SCAs, mean values for temperatures, pressure of 1 atm and stoichiometry of 1.....	43
Figure 32:	Influence of temperature and chlorine stoichiometry on mean Valex (green) and iron extraction (red) including all previously stated parameters, the black circle represents a value of 1.00.....	44
Figure 33:	Progression-analysis of the chlorination of Ag_2O with $\text{AlCl}_3 \cdot 6\text{H}_2\text{O}$, mass- and DTA-signals of pure Ag_2O (green lines), pure and $\text{AlCl}_3 \cdot 6\text{H}_2\text{O}$ (blue lines) and the mixture (magenta lines).....	50
Figure 34:	DTA- (solid lines) and mass-curves (dashed lines) for the chlorination of Ag_2O with $\text{AlCl}_3 \cdot 6\text{H}_2\text{O}$ at 5, 10, 15 and 20 K/min, assessed endothermic (green crosses) and exothermic (red crosses) peaks and their Kissinger-plots with calculated activation energy.....	50
Figure 35:	Progression-analysis of the chlorination of In_2O_3 with $\text{MgCl}_2 \cdot 6\text{H}_2\text{O}$	52
Figure 36:	Development of vapor pressures of InCl_3 , InCl_2 and InCl at rising temperatures.....	52
Figure 37:	DTA- (solid lines) and mass- (dashed lines) curves for the chlorination of In_2O_3 with $\text{MgCl}_2 \cdot 6\text{H}_2\text{O}$ at 5, 10, 15 and 20 K/min, assessed endothermic (green crosses) and exothermic (red crosses) peaks and their Kissinger-plots with calculated activation energy.....	53
Figure 38:	Progression-analysis of the chlorination of ZnO with $\text{FeCl}_3 \cdot 6\text{H}_2\text{O}$	54
Figure 39:	DTA- (solid lines) and mass- (dashed lines) curves for the chlorination of ZnO with $\text{FeCl}_3 \cdot 6\text{H}_2\text{O}$ at 5, 10, 15 and 20 K/min, assessed endothermic (green crosses) and exothermic (red crosses) peaks and their Kissinger-plots with calculated activation energy.....	55
Figure 40:	Progression-analysis of the chlorination of Fe_2O_3 with $\text{AlCl}_3 \cdot 6\text{H}_2\text{O}$	56
Figure 41:	Deviations from the mean extraction rates considering all observed influences in [%], shades of red colours represent a positive influence, blue colours a negative one.....	58
Figure 42:	Influence of temperature and chlorine stoichiometry on Valex (green) and iron extraction (red) in O_2 -atmosphere and the presence of CaSO_4 , the black circle represents a value of 1.00.....	59
Figure 43:	Comparison of different chlorine release potentials of selected gaseous SCAs.....	77
Figure 44:	Comparison of free Gibbs energy of chlorine release of CaCl_2 with (green and magenta lines) and without (red lines) reactions with	

	secondary components. When reactions can occur in both dry and humid atmosphere, formed chlorine agent is put in brackets.	77
Figure 45:	Comparison of free Gibbs energy of chlorine release of $MgCl_2$ with (green and magenta lines) and without (red lines) reactions with secondary components. When reactions can occur in both dry and humid atmosphere, formed chlorine agent is put in brackets.	78
Figure 46:	Influence of temperature on extraction rates of In, Ag, Zn, Pb and Fe using $CaCl_2$ (solid lines) or $FeCl_3$ (dashed lines).....	79
Figure 47:	Influence of pressure on extraction rates of assessed metals using $MgCl_2$ as SCA.....	79
Figure 48:	Influence of pressure on extraction rates of assessed metals using $AlCl_3$ as SCA.....	80
Figure 49:	Influence of pressure on extraction rates of assessed metals using $MgCl_2$ as SCA.....	80
Figure 50:	Influence of pressure on extraction rates of assessed metals using $FeCl_3$ as SCA.....	81
Figure 51:	Formation of various solid (solid lines) and gaseous (dashed lines) compounds in the $ZnO-AlCl_3$ -system in dependence of chlorine stoichiometry (1000 °C).....	81
Figure 52:	Influence of stoichiometry on extraction rates using $MgCl_2$ as SCA at various temperatures, pressure of 1 atm and inert atmosphere.....	82
Figure 53:	Influence of stoichiometry on extraction rates using $NaCl$ as SCA at various temperatures, pressure of 1 atm and inert atmosphere.....	82
Figure 54:	Influence of stoichiometry on extraction rates using $FeCl_3$ as SCA at various temperatures, pressure of 1 atm and inert atmosphere.....	83
Figure 55:	Influence of stoichiometry on extraction rates using $CaCl_2$ as SCA at various temperatures, pressure of 1 atm and inert atmosphere.....	83
Figure 56:	Influence of temperature on extraction rates of indium, silver, zinc, lead and iron from mock jarosite mixture using KCl , $CaCl_2$ or $FeCl_3$ as SCA.....	84
Figure 57:	Formation of various solid (solid lines) and gaseous (dashed lines) iron compounds as well as solid (dash dotted) and gaseous (dotted) compounds of $CaCl_2$ during chlorination of mock jarosite as a function of temperature in O_2 -atmosphere	85
Figure 58:	Formation of various solid (solid lines) and gaseous (dashed lines) iron compounds as well as solid (dash dotted) and gaseous (dotted) compounds of $CaCl_2$ during chlorination of mock jarosite as a function of temperature in Ar-atmosphere.....	85

Figure 59:	Formation of various solid (solid lines) and gaseous (dashed lines) iron compounds as well as solid (dash dotted) and gaseous (dotted) compounds of CaCl_2 during chlorination of mock jarosite as a function of temperature in CO-atmosphere	86
Figure 60:	Deviation from mean iron extraction for various atmospheres in combination with different secondary compounds and SCAs for full temperature range, 1 atm and stoichiometry of 1.....	86
Figure 61:	Difference between Valex and 5-fold iron extraction for various atmospheres with anhydrous and hydrated SCAs, mean values for temperatures, pressure of 1 atm and stoichiometry of 1	87
Figure 62:	Influence of temperature and chlorine stoichiometry on Valex (green) and iron extraction (red) in CO-atmosphere and the presence of CaF_2 , the black circle represents a value of 1.00.....	87
Figure 63:	Influence of temperature and chlorine stoichiometry on Valex (green) and iron extraction (red) in O_2 -atmosphere and the presence of CaSO_4 , the black circle represents a value of 1.00.....	88
Figure 64:	DTA- (solid lines) and mass- (dashed lines) curves for the chlorination of Fe_2O_3 with $\text{AlCl}_3 \cdot 6\text{H}_2\text{O}$ at 5, 10, 15 and 20 K/min, assessed endothermic (green crosses) and exothermic (red crosses) peaks and their Kissinger-plots with calculated activation energy.....	88

9 List of Tables

Table 1:	Typical characteristics of common iron precipitation residues.....	5
Table 2:	Typical concentration ranges and current market price of valuable metals contained in jarosite and goethite	5
Table 3:	Boiling points of assessed metals, their most stable chlorides and, if applicable, their oxides according to HSC Chemistry [67].....	17
Table 4:	Metal concentrations used for simulating the mock jarosite mixture.....	34
Table 5:	Assessed metal compounds and SCAs alongside the maximum temperature.....	47
Table 6:	Overview of assessed qualitative influences.....	84

10 Appendix

Chapter 2

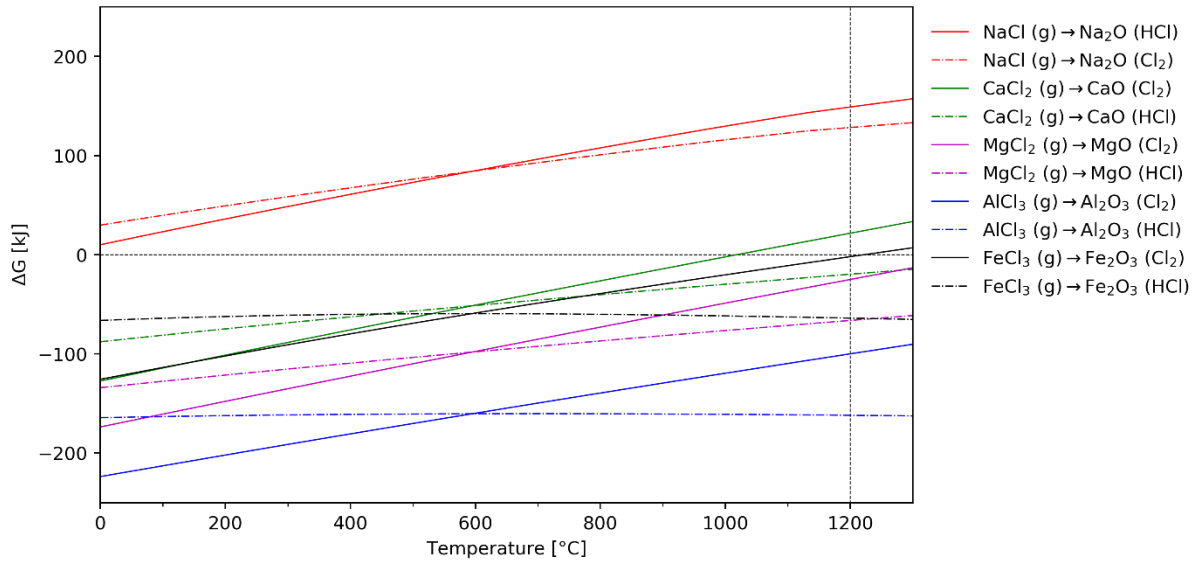


Figure 43: Comparison of different chlorine release potentials of selected gaseous SCAs

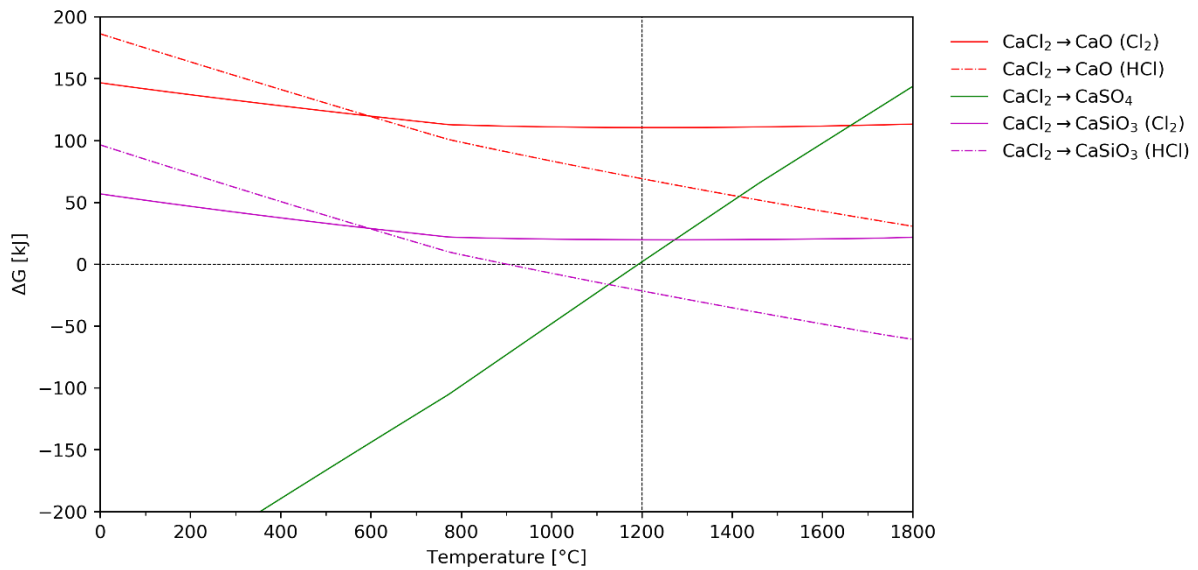


Figure 44: Comparison of free Gibbs energy of chlorine release of CaCl_2 with (green and magenta lines) and without (red lines) reactions with secondary components. When reactions can occur in both dry and humid atmosphere, formed chlorine agent is put in brackets.

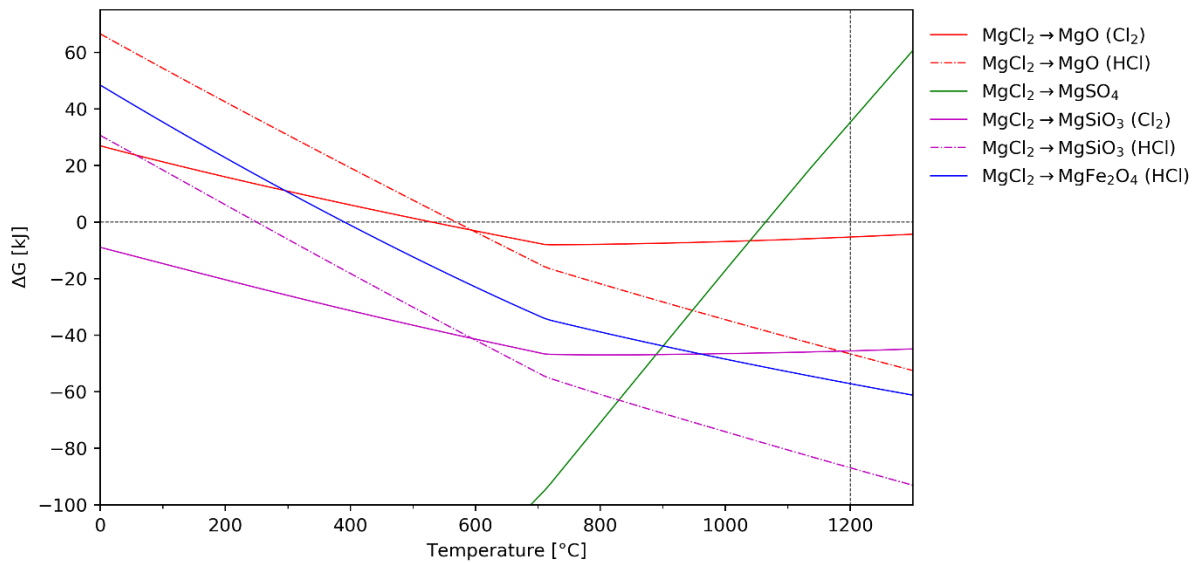
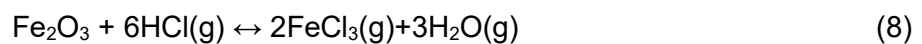
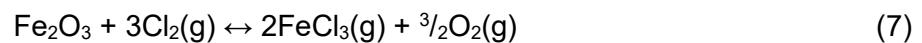
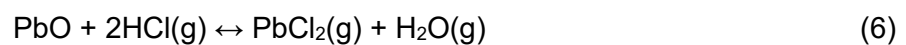
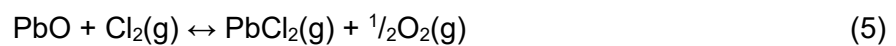
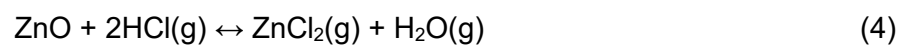
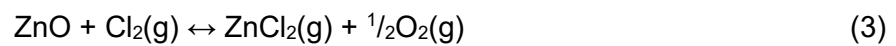
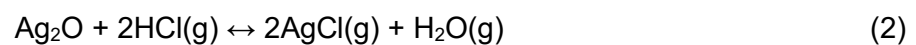
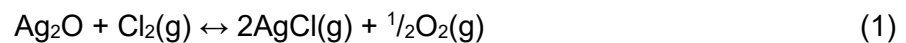


Figure 45: Comparison of free Gibbs energy of chlorine release of MgCl_2 with (green and magenta lines) and without (red lines) reactions with secondary components. When reactions can occur in both dry and humid atmosphere, formed chlorine agent is put in brackets.

Chlorination reactions of Ag-, Zn-, Pb- and Fe-oxide using chlorine gas



Chapter 3

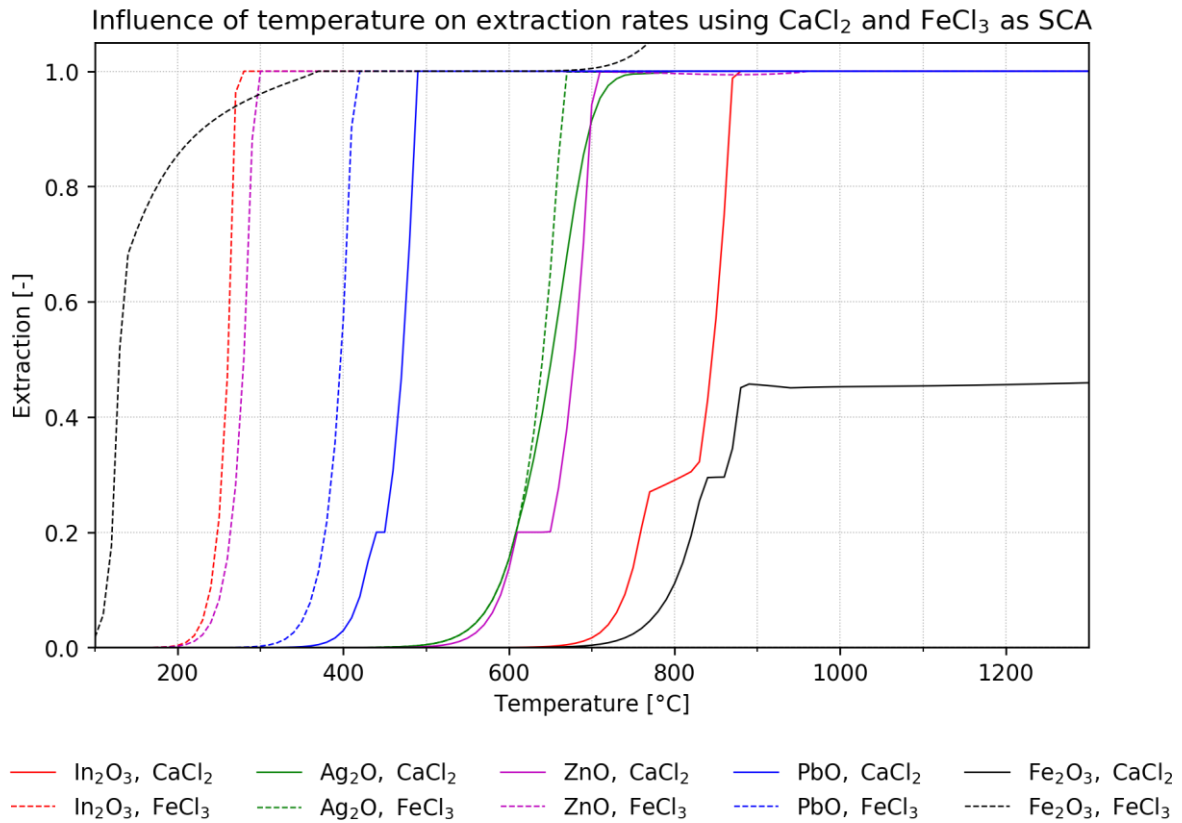


Figure 46: Influence of temperature on extraction rates of In, Ag, Zn, Pb and Fe using CaCl_2 (solid lines) or FeCl_3 (dashed lines)

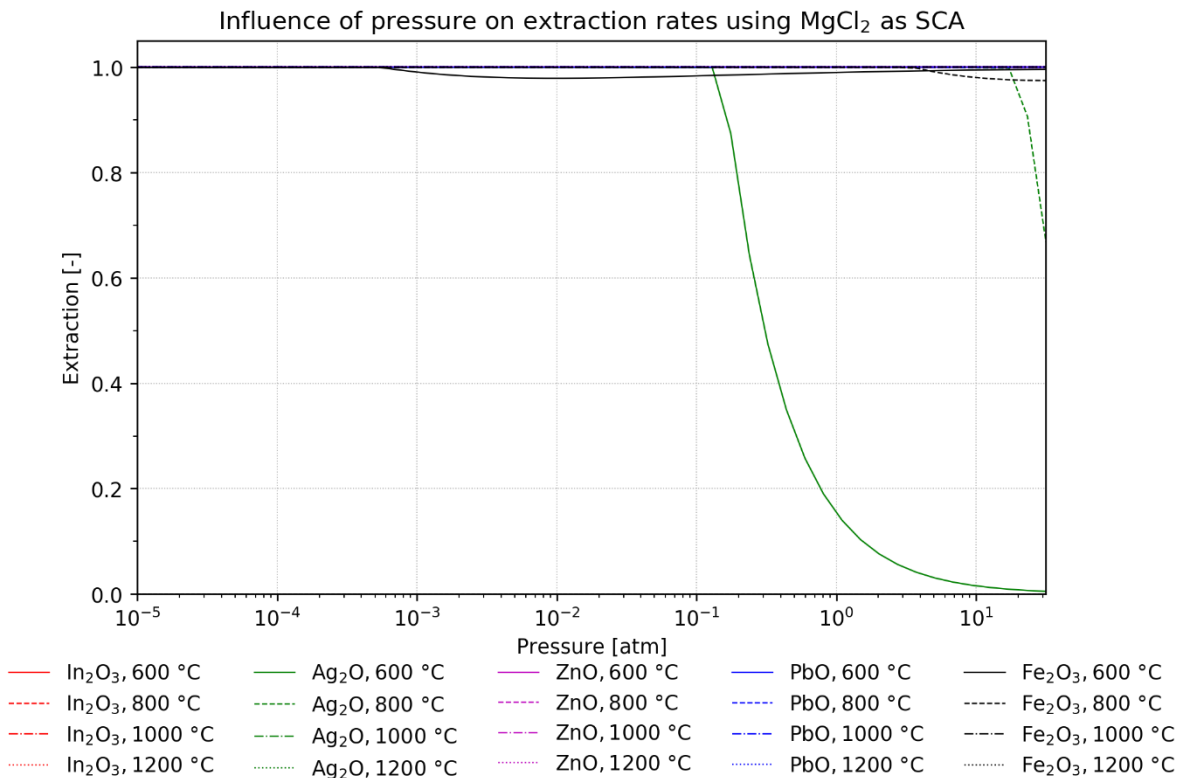


Figure 47: Influence of pressure on extraction rates of assessed metals using MgCl_2 as SCA

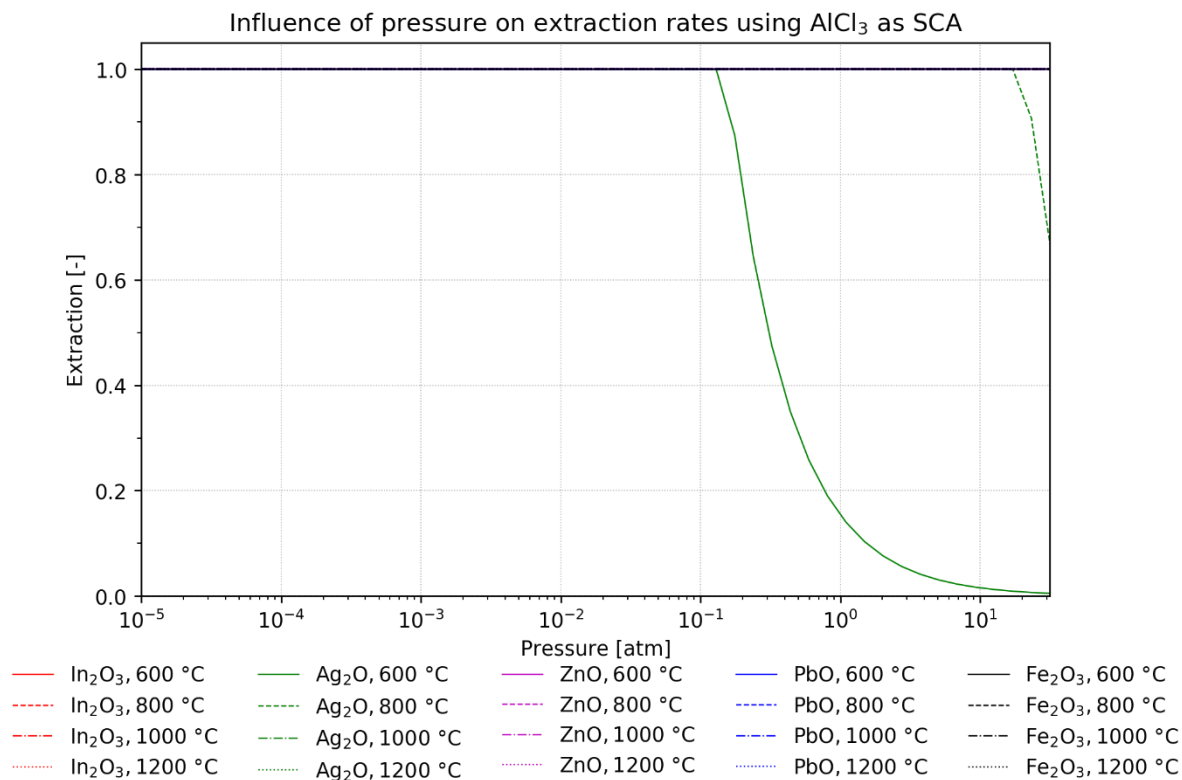


Figure 48: Influence of pressure on extraction rates of assessed metals using AlCl_3 as SCA

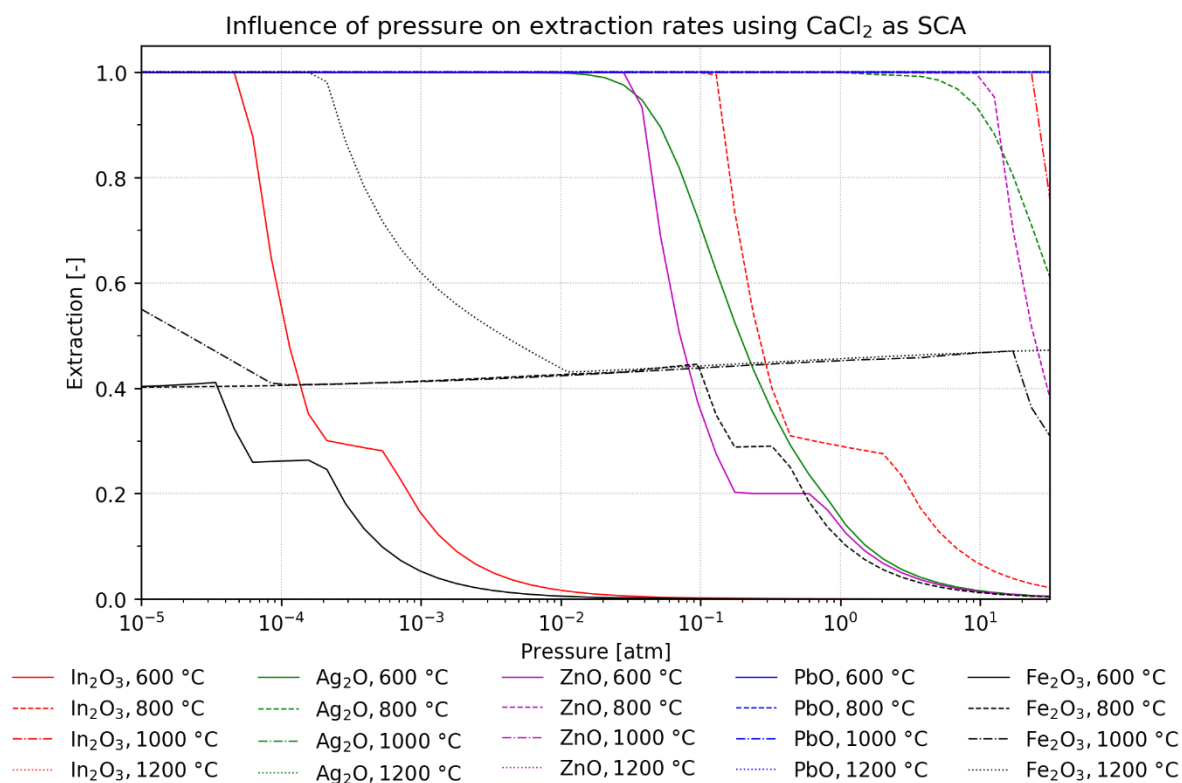
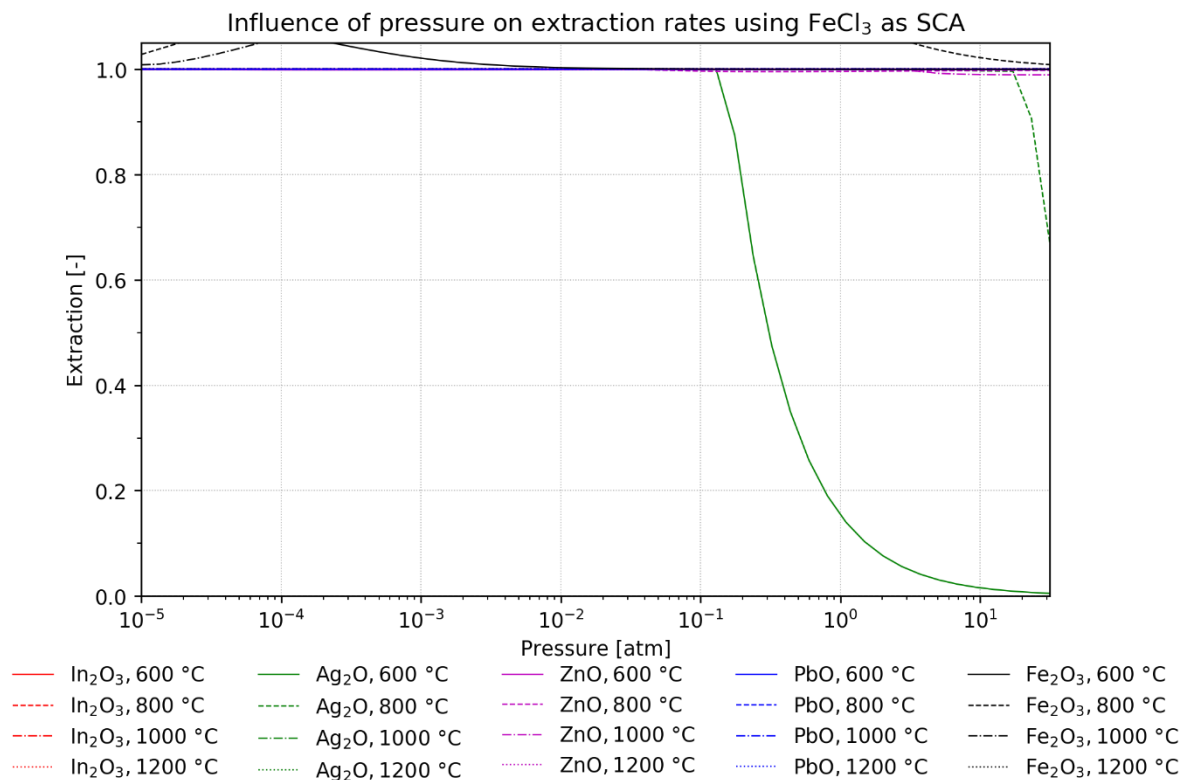
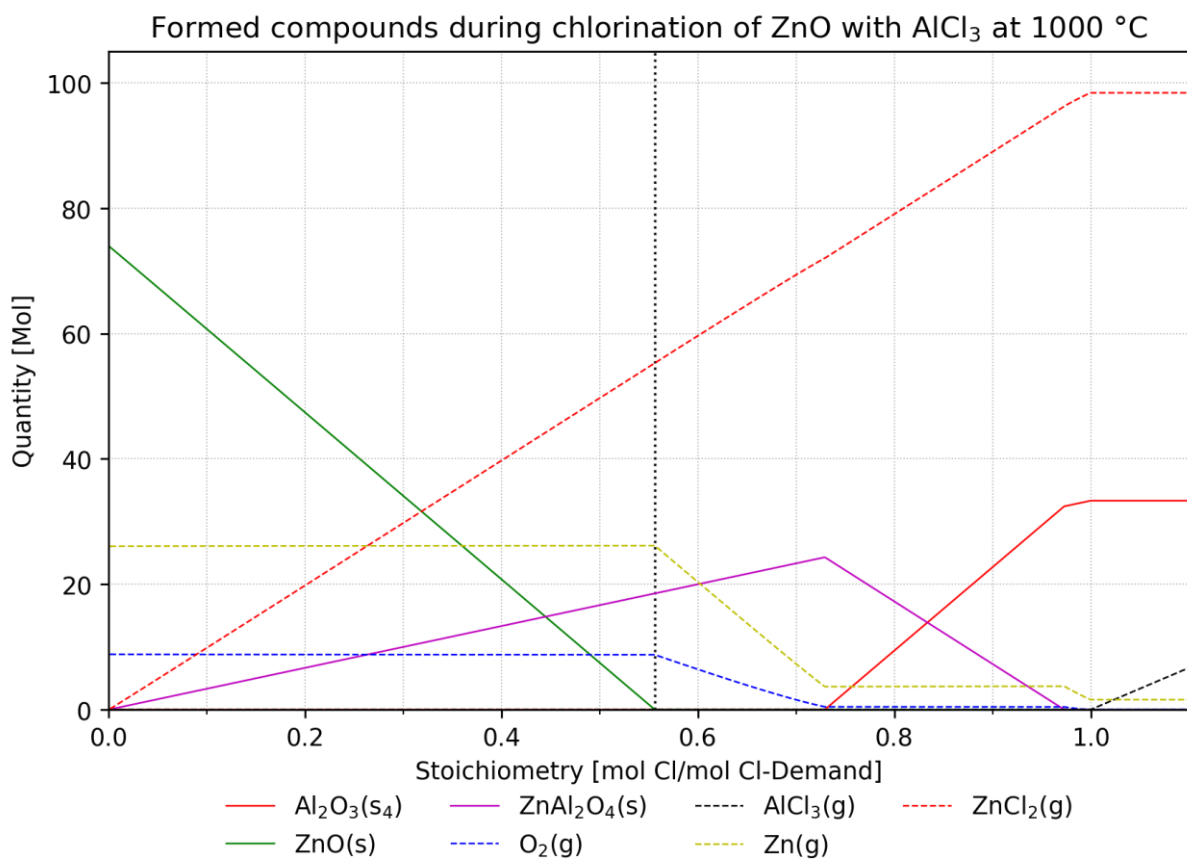


Figure 49: Influence of pressure on extraction rates of assessed metals using MgCl_2 as SCA

Figure 50: Influence of pressure on extraction rates of assessed metals using FeCl_3 as SCAFigure 51: Formation of various solid (solid lines) and gaseous (dashed lines) compounds in the ZnO - AlCl_3 -system in dependence of chlorine stoichiometry (1000 °C)

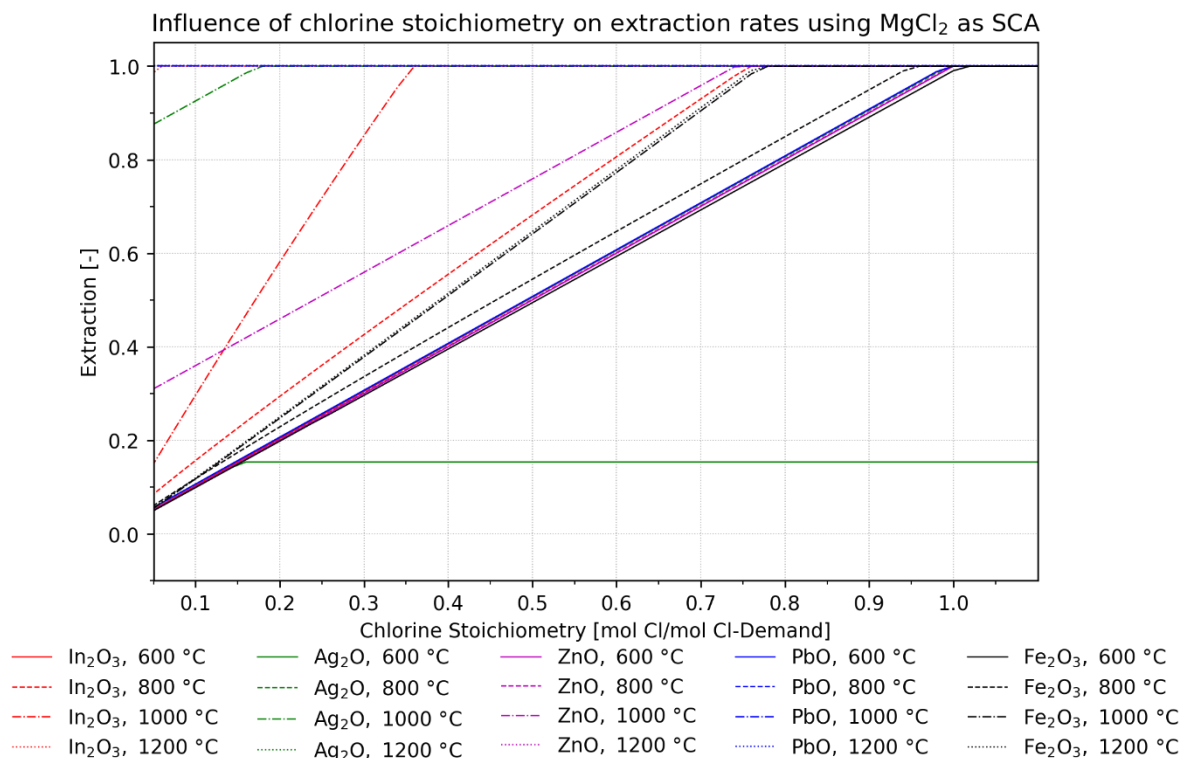


Figure 52: Influence of stoichiometry on extraction rates using MgCl₂ as SCA at various temperatures, pressure of 1 atm and inert atmosphere

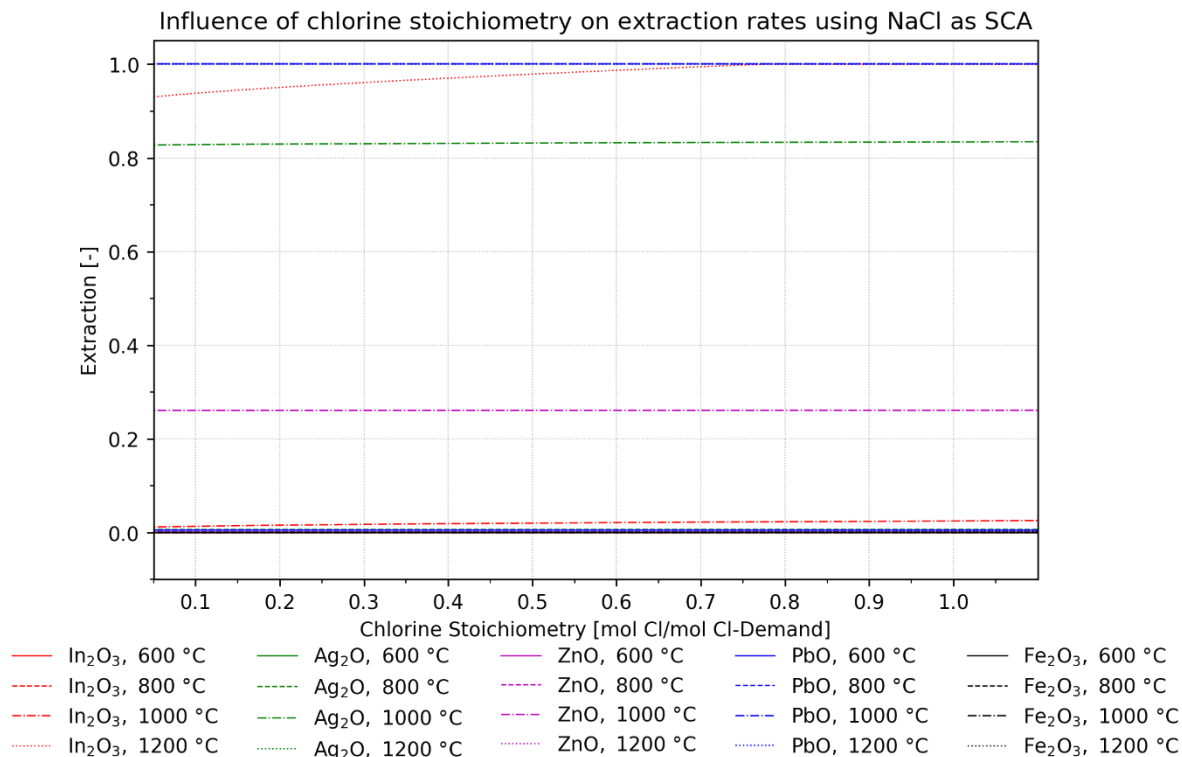


Figure 53: Influence of stoichiometry on extraction rates using NaCl as SCA at various temperatures, pressure of 1 atm and inert atmosphere

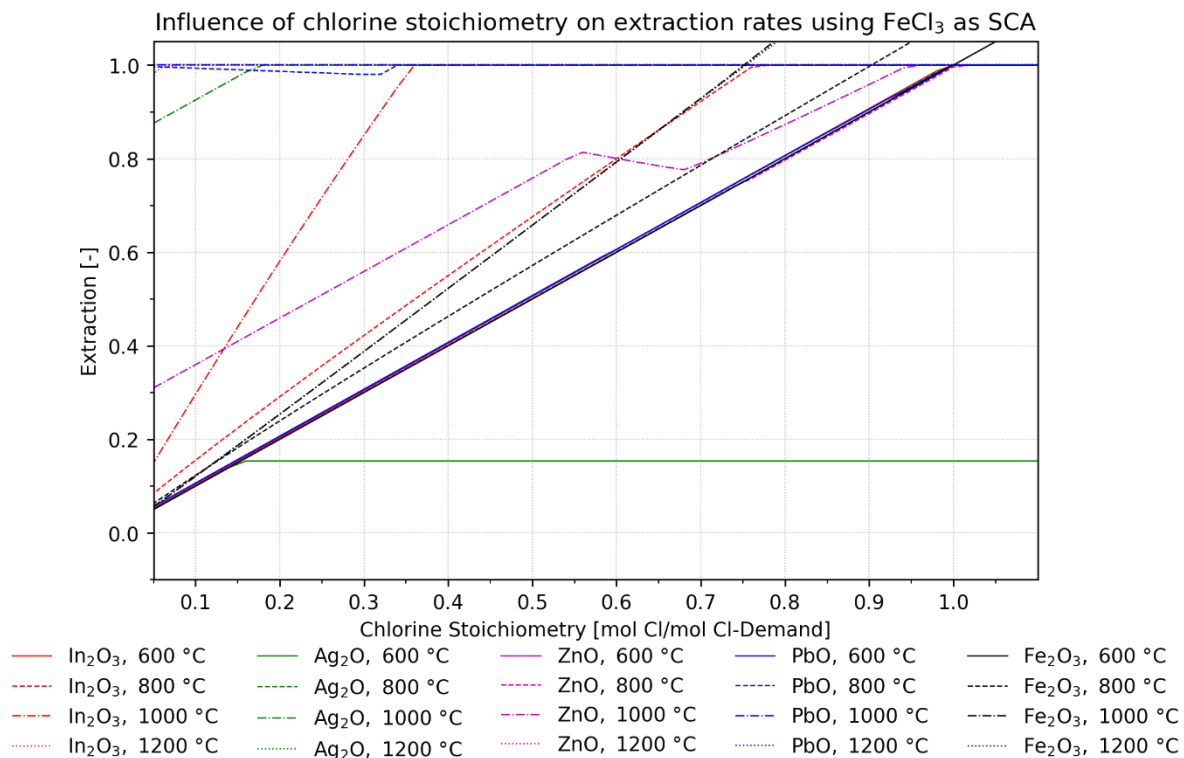


Figure 54: Influence of stoichiometry on extraction rates using FeCl₃ as SCA at various temperatures, pressure of 1 atm and inert atmosphere

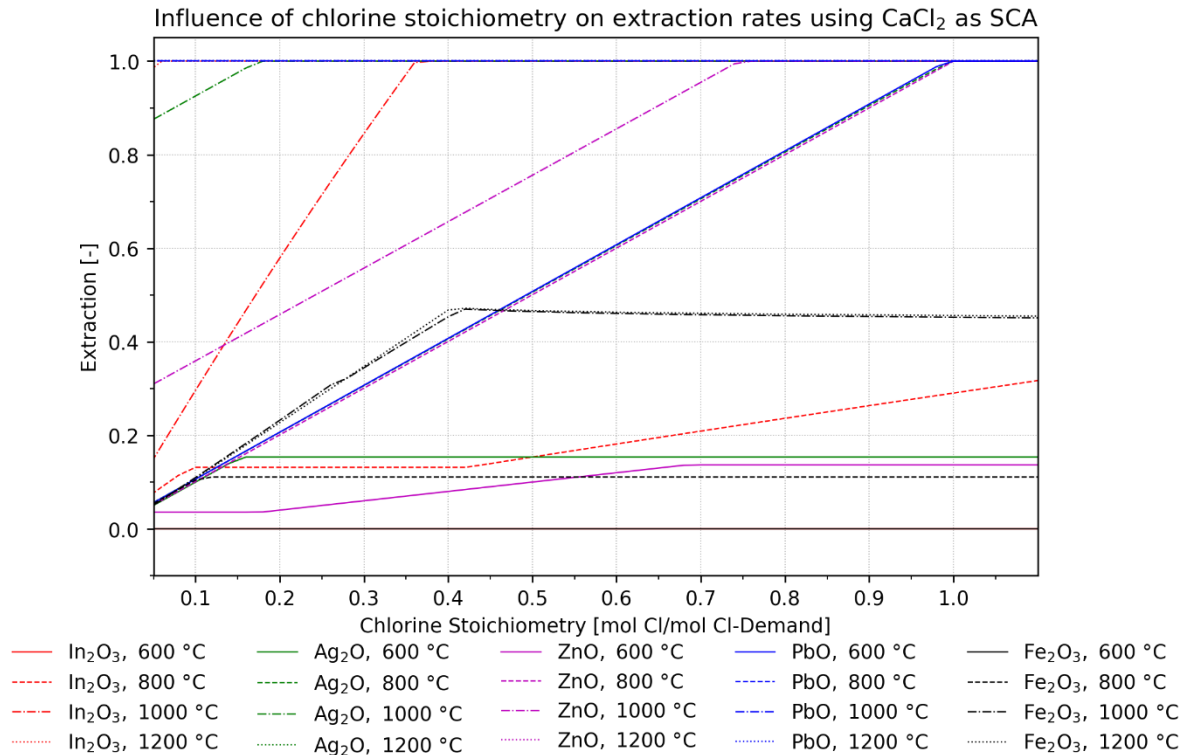
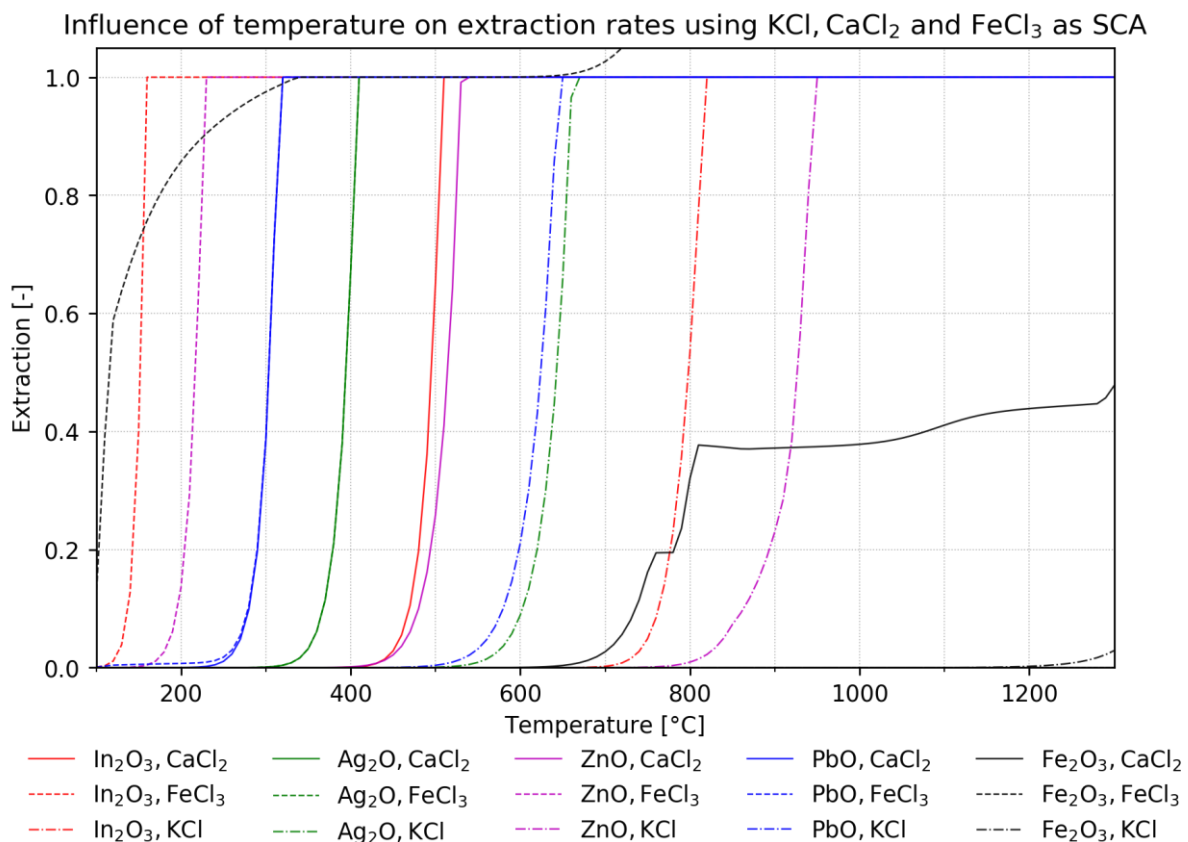


Figure 55: Influence of stoichiometry on extraction rates using CaCl₂ as SCA at various temperatures, pressure of 1 atm and inert atmosphere

Table 6: Overview of assessed qualitative influences

		Metal	Ag	Fe	In	Pb	Zn
		Mean Extraction [%]	63.8	39.0	78.7	99.0	73.1
Deviation from Mean Extraction [rel.-%]	Atmosphere	Ar	-4.0	7.3	2.8	0.0	3.5
		CO	-12.7	15.2	11.8	1.0	24.4
		H ₂ O	-6.6	-42.7	-4.4	-0.1	-7.9
		O ₂	17.6	-5.5	-15.5	-0.9	-20.2
		SO ₂	5.6	25.8	5.2	0.1	0.1
	Form	Hydride	-17.8	-11.2	17.9	0.8	17.9
		Metallic	-8.8	-43.8	2.9	0.3	4.7
		Oxide	11.7	99.0	9.3	0.5	5.9
		Sulfate	14.9	-44.0	-30.0	-1.6	-28.5
	SCA	AlCl ₃	2.3	4.5	1.6	-0.6	-3.5
		CaCl ₂	-2.7	-22.9	-4.0	0.3	2.8
		FeCl ₃	0.1	23.9	1.2	-0.3	0.4
		MgCl ₂	0.2	-5.5	1.2	0.6	0.3
	Secondary Compound	CaF ₂	21.3	1.8	5.0	0.9	17.4
		FeS ₂	-17.8	63.0	27.0	1.0	16.9
		K ₂ SO ₄	-29.5	-83.7	-40.8	-0.4	-46.8
		SiO ₂	26.0	18.9	8.8	-1.6	12.5

Figure 56: Influence of temperature on extraction rates of indium, silver, zinc, lead and iron from mock jarosite mixture using KCl, CaCl₂ or FeCl₃ as SCA

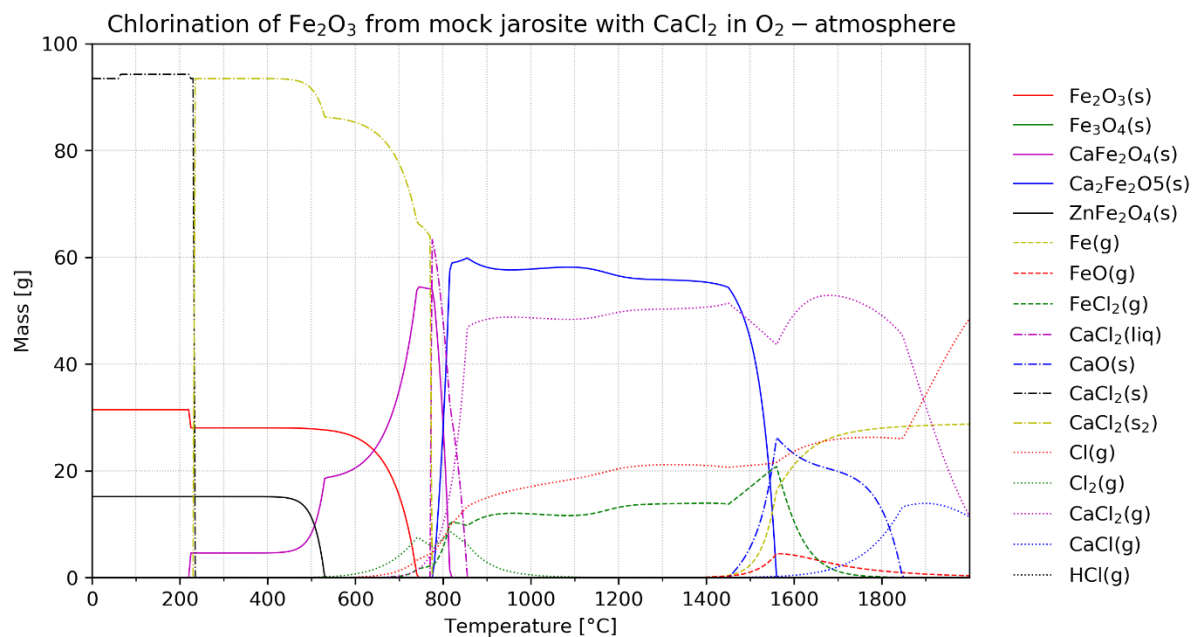


Figure 57: Formation of various solid (solid lines) and gaseous (dashed lines) iron compounds as well as solid (dash dotted) and gaseous (dotted) compounds of CaCl_2 during chlorination of mock jarosite as a function of temperature in O_2 -atmosphere

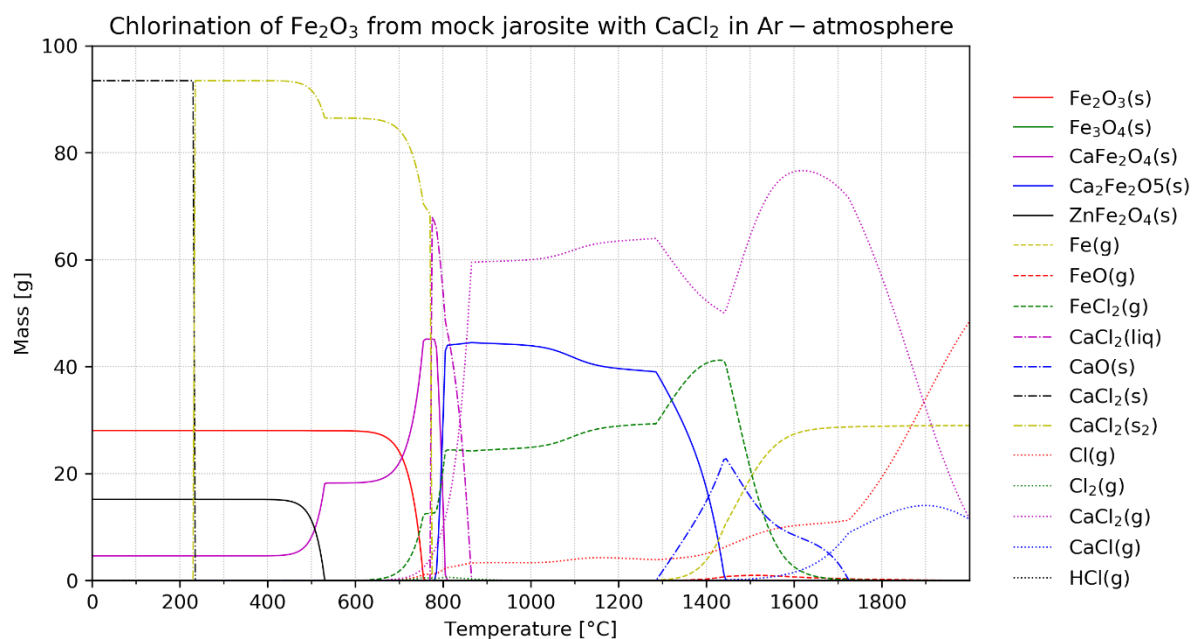


Figure 58 Formation of various solid (solid lines) and gaseous (dashed lines) iron compounds as well as solid (dash dotted) and gaseous (dotted) compounds of CaCl_2 during chlorination of mock jarosite as a function of temperature in Ar-atmosphere

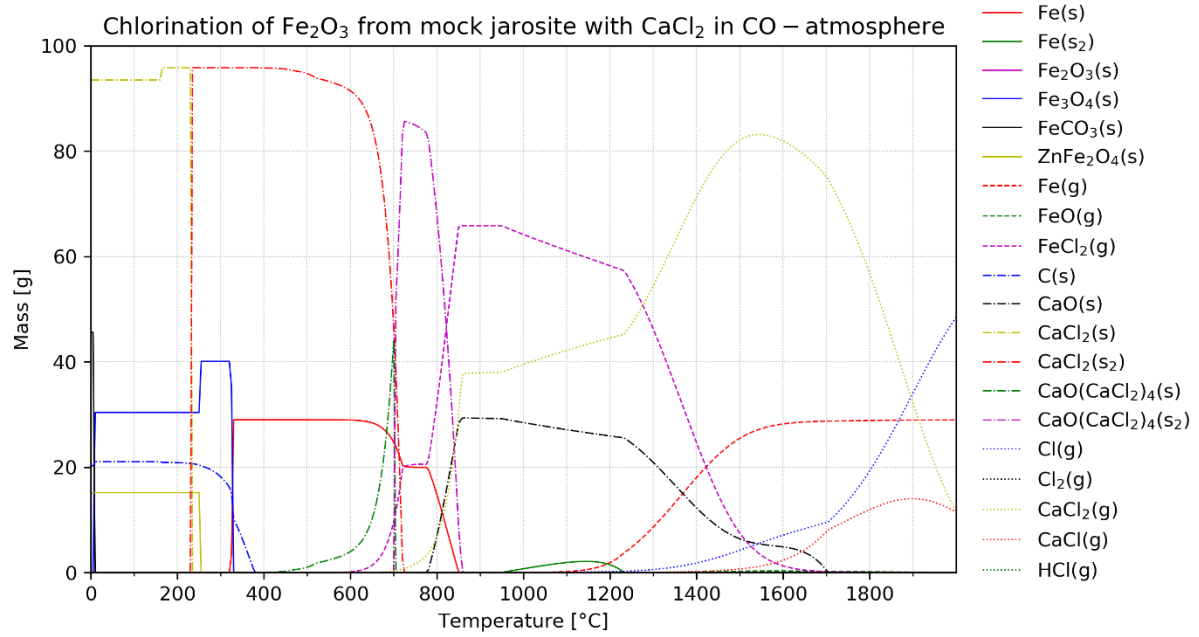


Figure 59: Formation of various solid (solid lines) and gaseous (dashed lines) iron compounds as well as solid (dash dotted) and gaseous (dotted) compounds of CaCl₂ during chlorination of mock jarosite as a function of temperature in CO-atmosphere

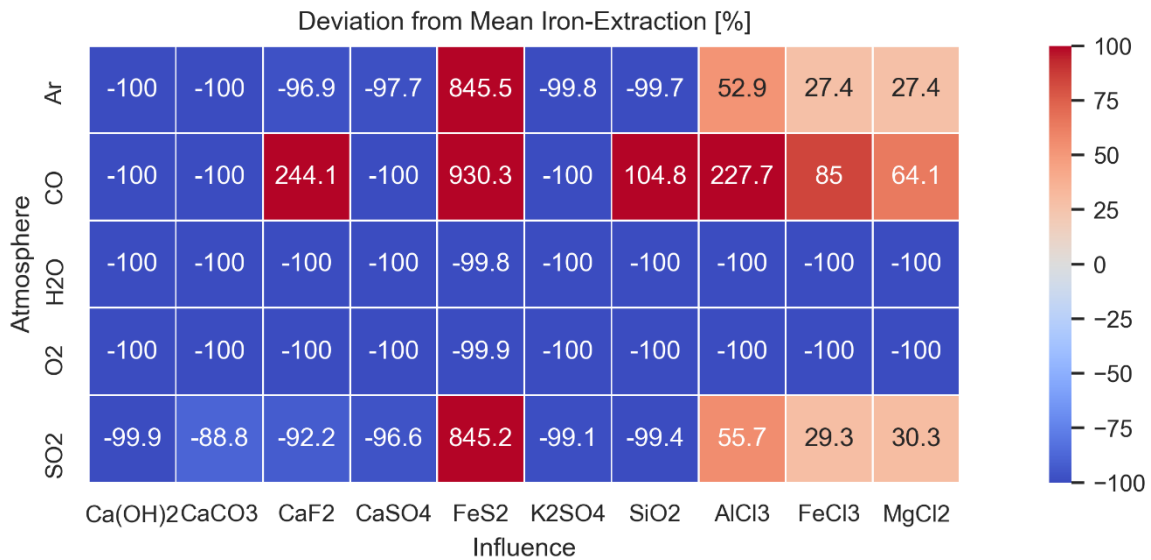


Figure 60: Deviation from mean iron extraction for various atmospheres in combination with different secondary compounds and SCAs for full temperature range, 1 atm and stoichiometry of 1

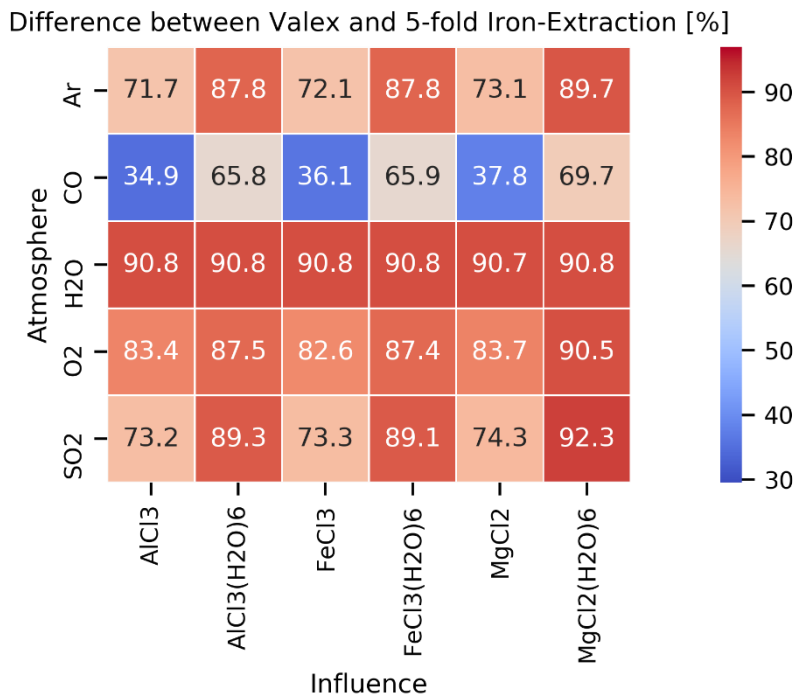


Figure 61: Difference between Valex and 5-fold iron extraction for various atmospheres with anhydrous and hydrated SCAs, mean values for temperatures, pressure of 1 atm and stoichiometry of 1

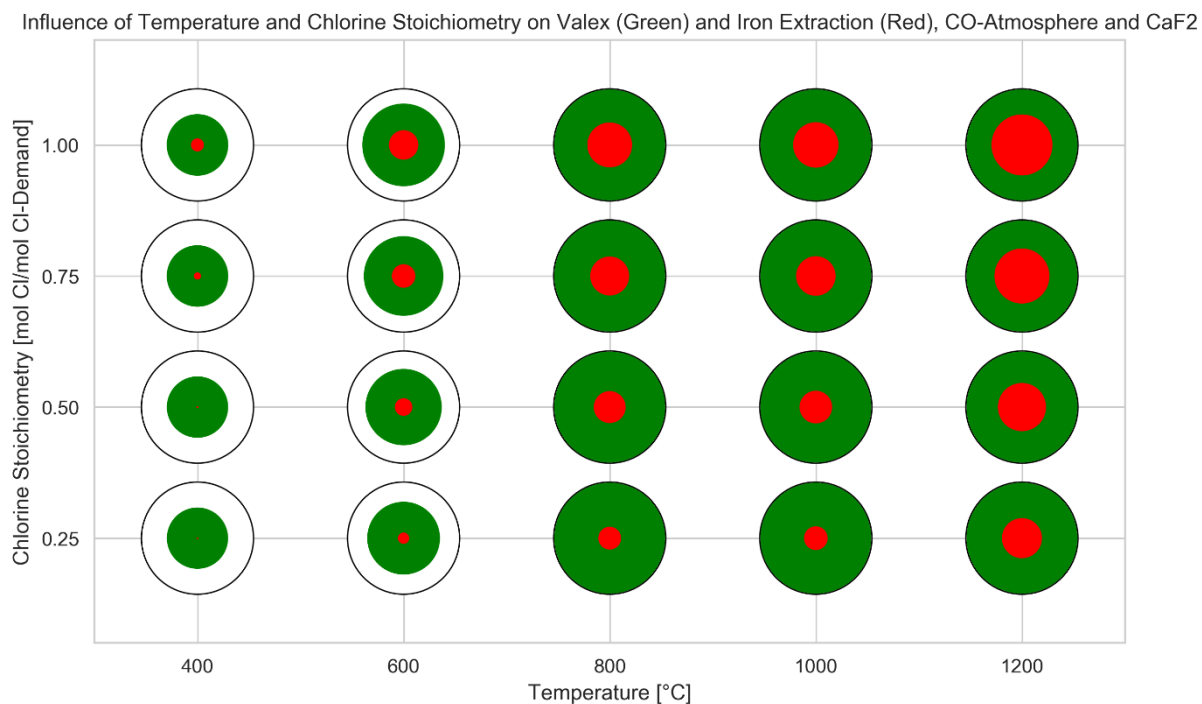


Figure 62: Influence of temperature and chlorine stoichiometry on Valex (green) and iron extraction (red) in CO-atmosphere and the presence of CaF₂, the black circle represents a value of 1.00

Influence of Temperature and Chlorine Stoichiometry on Valex (Green) and Iron Extraction (Red), O₂-Atmosphere and CaSO₄

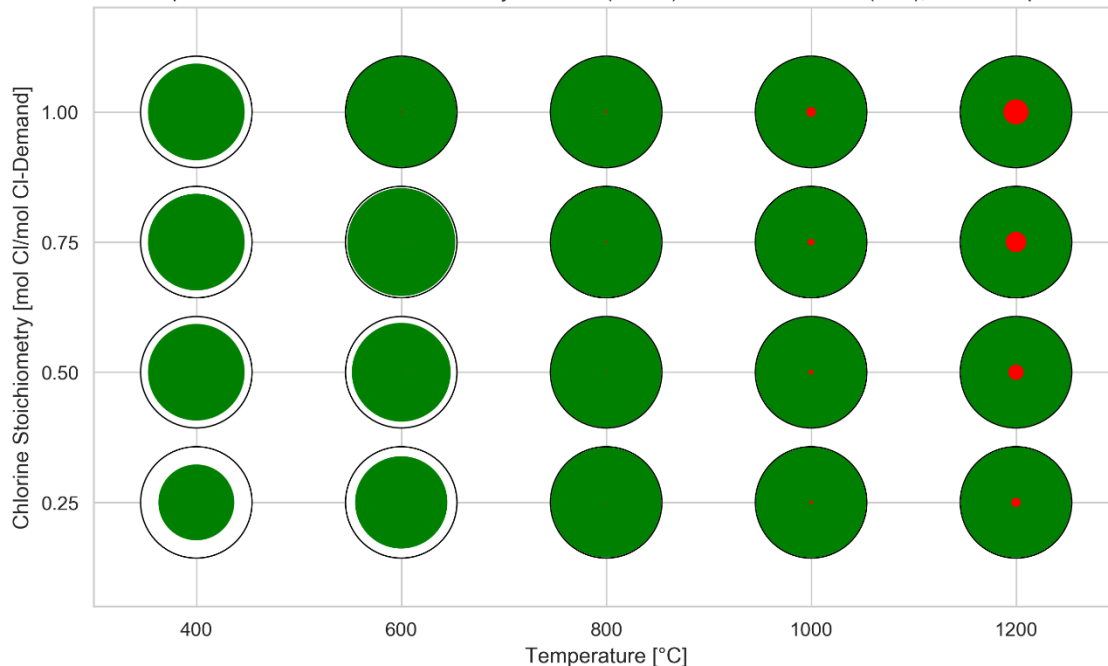


Figure 63: Influence of temperature and chlorine stoichiometry on Valex (green) and iron extraction (red) in O₂-atmosphere and the presence of CaSO₄, the black circle represents a value of 1.00

Chapter 4

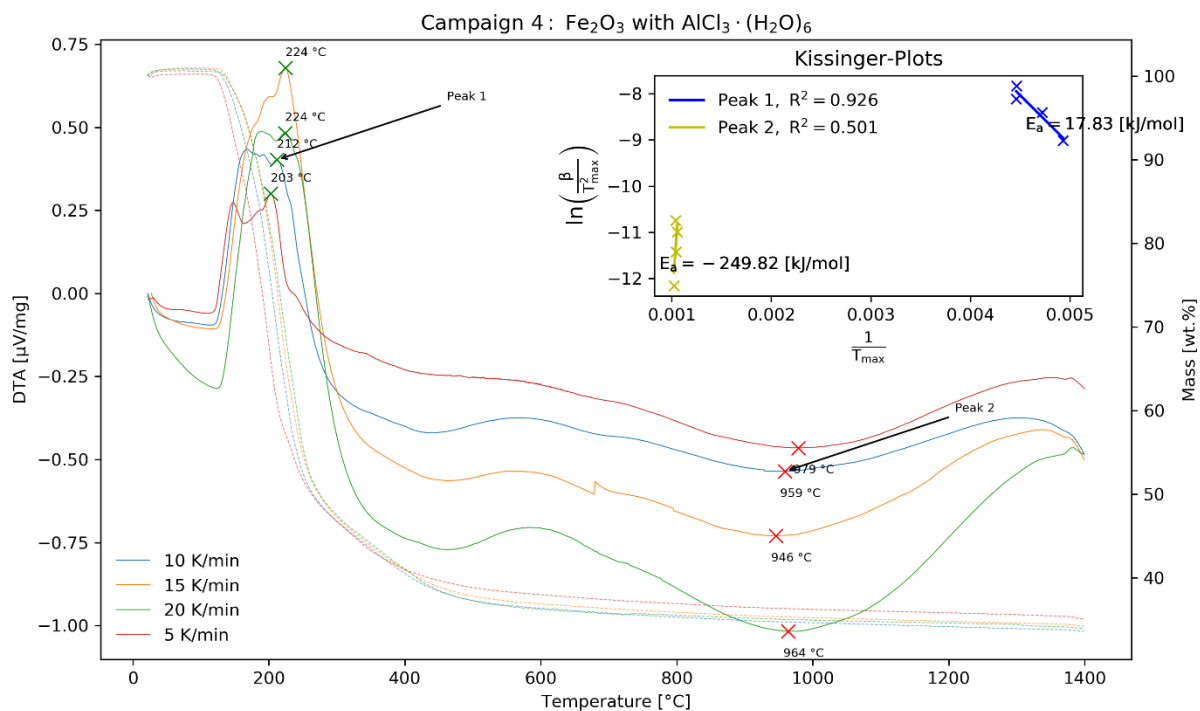


Figure 64: DTA- (solid lines) and mass- (dashed lines) curves for the chlorination of Fe₂O₃ with AlCl₃·6H₂O at 5, 10, 15 and 20 K/min, assessed endothermic (green crosses) and exothermic (red crosses) peaks and their Kissinger-plots with calculated activation energy